POLITECNICO DI MILANO

School of Industrial and Information Engineering
Department of Chemistry, Materials and Chemical Engineering:
"Giulio Natta"
Master of Science in Materials Engineering and Nanotechnology

MATERIALS FROM LIGNIN FOR INDUSTRIAL APPLICATIONS

Supervisor: Prof. Stefano Turri
Co-supervisor: Dr. Gianmarco Griffini

Master's Thesis of: Monica Bonfiglio
Identification number: 823578

Academic year: 2015-2016

Table of contents

List of figures

List of Tables

ABSTRACT

Nowadays a great amount of the energy resources and also of material products derives from the oil and petroleum industry; the limited availability of these resources, anyway, together with the concerns related to the impact that their utilization had (and continues to have) on the environment have led the world to focus attention on the research of new solutions able to replace them. The direct competitor of oil as raw material for fuel and production of chemicals appears to be the biomass. In the context of lignocellulosic biomass is inserted the focus of this thesis work, the lignin. Due to its many functional groups, it can be enhanced from simple waste to finished product to be applied in several sectors.

Purpose of this work was then to realize different functionalizations of this polymer. In the first part, the soluble fraction (SLF) of Indulin lignin was reacted with succinic anhydride (SA) to obtain a polyester (SAL) able to self-crosslink (SAL Self); then this system was compared with the polyester combined with a crosslinker (SAL-CYM) and with the soluble fraction combined with a crosslinker (SLF-CYM). After that, several analysis were performed: DSC and TGA to evaluate the thermal properties, OCA and pull-off test to highlight the surface characteristics and AFM and microindentation test to investigate the mechanical properties. Systems showed to possess good adhesion properties to different types of substrates, together with a high stiffness due to the high Tg. In the second part, the anti-corrosion and antioxidant properties of lignin were examined: soluble fraction (SLF) of Indulin was reacted with 3-Isocyanatopropyltrimethoxysilane (IPTMS) to obtain a silanized lignin (LKSi). This system was compared to another one containing also a crosslinker (LKSi-TEOS), and the modification of their properties was evaluated when a plasticizer was added in the formulations. Once again, several analysis were performed: DSC and TGA to evaluate the thermal properties; pull-off measurements to highlight the surface characteristics; potentiodynamic measurements to investigate anti-corrosion properties. The systems showed to possess good adhesion properties to different metallic substrates, and also a corrosion limit current density strongly reduced. Also a bending test was executed to confirm the improvement in plastic behavior of the formulations containing a plasticizer with respect to the others. In the last part, a brief introduction to the utilization of lignin into composite materials was carried out: an aqueous solution of Indulin and a crosslinker (IND-PR) was investigated and compared to a wide used mixture of acrilic resins, also in aqueous solution (SAD-ACR); both of them were utilized as matrix for the impregnation of carbon fibers. Two analysis were performed: the DMA showed that the modulus of both these systems increased with the progressively addition of matrix content in the composite; the SEM instead highlighted a better distribution of the Indulin inside the fibers network with respect to the industrial system, although both of them weren't able to wet the fibers homogeneously.

SOMMARIO

Ogni aspetto della nostra vita quotidiana è influenzato dai progressi che l'industria chimica ha compiuto negli ultimi due secoli: dai beni di prima necessità alle risorse di vario genere, essa è stata capace di migliorare nel tempo il nostro tenore e le nostre aspettative di vita. L'industria chimica è alla base del settore industriale ma è tuttora legata a risorse che con il passare dei decenni stanno diventando critiche e poco sostenibili e che sono la causa di numerose problematiche, come l'inquinamento provocato dai processi chimici e il rilascio di prodotti pericolosi nell'ambiente . Questa presa di coscienza ha portato ad una forte sensibilizzazione dell'opinione pubblica nei riguardi di questi temi, arrivando alla nascita del concetto di Sviluppo Sostenibile, ovvero di "una forma di sviluppo che sia compatibile con la salvaguardia dell'ambiente e dei beni liberi per le generazioni future"(The World Commission on Environment and Development, 1987). E' stata dunque individuata una valida alternativa al petrolio come materia prima da cui ottenere energia e prodotti chimici: la biomassa. Tra le varie tipologie, la biomassa lignocellulosica è di particolare interesse per lo sviluppo di questo elaborato, dal momento che da essa si ottiene la lignina, argomento centrale di questo studio. La lignina è un polimero di natura aromatica presente in grandi quantità in natura; la si ottiene dallo scarto della lavorazione della carta ed è attualmente impiegata per la maggior parte come combustibile a causa del suo alto potere calorifico. Grazie però alla grande varietà di gruppi funzionali, è possibile valorizzarla trasformandola in prodotto finito. La funzionalizzazione di questo polimero è dunque lo scopo di questo elaborato che ha come obiettivo quello di ottenere diversi prodotti da applicare in svariati settori industriali.

Nei tre capitoli che compongono il trattato è presente una suddivisione effettuata sulla base delle tre funzionalizzazioni attuate su una lignina kraft denominata Indulin AT.

- Nella prima parte , è stata realizzata una esterificazione della frazione solubile della lignina Indulin (SLF) mediante reazione chimica con Anidride Succinica (AS) per ottenere un poliestere in grado di reticolare autonomamente (SAL Self); questo sistema è stato confrontato con altri due: uno contenente la frazione solubile unita ad un agente reticolante (SLF-CYM) e uno contenente il suddetto poliestere unito ad un agente reticolante (SAL-CYM), entrambi in diversi rapporti di concentrazione. Le soluzioni sono state deposte su differenti substrati, trattate termicamente in stufa e analizzate attraverso diverse prove di caratterizzazione, fra cui: prove calorimetriche e termogravimetriche (DSC e TGA) per individuare Tg e perdite percentuali di massa; misure di angolo di contatto per verificare la bagnabilità delle superfici; misure di adesione dei rivestimenti su diversi substrati; prove di microindentazione per verificare la durezza dei film; analisi AFM per individuare la morfologia dei rivestimenti. I risultati ottenuti hanno mostrato che tutti e tre i sistemi possiedono Tg piuttosto elevate; ciò

ha consentito loro di apparire particolarmente resistenti. Le superfici dei film mostrano un carattere progressivamente più idrofilo passando dalle soluzioni contenenti AS a quelle prive di AS. Le adesioni ai vari substrati risultano buone nel caso dell'alluminio, e piuttosto elevate nel caso del vetro e del legno.

- Nella seconda parte sono state indagate le proprietà anti corrosive della lignina: la frazione solubile della Indulin (SLF) è stata fatta reagire con IPTMS per ottenere una lignina silanizzata (LKSi); oltre a tale sistema ne è stato realizzato un altro contenente un agente reticolante (LKSi-TEOS), ed entrambe le formulazioni sono poi state confrontate con due sistemi ad esse identici ma aventi all'interno un certo quantitativo di plasticizzante [(LKSi-TEOS)+GLY e (LKSi)+GLY]. Le quattro soluzioni, ciascuna delle quali realizzata in due differenti concentrazioni di lignina nel solvente (0,5% e 20%), sono state deposte su differenti substrati metallici, trattate termicamente in stufa e analizzate attraverso diverse prove di caratterizzazione, fra cui: prove calorimetriche e termogravimetriche (DSC e TGA) per individuare Tg e perdite percentuali di massa; misure di adesione dei rivestimenti su diversi substrati; prove potenziodinamiche per verificare la densità di corrente limite di corrosione; prove di bending per attestare la capacità di deformazione dei film. I risultati ottenuti hanno mostrato che i due sistemi senza plasticizzante possiedono Tg piuttosto elevate; l'aggiunta del plasticizzante decresce la Tg progressivamente con l'aumento della concentrazione in soluzione: ciò ha consentito ai film di resistere alle piegature effettuate sui substrati senza arrivare a danneggiarsi. I rivestimenti ad alta concentrazione di lignina hanno mostrato una buona adesione sia all'alluminio che all'acciaio; più elevata si è dimostrata invece quella dei film a bassa concentrazione di lignina. La resistenza alla corrosione dei quattro sistemi è risultata essere elevata su entrambi i substrati metallici.

- Nella terza parte sono stati effettuati degli studi preliminari sull'impiego della lignina come matrice per materiali compositi: una soluzione acquosa di Indulin e di un agente reticolante (IND-PR) è stata messa a confronto con una soluzione acquosa contenente resine acriliche di largo utilizzo nel settore industriale (SAD-ACR), entrambe a diverse concentrazioni di matrice; esse sono state utilizzate per impregnare dei tessuti non tessuti di fibre di carbonio. I due sistemi, dopo trattamento termico, sono stati sottoposti ad analisi DMA, dalla quale si è evinto che l'aumento del valore del modulo (GPa) è proporzionale all'aumento delle concentrazioni di matrice nel composito, arrivando quasi al valore delle sole fibre di carbonio. Le analisi al SEM hanno invece fornito una visione microscopica dei sistemi, da cui si è evinto che sebbene entrambe le matrici non impregnino uniformemente le fibre, tuttavia il sistema a base di lignina riesce a rimanere tra le fibre in quantità maggiori.

FOREWORD

The chemical industry is responsible for the creation of an immense variety of products which influences every aspect of our lives. While some of these products from the industry such as soaps, cleansing, generic detersives or perfumes are bought directly by the consumers, a great amount of chemicals are used instead by other industries as intermediates to produce more complex goods. The industry transforms a wide range of raw materials, from basic chemicals to consumer ones. Among basic materials, the most important are the chemicals derived from oil, also called petrochemicals. The effects of the utilization of fossil fuels are, by the way, for the most part responsible for: the decrease in fossil fuel reserves due the increase in energy demand; the change of the global climate due to the increase of CO_2 emission in the atmosphere; the increase of wastes due to the growth of the world population.

It is worth noting that many of these wastes, coming for example from agricultural, industrial and even residential sectors, could be considered as potential renewable energy sources to achieve sustainability. Sustainability can be defined as the preservation of processes of productivity for an unlimited period of time; it can be done through the substitution of the depleted resources with equal or greater value ones, without the need to degrade or put in danger the natural biotic systems.

Among all the possible renewable resources, biomass appears to be a direct competitor of the raw materials coming from non renewable resources like oils. In the context of lignocellulosic biomass is inserted the focus of this thesis work, the lignin. It is obtained as a waste of the paper production process, and usually the black liquor in which it is contained is used as a source of energy, due to the higher calorific value of lignin with respect to those of cellulose and hemicellulose. Anyway, the change of the modern industry imposed by the nowadays needs has required a deep modification of the utilization of this polymer: thanks to the huge variety of functional groups present in its structure, lignin can be transformed from a mere fuel source into a macromolecular building block for polymers, and functionalized to obtain added value products for different applications.

For this reason, the focus of this work has been centered on the realization of different lignin-based materials for several applications, in an effort to contribute to the valorization of the industrial wastes and also to offer innovative solutions to overcome the environmental issues that, year after year, have become always more worrisome.

1 INTRODUCTION

1.1 Sustainable development

In 1987 a report called *Our Common Future* was emitted by the United Nations World Commission on Environment and Development; this report, commonly called the Brundtland Report, included what is now one of the most widely recognized definitions of sustainable development. (1)

“Sustainable development is development that meets the needs of the present without compromising the ability of future generations to meet their own needs. It contains within it two key concepts:
· The concept of 'needs', in particular, the essential needs of the world's poor, to which overriding priority should be given; and
· The idea of limitations imposed by the state of technology and social organization on the environment's ability to meet present and future needs. **”**

— World Commission on Environment and Development, Our Common Future (1987)

Sustainable development can be defined as the organizing principle for the maintenance of finite resources necessary to provide for the needs of future generations of life on Earth. It is a process that images a desirable future state for human societies in which the living conditions and the consuming of the main resource make an effort to meet human needs without causing the violation of the "integrity, stability and beauty" of natural living systems. (2)

Sustainability can be also defined as the ability to maintain all the processes involving the production, whether they are natural or human made, by substituting the resources used with resources of equal or greater value without degrading or endangering natural biotic systems. Sustainable development binds together the concern for the natural systems with the social, political, and economic challenges faced by humanity. (3)

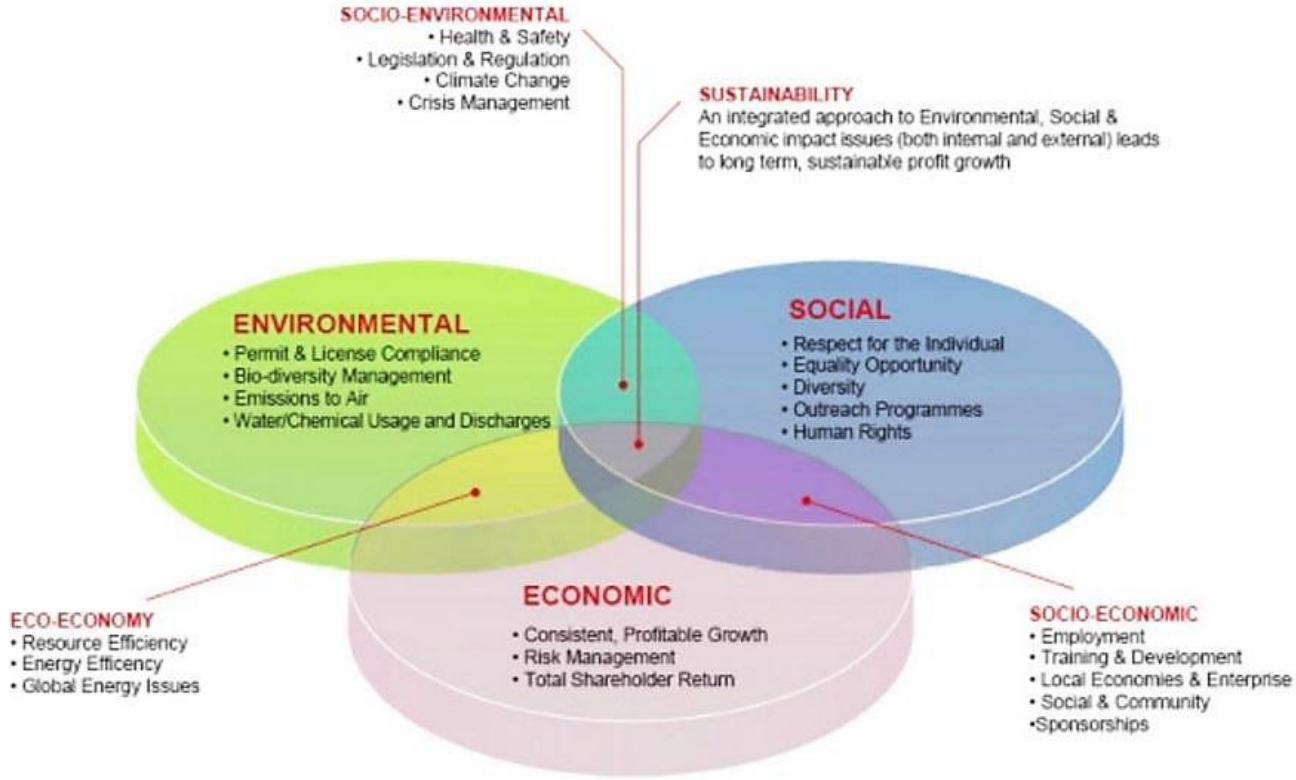

Figure 1 Graphical representation of the Sustainable Development components (4)

It has been described, as it is possible to see in **Figure 1**, in terms of three domains or pillars, i.e. the environment, the economy and society. This framework was initially introduced by the economist René Passet in 1979, and shows the three major parts in which it can be divided.

- **Environmental sustainability**:

As visible in **Table 1,** it cares about the natural environment and how it can withstand and maintain its variety of production. Since the natural resources are derived from the environment, protecting the climate and the state of air and water has become quite fundamental in the last years. Environmental sustainability has demanded and continues to demand to the society to design activities able to meet human needs while preserving the life support systems on Earth. This, for example could be translated in using water sustainably, utilizing renewable energy, and sustainable material supplies (e.g. harvesting wood from forests at a rate that allows the biomass and biodiversity to maintain themselves). (5)

Consumption of non-renewable resources	State of environment	Sustainability
More than nature's ability to replenish	Environmental degradation	Not sustainable
Equal to nature's ability to replenish	Environmental equilibrium	Steady state economy
Less than nature's ability to replenish	Environmental renewal	Environmentally sustainable

Table 1 Sustainability as a function of the consumption rate of nature's resources (6)

- **Politics:**

Sustainable political development was defined by the United Nations Global Compact Cities Programme in a much broader way than the usual definition, standing beyond states and governance. Since policy has been defined as "the domain of practices and meanings associated with basic issues of social power as they pertain to the organization, authorization, legitimation and regulation of a social life held in common", it was possible to find a connection with the view that political change is important for responding properly to ecological, economic and cultural challenges. It also means that the politics of economic change can be addressed. Seven subdomains of the domain of politics have been listed, according to the previous definition:

1. Organization and governance
2. Law and justice
3. Communication and critique
4. Representation and negotiation
5. Security and accord
6. Dialogue and reconciliation
7. Ethics and accountability

This accords with the Brundtland Commission emphasis on development that is guided by human rights principles. (7)

- **Economics aspect:**

The sustainable economic growth, fundamental for the progress of each State, requires anyway safe and sustainable resources for industrial production. To be able to rearrange a substantial economy to biological raw materials, new approaches are necessary in field of research and development, in production and economy. This, first of all, requires to search for new solutions in order to decrease the rapid consumption of fossil and non-renewable resources (petroleum, natural gas, minerals). While, indeed, the economy of energy can be based on several valid alternative raw materials (wind, biomass, sun, nuclear fission, water, and nuclear fusion), the material economy of resources instead is still mainly depending on biomass, in particular on plant biomass. The key to the success depends on how far it will be possible to modify today's production gradually from fossil to biological raw materials. New approaches in research and development are required to rearrange the whole economies to biological raw materials as a source for increased value. It is important that biological and chemical sciences play a leading role in the generation of future industries in the twenty-first century, but also that new synergies are worked out and established between different fields concerning the sciences. This, in the end, needs to be combined with new technologies concerning media and information, but also with economic and social sciences. Special requirements will be placed on both the converting industry and on research and development with regard to raw material and production line efficiency and sustainability. (8)

The development of systems able to convert substances into basic products and also polyproducts, such as biorefineries, will be "the key for the access to an integrated production of food, feed, chemicals, materials, goods, and fuels of the future" (National Research Council 2000).

1.2 Biorefinery

Biorefining is defined as the sustainable processing of the biomass into a wide range of marketable products and energy. (9) The biorefinery concept embraces a wide range of technologies able to separate biomass resources like for example wood into their building blocks, and to value added products, like biofuels and also chemicals. (10)

A biorefinery is a facility or a network of more facilities that involves processes of biomass conversion and the equipment to produce transportation of biofuels, power, and chemicals from biomass (**Figure** 2). This concept is analogous to the refinery of petroleum, which produces multiple

fuels and products from the petroleum. The main biobased products are today obtained from the conversion of biomass into oil, starch and cellulose. In addition, some chemicals like amino acids are produced and used in the food industry. Other already commercially available biobased products comprise adhesives, compounds for cleaning, dyes, detergents, hydraulic fluids, inks, lubricants, packaging materials, paints and coatings, paper, plastic fillers, polymers, solvents, and sorbents. Most of the existing biofuels and biochemicals are currently realized with materials that are in competition with the food and the feed industry, usually obtained under the form of single production chains and not within a biorefinery concept. Their exploitation is thereby limited. On the other hand, lignocellulosic crops reduce the competition for fertile land, since it is possible to make them grow on lands which are not suitable for agricultural crops. Moreover, among all the conventional crops that can contribute only with a small fraction of the above standing biomass, biorefineries based on lignocellulosic feedstocks can rely on larger biomass per hectare yields. (10)

The aim of technological process in biorefinery is to depolymerize and to deoxygenate the biomass components. In order to convert biomass feedstock into valuable products within a biorefinery approach, several technological processes must be utilized. They can be thereby divided in four main groups: thermochemical, biochemical, mechanical/physical and chemical processes.

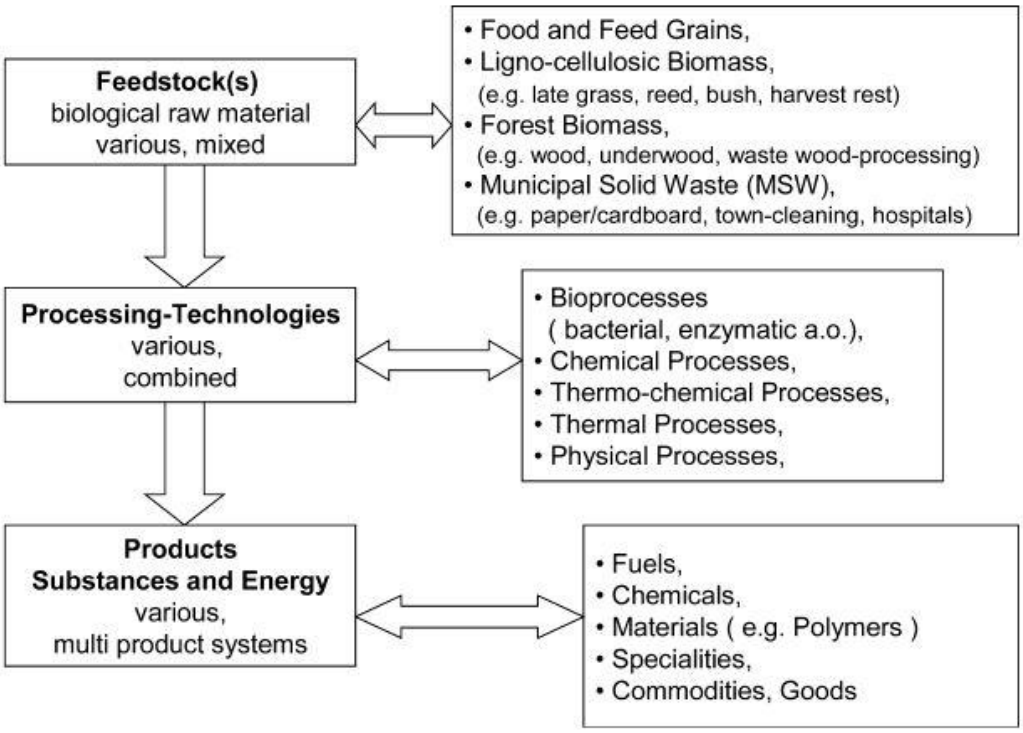

Figure 2 Basic principles of a biorefinery (8)

- **Thermochemical processes:**

There are two main thermochemical processes that can be used to convert biomass into energy and chemical products. The first of them is the gasification, which consists in the maintenance of the biomass at high temperature (>700 °C) with low oxygen levels for the production of the syngas, which consists of a mixture of H_2, CO, CO_2 and CH_4. Syngas can be used directly as a stationary biofuel or can be transformed into a chemical intermediate for the fuels production or for the chemicals production (alcohols, organic acids, ammonia, methanol and so on). The second thermochemical process of conversion of biomass is called pyrolysis, which takes advantage of intermediate temperatures (300–600 °C) in the absence of oxygen to convert the feedstock into liquid or bio-oil, solid charcoal and light gases similar to the previously cited syngas. Their yields vary with process conditions and for biorefinery purposes the treatment which maximizes the production of liquid bio-oil is the most desirable (flash pyrolysis). This is the most common and oldest form of biomass conversion that involves burning biomass in an oxygen-rich environment mainly for the production of heat. (10)

- **Biochemical processes:**

Unlike thermochemical processes, biochemical processes take place at lower temperatures and possess also lower reaction rates. The most common types of biochemical processes are, for example, fermentation and the anaerobic digestion. The fermentation, in particular, uses microorganisms or enzymes to convert a fermentable substrate into recoverable products (usually alcohols or organic acids). The most required fermentation product usually is ethanol, but the production of many other chemical compounds such as hydrogen, succinic acid, methanol, is nowadays object of many research and development activities. The most frequent fermentation substrates are Hexoses like glucose, while hydrocarbons like pentoses, which are the sugars from hemicellulose, and glycerol usually require the development of customized fermentation organisms able to transform them into ethanol. Anaerobic digestion involves instead the bacterial breakdown of biodegradable organic material in the absence of oxygen over a temperature range going from about 30 to 65 °C. The main end product of these processes consists of biogas, which unlike syngas, consists of a gas mixture made of methane, CO_2 and other impurities, and can be upgraded up to >97% methane content and used as a surrogate of natural gas. (10)

- **Chemical processes:**

Chemical processes allow a change in the chemical structure of the molecule by promoting its reaction with other substances. The most common chemical processes in biomass conversion are hydrolysis and transesterification. While hydrolysis uses acids, alkalis or enzymes to depolymerize polysaccharides and proteins into their basic components like, for example sugar from cellulose, or

derivate chemicals like for instance levulinic acid from glucose, the transesterification instead is the process of exchanging the organic group of an ester with the organic group of an alcohol, by mean of which vegetable oils can be converted to methyl or ethyl esters of fatty acids, also called biodiesel. This process involves the coproduction of glycerine, a chemical compound with diverse commercial uses. (10)

- **Mechanical processes:**

Mechanical processes are processes which, unlike the chemical ones, do not change the state or the composition of biomass, they are only responsible for the size reduction or for the separation of feedstock components. In a biorefinery pathway, they are usually applied at the beginning, because the subsequent biomass utilization requires the reduction of the material size within specific ranges, depending on feedstock nature, on the handling and further on conversion processes. The reduction of the biomass size is a mechanical treatment that refers to either the cutting or the converting processes that are responsible to significantly change the particles size, and also the shape and the bulk density of the biomass. Separation processes involve the separation of the substrate into its components, while with extraction methods valuable compounds are extracted and concentrated from a bulk and inhomogeneous substrate. Lignocellulosic pre-treatment methods (e.g. the split of lignocellulosic biomass into cellulose, hemicellulose and lignin) fall within this category (10).

Lignocellulosic biorefinery includes a series of consecutive processes, which consist of:

- Selection of lignocellulosic feedstock
- Pre-treatment (*steam explosion*), where the purpose is to transform the lignocellulosic biomass in a hydrolysable intermediate containing its three main components. Through the Steam Explosion, the biomass is compressed by the vapor and successively reported at the atmospheric pressure. A consequence of this is the fragmentation of the material. The advantages of the process are the low energy consumption and the use of water for the solvent separation or *pulping*
- Extraction
- Recovery of insoluble material. (11)

1.3 Lignocellulosic biomass

Biomass has been defined as “any material, excluding fossil fuel, which was a living organism that can be used as a fuel either directly or after a conversion process” (ASTM 2002). Although such definition of biomass derived fuels is currently in use, the bioprocessing options, divided in aerobic and anaerobic fermentation, able to produce liquid transportation fuels, are of particular importance to any sustainable energy development scheme. The global rise in energy consumption, but also the predicted increase in energy demands in future, the depletion of reserves of fossil fuel and the climate change have converged to make urgent the need to develop more sustainable energy systems based on renewable lignocellulosic biomass. Lignocellulosic materials, as visible in **Figure 3**, are constituted mainly of three polymers, associated with each other in a hetero-matrix to different degrees and varying relative composition depending on the type, species and even source of the biomass: (12)

- **Cellulose:** is the main constituent of plant cell wall conferring structural support and is also present in bacteria, fungi, and algae. When in the form of unbranched homopolymer, cellulose is a polymer of ß-D-glucopyranose moieties linked via ß-(1,4) glycosidic bonds with well documented polymorphs. The degree of polymerization of cellulose chains in nature has a wide range that goes from 10,000 glucopyranose units in wood to 15,000 in native cotton. The repeating unit of the cellulose chain is the disaccharide cellobiose as oppose to glucose in other glucan polymers. The cellulose chains (20–300) are grouped together to form microfibrils, fundamental precursors to form cellulose fibres. The cellulose microfibrils are mostly independent, but the rigid structure of cellulose is largely due to the presence of covalent bonds, hydrogen bonding and Van der Waals forces. Hydrogen bonding within a cellulose microfibril determines ‘straightness’ of the chain but interchain hydrogen bonds might introduce order (crystalline) or disorder (amorphous) into the structure of the cellulose. (12)

- **Hemicellulose:** it differs from cellulose by the fact that it is not a chemically homogeneous material. Hemicelluloses are branched, heterogenous polymers of pentoses (xylose, arabinose), hexoses (mannose, glucose, galactose) and acetylated sugars. They have lower molecular weight, if compared to cellulose molecular weight, and branches with short lateral chains that are easily hydrolyzed. Among the key components of lignocellulosics, hemicelluloses are the most thermo-chemically sensitive. Hemicelluloses within plant cell walls are thought to ‘coat’ cellulose-fibrils and it has been seen that to significantly increase cellulose digestibility, at least 50% of hemicellulose should be removed. (12)

- **Lignin:** it is the second most abundant polymer in nature. It is present in plant cell walls and confers a rigid and impermeable resistance to microbial attack and oxidative stress. Lignin is an amorphous heteropolymer and possesses a network of phenyl propane units (p-coumaryl, coniferyl and sinapyl alcohol) held together by different linkages. Lignin is generally accepted as the 'glue' that binds the different components of lignocellulosic biomass together, thus making it insoluble in water. (12)

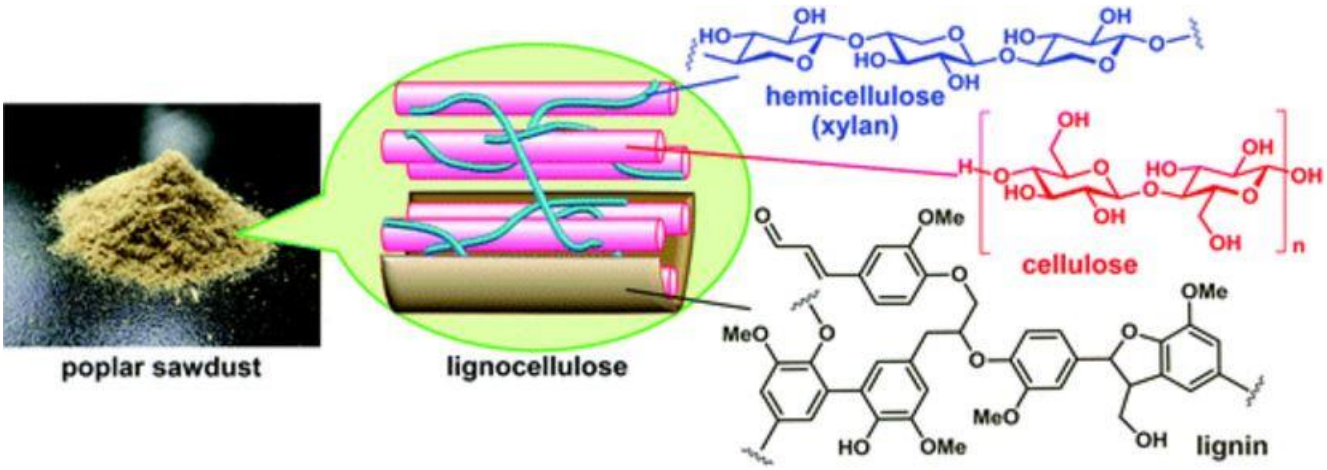

Figure 3 Schematic representation of the lignocellulosic materials (13)

1.4 Lignin (structure and biosynthesis)

In the early decades of 19th century the French chemist Anselme Payen (1795–1871) treated wood with nitric acid and caustic soda reagents, with the recovery of two different products: the first one was called “cellulose” and the other one with higher carbon content was considered as an “incrusting material”, in which the fiber-forming cellulose was imbedded. The Payen’s “incrustation theory” signed the beginning of the history of what latter was named “lignin”, a word derived from the Latin lignum, meaning wood. (14) Lignin is a major component of wood, ranging from 15% to 36% of its dry weight: it is, after cellulose the second most abundant natural polymer on the earth. Lignin is deposited in the cell wall at the end of xylem cell differentiation. It is important since it performs two main activities in wood, which are the xylem sap conduction and the mechanical support. Indeed, its deposition reinforces the walls of the plant cell, providing rigidity, impermeability to water and also protection against pathogens. Therefore, lignin biosynthesis appears in vascular plants of fundamental importance for plant adaptation to an aerial environment and further to the development of trees. Lignin is a highly variable molecule, whose synthesis appears influenced by environmental and physiological parameters such as tree age, cell type or cell wall. Therefore, lignin synthesized by a young tree grown for several months under the sub-optimal conditions of a greenhouse can be rather different from the one synthesized by the same tree, but after several years of growth in another environment. Lignin is the result of the polymerization of elementary units, namely p-hydroxycinnamyl alcohol monomers or monolignols, which differ by the number of methoxylations on their aromatic cycle: this is why, as a consequence, it is better to use the term ‘‘lignins’’ indicative of an array of different polymers, instead of the term ‘‘lignin’’ indicative of a single lignin molecule. In gymnosperms, lignins result mostly from the incorporation of coniferyl alcohol and a small proportion of p-coumaryl alcohol. The phenolic substructures that originate from these monolignols are called hydroxyphenyl (**H**, from coumaryl alcohol), guaiacyl (**G**, from coniferyl alcohol) and syringyl (**S**, from sinapyl alcohol) moieties, and are visible in **Figure 4**. In angiosperms, lignins are composed approximately equally of G and syringyl (**S**) units resulting from the incorporation of sinapyl alcohol. The different proportions between the monolignols affects their linkage within the polymer and successively the structure and properties of the lignin polymer. In accordance, lignins will be more or less condensed, and in consequence, more or less resistant to chemical attacks, whether they are natural or artificial. (15)

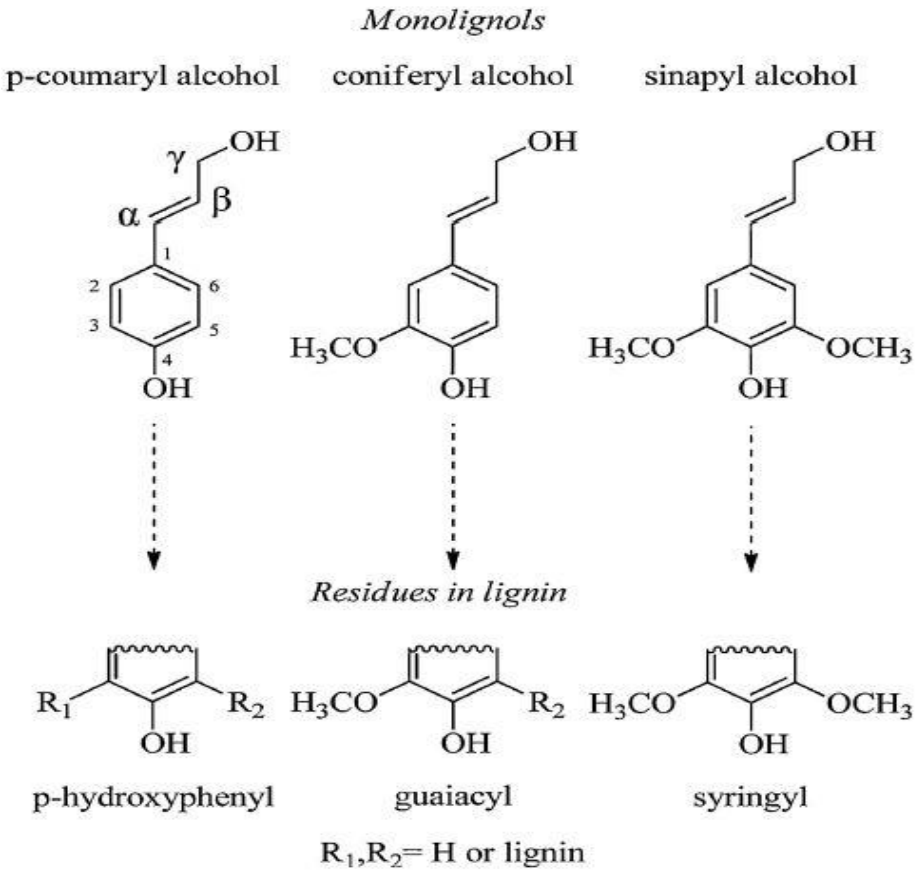

Figure 4 The three main precursors of lignin (monolignols) and their corresponding structures in lignin polymers (16)

Lignin polymerization involves the formation, from oxidation of the monolignols, of phenolic radicals that undergo coupling reactions with analogous radicals produced on growing lignin chains. In the first step, the monolignol phenol is oxidized or dehydrogenated. Since delocalization of the unpaired electron in the conjugated system occur, the resulting phenolic radical is relatively stable. Subsequently, two monomer radicals may couple to form a (dehydro)dimer, thereby establishing a covalent bond between both subunits. Monolignol radicals favor coupling at their β positions, resulting essentially in only the β-β, β-*O*-4, and β-5 dimers (Figure 5).This radical-radical coupling occurs in a chemical-combinatorial way: this means that the ratio of each of the possible coupling products depends largely on the chemical nature of each of the monomers and the conditions in the cell wall. (17)

Then, the dimer needs to be oxidized again to a phenolic radical before it can couple with another monomer radical. This way of acting according to which a monomer (radical) is added to the growing polymer, is termed endwise coupling: the polymer grows one unit at a time. While the coupling of

two lignin oligomers is quite rare in S/G-lignins, it results relatively common in G-lignins, where 5-5 coupling accounts for approximately 4% of the linkages. (18)

During each of the coupling reactions, two radicals are employed in the termination reaction,and each single electron contributes to the newly formed bond, making this type of radical polymerization basically different from the radical chain reactions that occur in the polymerization of several industrial polymers. The average length of a linear lignin chain in poplar plant is estimated to be approximately between the 13-20 units (19). In **Figure 5** it is possible to see the main linkages present in a softwood lignin.

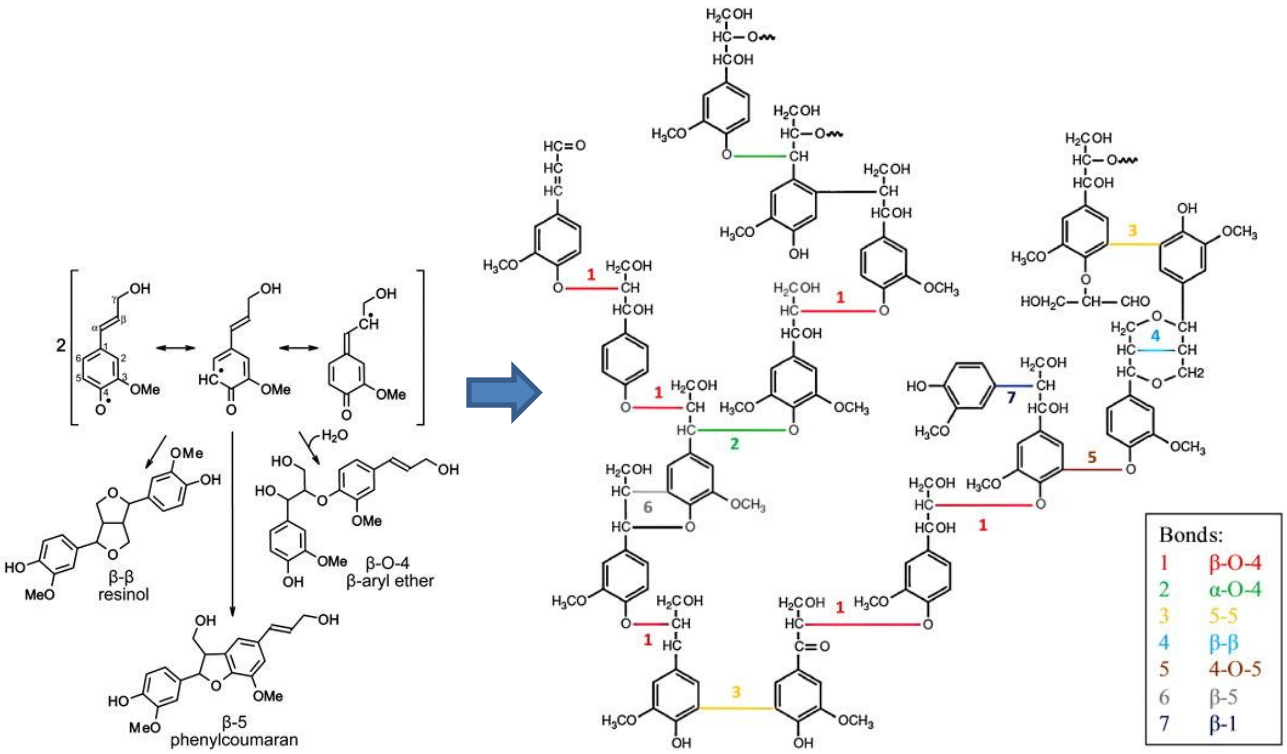

Figure 5 Dimerization of two dehydrogenated coniferyl alcohol monomers (20) ; Main linkages in a softwood lignin (14)

Based on the first lignin structure proposed by Adler in 1977, lignin is recognized as a highly branched polymer with a variety of functional groups: phenolic aliphatic and hydroxyls, carboxylic, carbonyl and methoxyl groups. The main functional groups of a softwood lignin are depicted in **Figure 6**. Its chemical structure has been investigated by many chemical and spectroscopic methods, which are well described in numerous books and publications: some examples are represented by the research

conducted by Pandey on the structure of wood polymers by FTIR spectroscopy (21), by the characterization of lignin through ^{1}H and ^{13}C NMR spectroscopy conducted by Chen et al. (22), and by the computer-assisted molecular simulations achieved by Fadon and Hatcher (23). The huge variety of the chemical sites provides different possibilities for chemical modification and suggests that lignin could play a central role as a new chemical feedstock, particularly in the formation of supramolecular architecture and aromatic chemicals. (16)

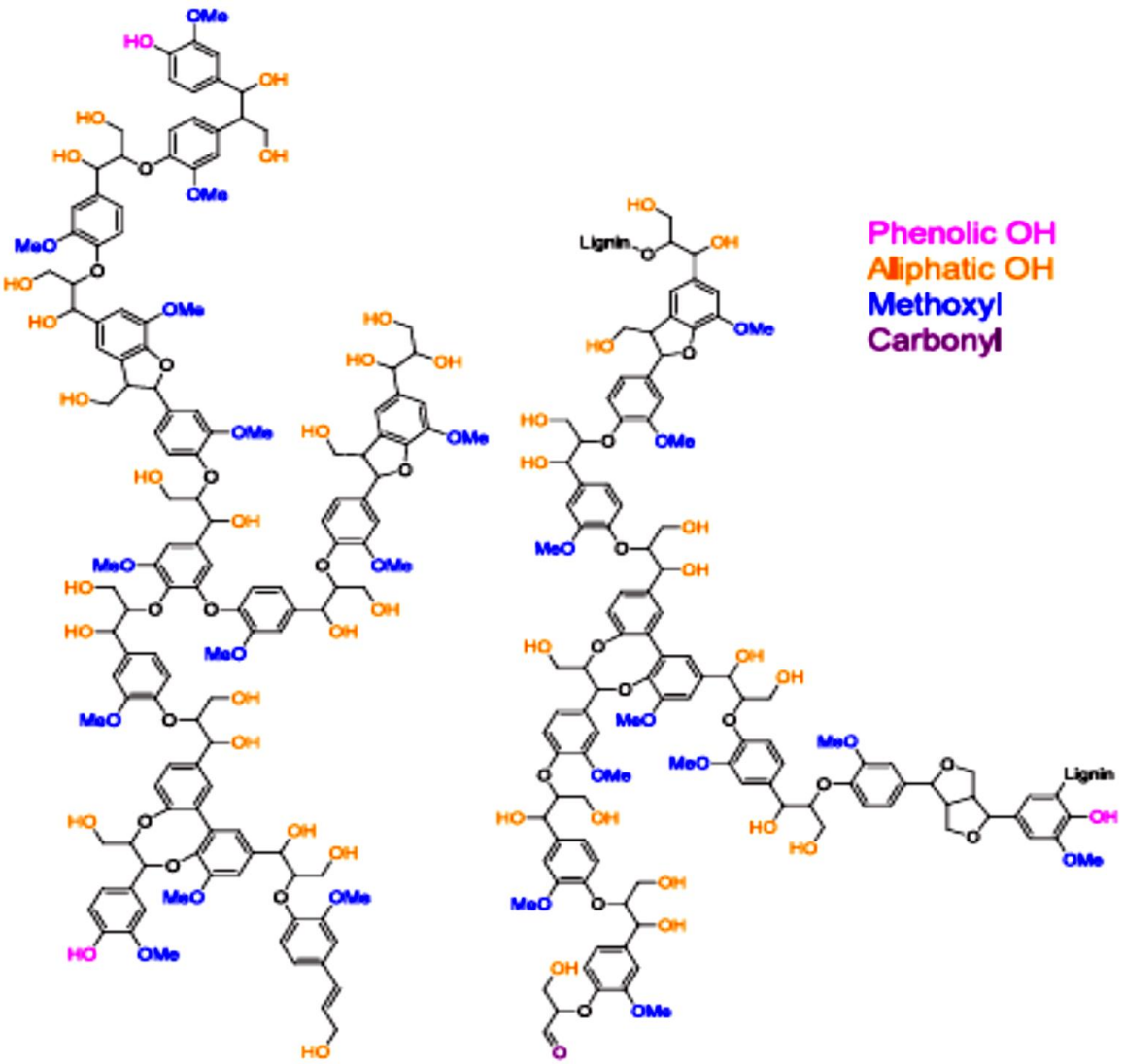

Figure 6 Main functional groups in a softwood lignin (24)

1.4.1 Extraction processes of lignin

Lignin is extracted from the other lignocellulosic parts by means of several treatments. The botanical source, but also the pulping process named delignification and extraction procedures highly influence its final structure, but also purity and the corresponding properties. Common pulping processes are based on the cleavage of ester and ether linkages, then the resulting technical lignins differ considerably from the lignin findable in plants. In this part, attention will be paid on the different commercially available extraction processes that are used to recover these lignins. **Figure 7** shows the classification into two main categories, sulfur and sulfur-free processes, respectively.

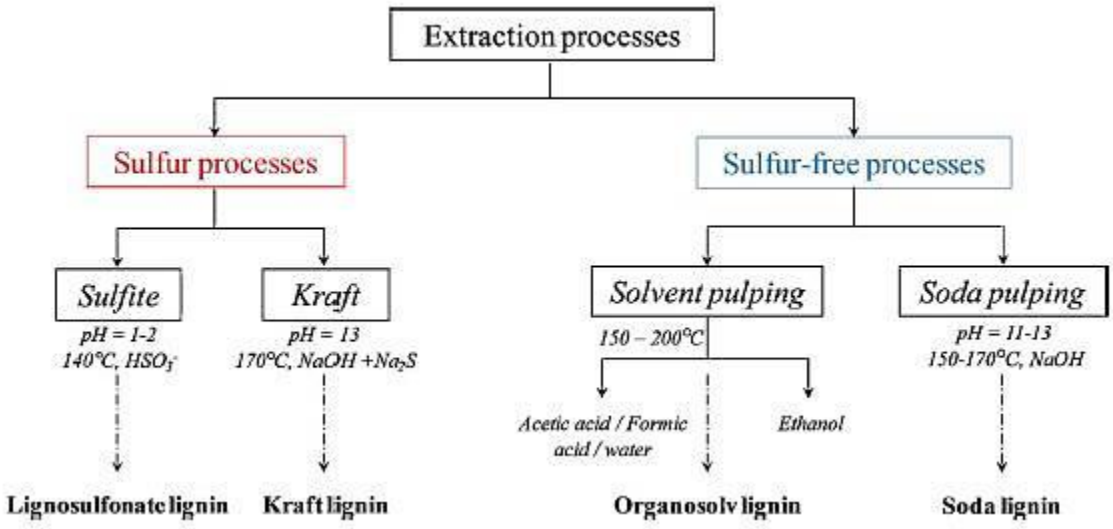

Figure 7 Different extraction processes to separate lignin from lignocellulosic biomass and the corresponding productions of technical lignins (16)

- **Kraft Pulping:**

Kraft pulping is a method of chemical pulping that uses chemical reactions to reach the degradation and dissolution of lignin in order to separate the pure cellulose from wood. An important step of the process is the treatment of biomass with sodium hydroxide and sodium sulfide to reach the cleavage of the ether linkage by sulfide and bisulfide ions. In this process, visible in **figure 8** below, phenolic groups are converted into quiononemethide groups by sodium hydroxide; then hydrogen sulfide ion attacks α-carbon atoms of ether linkages forming a benzylthiolate anion. Next, the β-phenolate anion is released from the benzylthiolate anion to produce free phenolic groups. The free phenolic groups

yield quiononemethide again, and the same process tends to be repeated continuously to cleave more ether bonds and produce always lower molecular weight, soluble fragments. Lignin C-C bonds can be formed only at the last stage of the process, which usually involves a condensation reaction and yields a very robust lignin complex. Kraft lignin behaves as an hydrophobic material at neutral pH and contains approximately 1% sulfur (measured in atomic%) in the form of aliphatic thiol groups. Also other important functional groups in kraft lignin (expressed in w/w%) are methoxyl group (14%), aliphatic hydroxyl group (10%), phenolic hydroxyl group (2-5%), and carboxylic acid group with compositions that can vary depending on the plant source and processing conditions (4-7%). However, as a by-product in paper production, most kraft lignin is still burned as a fuel to produce power in the pulp mill and to recover inorganic components. (25)

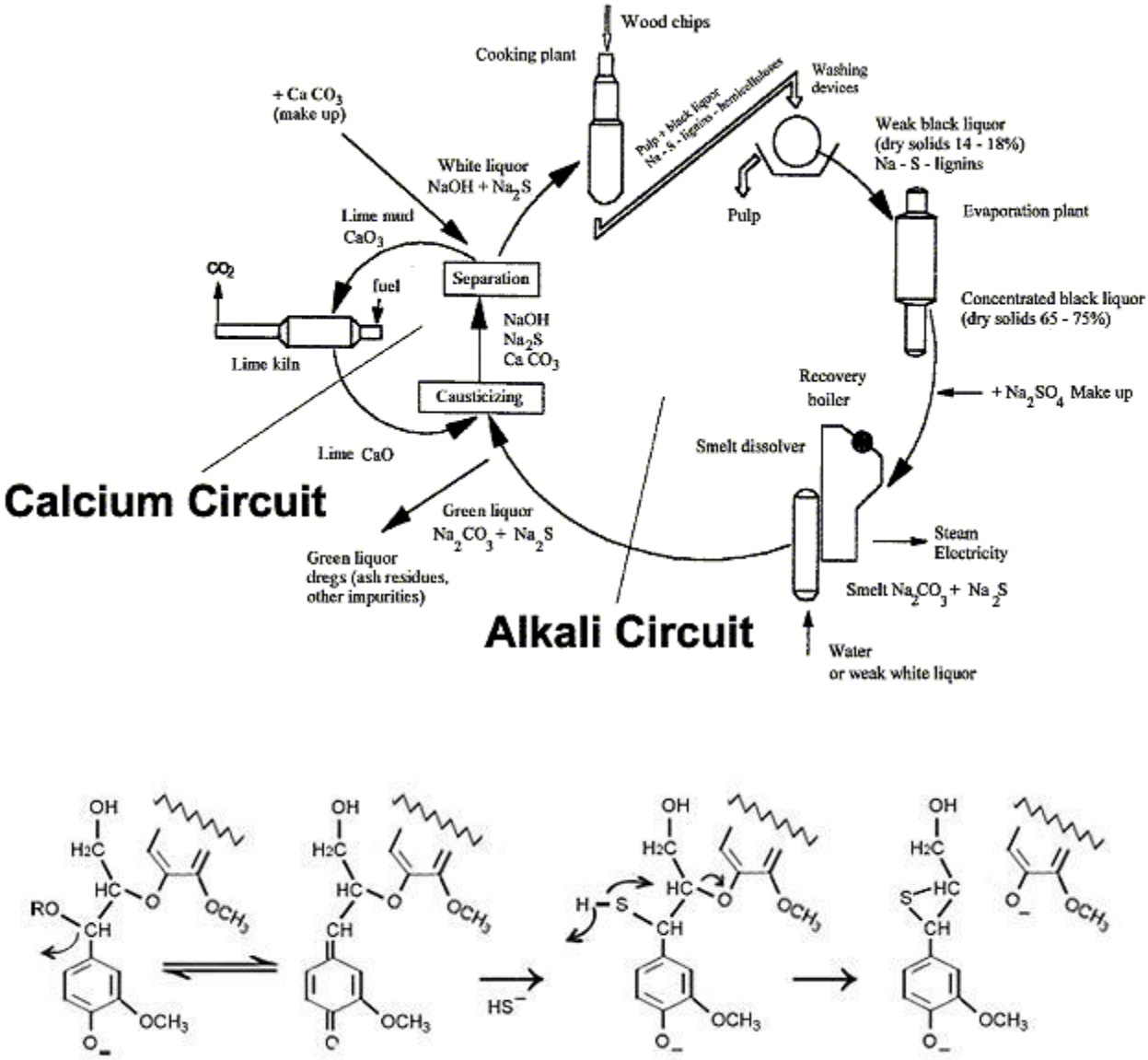

Figure 8 Schematic representation of the kraft pulping process and of the occurring reactions (26)

- **Sulfite Pulping:**

The process of sulfite pulping consists of the reaction of wood or biomass with sulfur dioxide (SO_2), which reacts with water to form sulfonic acid, and bases such as calcium, sodium, magnesium, or ammonium at high temperatures, 125-150 °C, for 3-7 h. This process is acid-catalyzed to obtain the cleavage of α-ether linkage and β-ether linkages during the pulping process. The lignin can be dissolved and separated in aqueous solution due to sulfonic acids which attack the α -carbon of ethers. The resulting lignin has functional groups of lignosulfonic acid, lignosulfonate, carboxylic group together with phenolic/aliphatic hydroxyl groups. Due to the high content of sulfonate, the produced lignin shows an hydrophilic nature, so it is water soluble. Lignin produced by the sulfite process has broad molecular weight distribution and relatively high ash content. The carboxylic acid content is approximately 4%, while the sulfonate content can be 13%. The applications of such materials are limited to the area of animal feeds, particle boards, surfactants, adhesives, cement additives, and stabilizer/dispersing agents. Due to the high content of sulfur, approximately 5-6%, most of the obtained lignin by the sulfite pulping process is used as a fuel for the pulp mill and to recover inorganic components. (25)

- **Soda Process:**

The soda process is the oldest pulping method that included the utilization of sodium hydroxides as the chemical reagents of the pulping process; nowadays, it has been used to process non-wood material, which includes mainly annual plants and agricultural waste, such as wheat straw, sisal, kenaf. In the above mentioned process, biomass reacts with concentrated sodium hydroxide (ca. 1 M) under high temperature (ca. 170 °C) and high pressure (ca. 10 psi). An α -ether bond can be hydrolytically cleaved by this method, resulting in realization of lower molecular weight fragments with increased solubility, making it an effective process for delignification. Anthraquinone (AQ) is often added to the reaction, which oxidizes carbohydrates and forms anthrahydroquinine (AHQ). The AHQ dianion can cleave the β -O-4 ether linkage easily during the process by reacting with quinine methides formed from soda reactions via nucleophilic attack, thus regenerating the AQ. Addition of AQ can significantly increase the rates of delignification. Furthermore, soda lignin has been considered as a precursor for raw materials, since appeared to be the closest one to the natural lignins in a broad range of applications because of the absence of sulfur functionality. (25)

- **Organosolv Lignin:**

Organosolv processes include a wide family of methods used to delignify biomass. Common features, for example, include mixtures of water and organic solvents to remove lignin from the wood or other biomass as well as the use of acid or base catalysts. Ethanol, methanol, or acetic acid have been used, and it is known that the organosolv process is more effective in treating annual plants and hardwoods. Organosolv lignin is sulfur-free, and the molecular weight is low with respect to other lignin production methods, generally around 5 kDalton, although this will depend on the organic solvent used, with carboxylic acids often being less effective at preventing recombination than alcohols. Many organosolv processes have been investigated extensively and tested in pilotscale plants, including Alcell, Acetosolv, and Milox. They possess several advantages, with respect to the other extraction processes, like the fact that they involve an acid catalyst or are performed in an acidic solvent, which allows use of lower temperatures than traditional pulping methods, or that they generally avoid use of sulfur- and chlorine-based chemicals. (25)

1.4.2 Applications of lignin

Lignin can be used in several applications, due to its many properties and due to its chemical structure and composition: thanks to the high energy content related to the presence in the main skeleton of aromatic rings, it is mainly utilized as black liquor for generating power, process steam and also chemical recovery in the pulp mill. A few pulping mills convert lignin into value added products: thermochemical techniques, for example, such as gasification of lignin to syngas or its pyrolysis to bio-oils can contribute to value-addition. Gasification of black liquor on a large scale results in more efficient power generation. Due to the change of the modern industry imposed by the nowadays needs, a transformation of lignin occurred from a mere fuel source into a key biorefinery process stream: it can be processed further to ethanol, mixed alcohols, green fuels or other syngas products. However, the current focus on greater utilization of waste products has driven research to the isolation, structural modification and utilization of lignin. Below in **Figure 9** different products obtained from lignin have been listed in increasing order of value. (27)

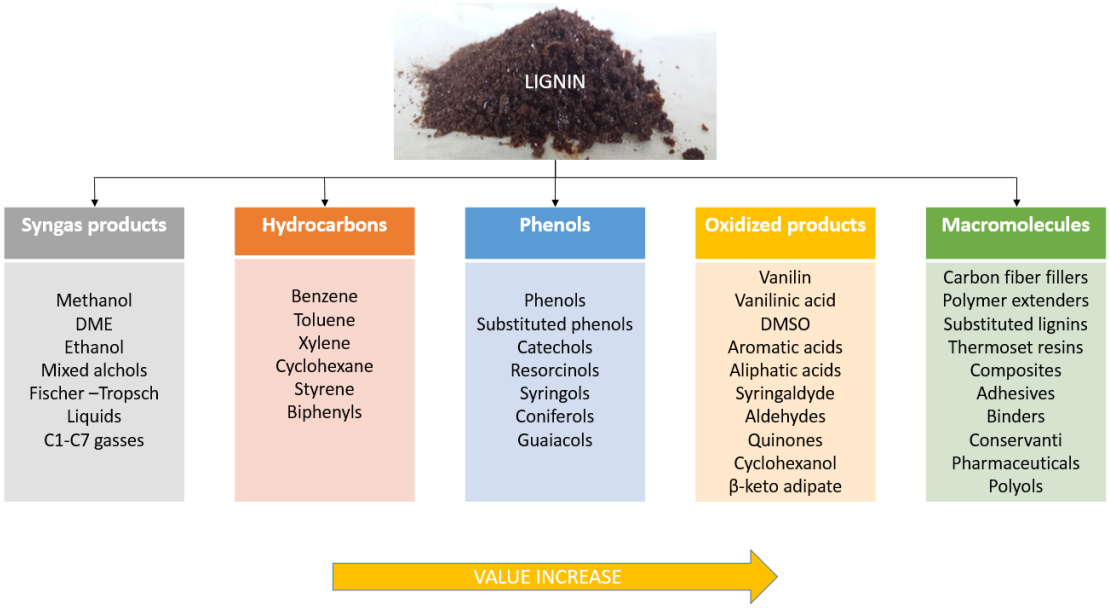

Figure 9 Lignin products listed in increasing order of value (28)

Several examples of applications available in literature have been reported hereafter.

Zhang et al. used a softwood lignin as both crosslinker and reinforcing agent in silicone elastomers: silicone elastomer networks are usually prepared using the Piers–Rubinsztajn reaction by means of crosslinking reaction of hydrosilicones with alkoxysilanes in the presence of fillers. Instead of using tetraethyl orthosilicate (TEOS) as a crosslinker, the reinforced silicone elastomers were obtained from the reaction of hydrogen-terminated polydimethylsiloxane (H-PDMS-H) with softwood lignin, catalyzed by tris(pentafluorophenyl)borane [$B(C_6F_5)_3$]. The modulus and elongation-at-break of the elastomers were influenced by lignin content and molecular weight of silicones, and the elastomer exhibited excellent resistance to high temperature aging and also a moderate resistance to solvent extraction, so it was possible to deduce that lignin can serve as efficacious green elastomer filler (29).

Jiang et al. realized an in situ dispersion of lignin at submicrometer size in epoxidized natural rubber (ENR) by means of a high-temperature dynamic heat treatment (HTDHT). Rheology analysis indicated that the ring opening reaction between lignin and ENR occurred at 160°C, and further was confirmed by FTIR. DMA and morphology analysis demonstrated that lignin was perfectly dispersed and interacted strongly with ENR. The mechanical properties of the lignin/ENR composites were significantly improved by using the dynamic heat treatment: compared, indeed, to the rubber composites obtained by direct mixing, the tensile strength and tear strength of the heat treated rubber composites filled with 40 parts per hundred rubber lignin were increased by 114% and 23%, respectively. Especially, the 300% modulus of the rubber composite thermally treated was increased by 400%. X-ray diffraction analysis showed that the reinforcement of the composites originated from the presence of lignin rather than the strain-induced crystallization of ENR (30).

Hilburg et al. synthesized nanocomposites based on synthetic polymers grafted from kraft lignin with average dimension of the particle of 5 nm by means of an atom transfer radical polymerization (ATRP). First of all were prepared lignin macroinitiators, then both polystyrene and poly(methyl methacrylate) were polymerized with a certain degree of polymerization resulting in materials having lignin mass fractions of 4.5%, 8.3%, and 22.1% for the poly(methyl methacrylate) samples and 3.2%, 7.1%, and 19.6% for the polystyrene samples. The tensile tests showed that although the modulus was decreased, an enhance in toughness of all nanocomposites compared to homopolymers was registered, and the poly(methyl methacrylate) grafted samples had nearly twice the ultimate elongation as the polystyrene grafts at high graft density. Both types of grafted nanocomposites presented values of toughness that were greater than 10 times that of the corresponding kraft lignin/polymer blend system, indicating the potential of ATRP as the basis for the 'one component' composite approach towards more sustainable polymeric materials. The DMA test was performed to measure softening temperatures, and both the polystyrene-grafted and poly(methyl methacrylate) grafted nanocomposites had a peak in the loss modulus that was higher than the corresponding homopolymer, consistent with strong polymer/lignin interactions. The results showed that atom transfer radical polymerization is well suited for preparing lignin-based thermoplastics and could be the basis for hybrid materials that make effective use of this important renewable resource (31).

Griffini et al. realized lignin-based thermoset polyurethane (PU) coatings with a high lignin content. These materials were obtained through the extraction of the soluble fraction of a raw kraft lignin sample by means of the 2-methyl-tetrahydrofuran (MeTHF) solvent, and subsequently directly crosslinking the MeTHF-soluble lignin fraction with a toluene diisocyanate (TDI)-based polyisocyanate at different weight ratios. The characterization of the PU materials highlighted an improved thermal stability, an increased film forming ability, and an higher hydrophobic character with respect to the uncrosslinked lignin precursor. By means of AFM measurements the elastic modulus of the PU materials was determined. Furthermore, the lignin-based PU materials were found to exhibit high adhesion on different substrates like metals, glass and wood. The results of this study established that the development of lignin-based thermoset PU systems through the direct reaction of chemically-unmodified fractionated lignin with polyisocyanates represents an interesting strategy, and may find application in the field of high-performance bio-based coatings and adhesives (32).

Cateto et al. synthesized rigid polyurethane (RPU) foams using lignin-based polyols obtained by oxypropylation of four distinct lignins: Alcell, Indulin AT, Curan 27-11P, and Sarkanda. Two different ratios of Polyol formulations with two lignin/propylene oxide/catalyst content (L/PO/C) were chosen (30/70/2 and 20/80/5). The preparation of RPU foams required the embedding inside a polyol component the lignin-based one at contents ranging from 25 to 100%. A 100% commercial polyol-based (Lupranol 3323) RPU foam was also prepared and held as the reference. The characterization of the RPU foams was done in terms of density, compressive modulus, and conductivity. Cell

morphology and size estimation were accessed by SEM analysis. Moreover the biodegradation of the Alcell- and Indulin AT-based foams was estimated using respirometry tests. The Alcell and Indulin AT-based polyols together with the 20/80/5 Curan 27-11P-based one led to RPU foams with properties quite similar to those obtained in the reference foam (33).

Peng et al. synthesized hydrogels from acetic acid lignin by chemical crosslinking with NCO-terminated polyurethane ionomers (IPUI). The swelling ratio of hydrogels was found to increase with pH. The hydrogel prepared at the specific mass ratio of m_{AAL}/m_{IPUI}: 0,35:1 presented maximum swelling ratio in pH 6.8 buffer solutions. Through thermogravimetric analysis it was demonstrated that the thermal stability of the hydrogels has been improved by the introduction of lignin. According to the data of release experiments for ammonium sulfate, the hydrogels from acetic acid lignin can be used as coating materials to prepare a slow-release fertilizer (34).

Nonaka et al. obtained a cured lignin-epoxy resin by dissolution of Kraft lignin or ozone oxidation kraft lignin in the 1% sodium hydroxide water solution at 60 °C and subsequently mixing with the water-soluble epoxy resin, polyethylene glycol diglycidylether (PEGDGE), and/or the emulsified bisphenol-A type epoxy resin. The resulting mixture is crosslinked with toriethylenetetramine TETA. The results showed that there are little differences in performance properties between the epoxidized lignin systems with and without ozone oxidation lignin, and that the heat curing at 150 °C provides a good adhesion performance for the system even if the system contains the lignin up to 50 wt%. Although the Tg of the epoxidized lignin system depends on the type of curing agent it is combined with, it is also able to have the Tg below the ambient temperature. In this case, each lignin-based system has higher loss tangent values in a wide temperature range around the ambient temperature and has a lower elastic modulus at the ambient temperature. This gives a clear indication that the damping material can be recommended as one of the applications for this type of lignin-epoxy resin (35).

Migita et al. provided a lignin-based epoxy resin starting from the addition of Acid (hydrochloric or sulfuric acid) and phenol derivatives to kraft lignin to cause the cleavage of lignin intermolecular bond and at the same time to generate the phenolic hydroxyl group in the molecule, followed by epoxidation of the phenolic hydroxyl group with epichlorohydrin (ECH). The epoxy resin is subsequently crosslinked with diethylenetriamine (DETA) or phthalic anhydride for to be used as adhesive (36).

The huge variety of examples previously cited showed that lignin can be applied as: macromolecular building block in different classes of polymers, crosslinker and reinforcing agent in silicone elastomers, reinforcing comonomer in epoxidized natural rubber, comonomer in PMMA/PS thermoplastic materials and in PU coatings and foams, epoxy resin for adhesives.

Particular attention will be now dedicated to three main functionalizations and applications of this versatile polymer, and some of the main examples encountered in literature will be resumed below in three macroareas.

- **Esterification of lignin:**

Polyesters are among the most promising families of polymers based on renewable resources, thanks to their unique and vast array of properties, and also because the bio-based monomers for polyesters are relatively easy to access (37). Among the many sources of building blocks for the synthesis of polyesters, carbohydrates, vegetable oils, proteins and lignin are for sure the most interesting ones (38). The biomass components can be subjected to a set of transformations to obtain renewable chemical building blocks for the preparation of sustainable polymers.

Thielemans et al. esterified Kraft lignins both hardwood and softwood with several anhydrides like acrylic anhydride, propionic anhydride, butyric anhydride, methacrylic anhydride and maleic anhydride to alter their solubility behavior in nonpolar solvents, such as styrene-containing thermoset resins. The esterification reaction was able to reduce the amount of waste products, and can be easily tuned up. With the increase of the carbon chain length on the ester group it was found that the solubility of lignin in nonpolar solvents improved, for example the butyrated lignin was completely soluble in styrene. With respect to the saturated analogues, the esterification with unsaturated groups such as methacrylic anhydride, improved the solubility to a lesser extent. The solubility behavior of the modified lignin was described according to the Flory-Huggins solubility theory, combined with the predictive method of Hoy. The main target was to obtain a styrene soluble kraft lignin that could be used in unsaturated polyesters and vinyl esters, and was achieved with fully butyrated kraft lignin and a butyrated/methacrylated lignin. The solubility of the latter is governed by the ratio between butyrate and methacrylate. The reaction rate constants for the butyration and methacrylation reactions were also determined and the aromatic hydroxyl groups were found to be consistently three times more reactive than the aliphatic ones. (39)

Fox et al. characterized corn stover and rice straw lignin samples received from ethanol pilot plants, along with softwood kraft lignin samples, by means of pyrolysis GC-MS, ^{13}C-NMR spectroscopy, and also permanganate oxidation degradation. After that lignins were subjected to an esterification reaction (**Figure 10**) with either acetic, propionoic, or butyric acid anhydride using 1-methylimidazole as a catalyst in a pyridine-free reaction, and the thermal properties of the products were evaluated. Solid state NMR showed that the lignin coming from rice straw contained 18% of residual polysaccharides. From pyrolysis GC-MS it was found that the softwood kraft, corn stover, and rice straw lignins were *G* – type, *H*/*G*/*S* – type, and *G*/*S* – type, respectively. However, some discrepancy was apparent between the pyrolysis and permanganate oxidation studies as to the ratios of the

monomeric makeup of the lignins. While kraft and rice straw lignins seemed to have high degrees of condensation, instead the corn stover lignin was uncondensed. Little to no increase in solubility was noticed for corn stover or rice straw lignin esters in organic solvents. Glass transition temperatures (*Tg*) of the lignin derivatives were determined through differential scanning calorimetry (DSC), dynamic mechanical analysis (DMA), and parallel plate rheometry. The resultant lignin ester derivatives were shown to have discrete glass transition temperatures. Tg were dependent on lignin type and acyl substituent. Also moderate viscous flow was registered under the rheological conditions tested, denoting that the lignin-based thermoplastics could be molded into products. The flexural properties of the lignin ester samples were found to be comparable to common plastics such as polypropylene and polyethyleneterephthlate (40).

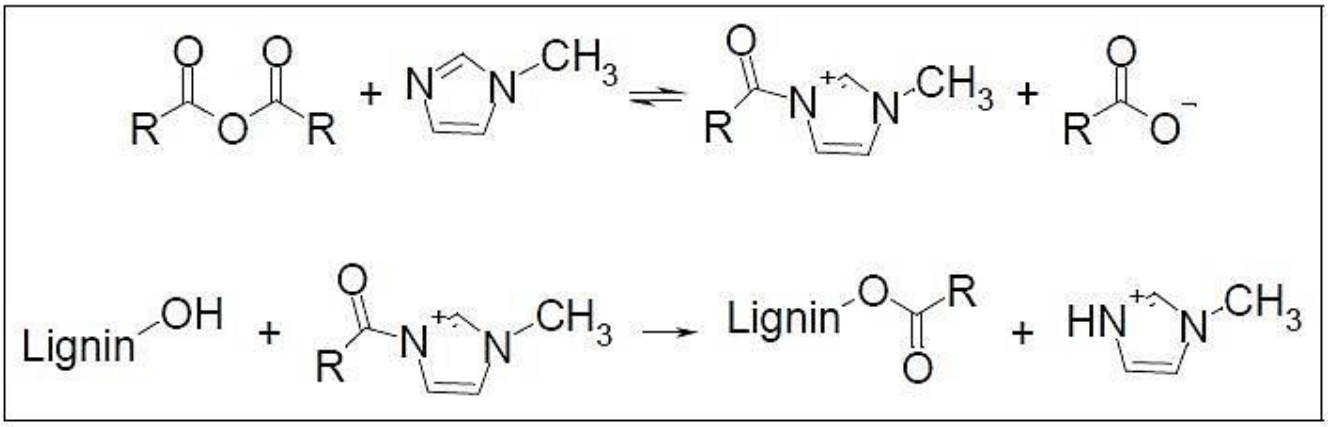

Figure 10 Reaction mechanism for lignin esterification using 1-methylimidazole as a catalyst. R = -CH3 for acetic anhydride, -CH2CH3 for propionic anhydride, and -CH2CH2CH3 for butyric anhydride. (40)

Sivasankarapillai et al. have been developed hydrogen bonded/crosslinked polymer networks based on lignin. This new type of polymeric material was obtained from the combination of an industrial lignin and a highly branched poly(ester-amine) (HBPEA) obtained by melt polycondensation of 1,1,1-triethanolamine (TEA) and adipic acid (AA) (**Figure 11**). The lignin-HBPEA polymers showed to be insoluble in common organic solvents and were characterized by FTIR and NMR spectroscopies. From thermo-mechanical measurements it was found that melt mixing HBPEA with 40% lignin gives a flexible and tough material , with a glass transition temperature of 7.7 °C and an elastic modulus E'of 3.5 GPa. The hydrogen bonding recognition was based on the many hydroxyl groups in lignin and on aliphatic ester groups from HBPEA. The extent of interactions could be controlled through the variation of the amount of lignin added. These networks were thermally reversible and have highly tunable mechanical properties that were controlled by the extent of interactions. High level of mechanical properties could be achieved if the addition of lignin-poly (ester-amine) covalent cross-links was done. This study shows that the poly(ester-amine) structure plays an important role in the

thermo-mechanical properties: indeed if the spacer length between lignin and tertiary amine unit was varied , materials with various thermo-mechanical properties were obtained from the same parent polymer backbone (41) .

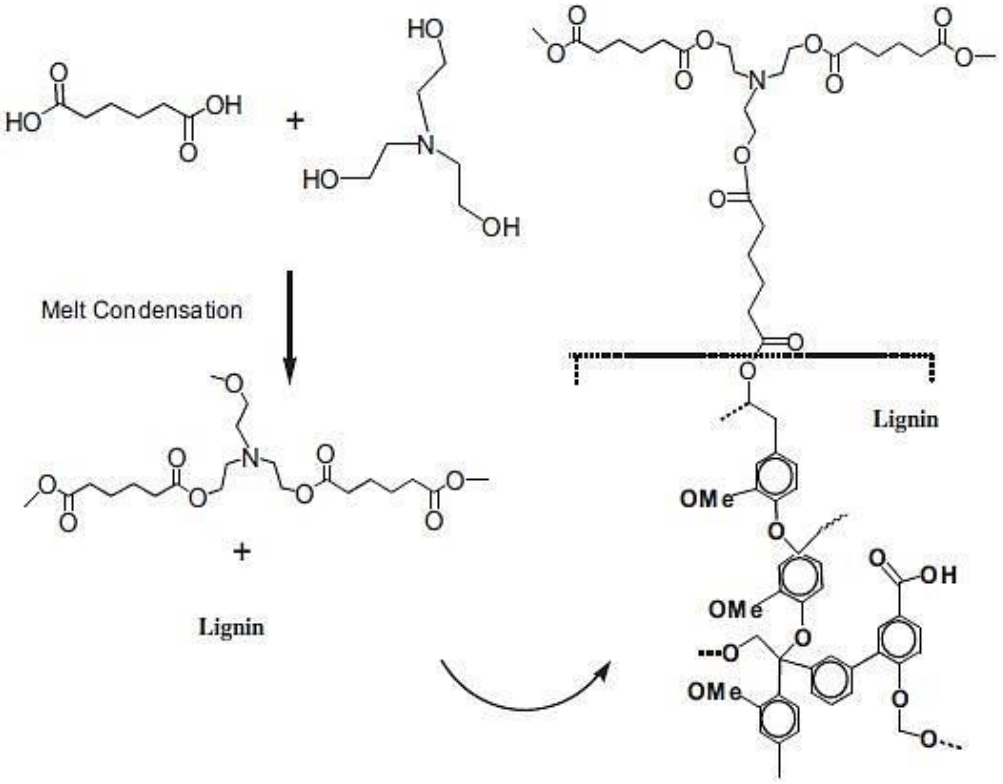

Figure 11 Schematic representation of synthesis of L-HBPEA (41)

Chen et al. synthesized esterified kraft lignins by reaction with maleic anhydride (MA), succinic anhydride (SA) and phthalic anhydride (PA) in acetone solutions (**Figure 12**). Esterified lignins were examined through ATR-FTIR, slid state ^{13}C-NMR spectroscopy, TGA and DSC. The highest gain percent in weight was obtained with PA modification. From the spectroscopic analysis it was found that there is a decrease in hydroxyl content and an increase in carbonyl and ester groups of the modified kraft lignin due to the esterification reaction. The hydrophobic properties increased, as well as the thermal stability of SA and MA modified lignins with respect to the unmodified one. Less efficient was found instead to be the PA modified lignin as far as the thermal stability was concerned. According to this study it seems that to produce high performance composites it is necessary to only modify the basic properties of lignin with esterification reactions. (42)

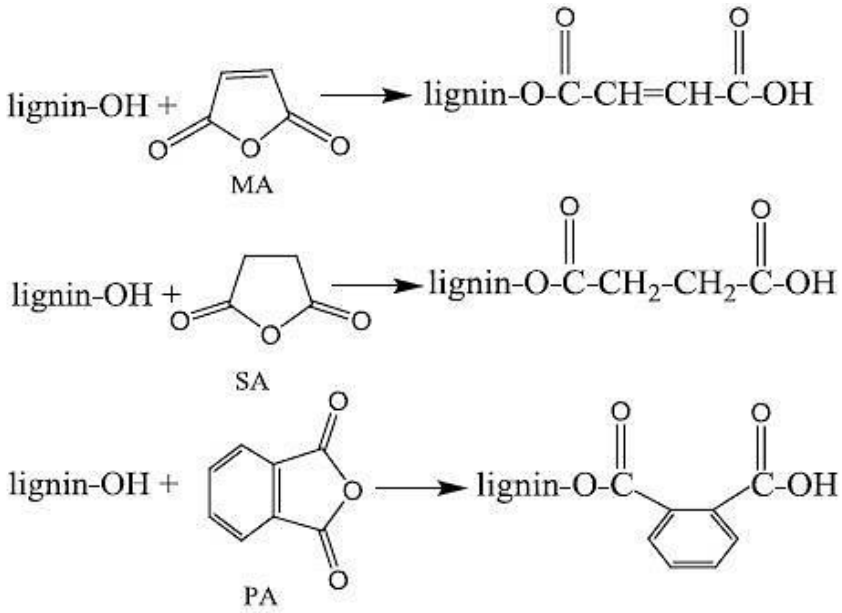

Figure 12 Schematic representations of lignin reactions with MA, SA and PA (42)

The incorporation of carboxylate groups (-COO-) on lignin macromolecule by means of cyclic anhydrides such as succinic anhydride (SA) has received an increasing attention, since it represents an easy way to introduce new material properties to the parent lignin. This modification, indeed, leads to the formation of carboxyl groups covalently bonded to lignin that may represent new sites upon which further reactions can take place.
It is therefore of interest to study the effect of the reaction of SA with lignin on the properties of the resulting material, including molecular weight, glass transition temperature, the thermal stability, the adhesion properties, the mechanical properties. (37)

- **Silanized and anti-corrosive lignin-based coatings for metallic substrates:**

The antioxidant capacity of lignin has been widely studied, since it represents a natural free radical scavenger. Due to the high content of different functional groups (phenolic and aliphatic hydroxyls, carbonyls, carboxyls, etc.) and its phenylpropanoic structure, lignin can act as a neutralizer or inhibitor in oxidation processes, being able to stabilize reactions induced by oxygen radicals and their derived species (43).

Hussin et al. have been investigated the inhibitive effect of ultrafiltrated oil palm fronds (OPF) lignins on the corrosion of mild steel in a solution 0.5 M of chloridric acid (HCl) by means of electrochemical impedance spectroscopy (EIS), potentiodynamic polarization (PP) and weight loss measurement. The presence of smaller lignin fractions is responsible for the remarkably reduction of the corrosion rate of mild steel. The highest corrosion inhibition efficiency for all ultrafiltrated lignins was attained at maximum concentration of 500 ppm (IEP.Soda: 87% > IEP.Organosolv: 83% > IEP.Kraft: 81%). The

results obtained from this corrosion test evidence that all ultrafiltrated lignins behaved as an inhibitor of mixed-type with predominant anodic or cathodic effectiveness whether it is organosolv lignin or alkaline lignin. It was deduced that the inhibition process was spontaneous and the inhibitors were mainly physically adsorbed onto the mild steel surface (44)

Vagin et al. executed the electropolymerization of water soluble lignin derivatives (lignosulfonates, **Figure 13**) on steel surface: lignin was transformed into corrosion protective layers by its electropolymerization on steel surface. The solutions throughout this work were prepared using distilled water. For the elaboration of working electrodes, deoxidized high-carbon steel (carbon: 0.06–0.12% mass, Mn: 0.25–0.5% mass, Si: 0.05–0.15% mass) was employed. The standard corrosion inhibitor COREXIT SXT-1003 was used as a reference inhibitor. In cyclic voltammetric regime deoxidized high-carbon steel was immersed in buffer solution of lignosulfonate saturated with argon under a continuous argon flow above solution. Then the system was left free to equilibrate until a stable value of open circuit potential was achieved. Afterwards the electrode was cycled from the open circuit potential value up to 0.5–1.5 V at a rate of 20 mV/s. Alternatively, a potentiostatic deposition was made at a constant potential recording current–time dependencies. It was noticed an appearance of anodic current of lignin oxidation and a subsequent considerable decrease in current at high anodic potentials, as already confirmed by the knowledge of lignin oxidative polymerization. Ionic strength affects a potential of lignin oxidation: an increase of ten times in the KCl concentration (from 0.1 to 1 M) causes a decrease in oxidation potential of 1 V. The polymerization potential can be sufficiently decreased by an increase in ionic strength of the growing solution. Lignosulfonate electropolymerization led to the considerable corrosion protection effect of carbon steel. It was observed a decrease in corrosion rate on steel surface after lignosulfonate electropolymerization of more than three times, exceeding protective effect of standard commercially available corrosion inhibitor (45)

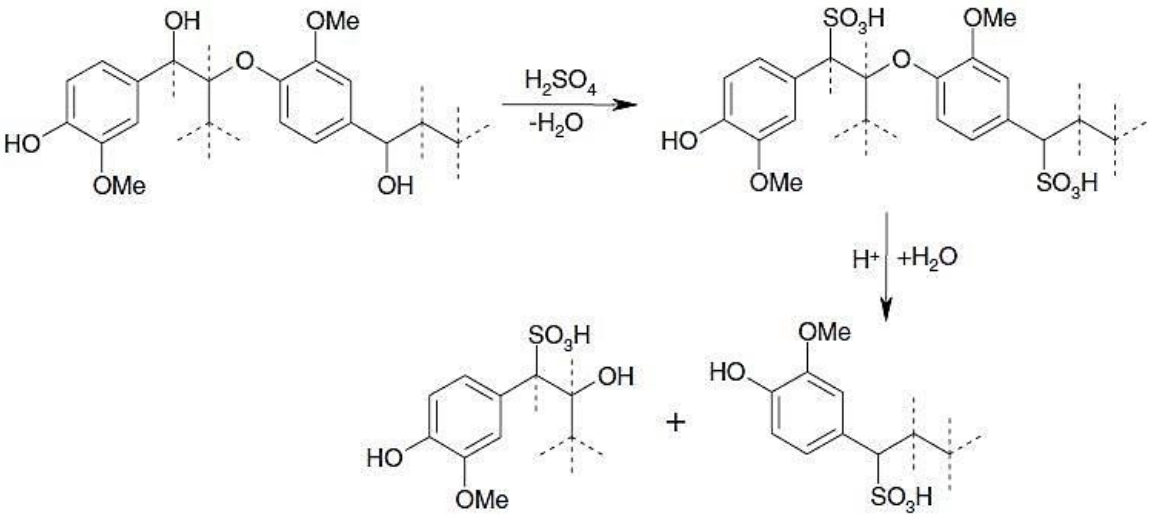

Figure 13 lignosulfonate process (45)

Pan initiated a study on the chemical and physical bases of general chemical antioxidants, using a biopolymer, i.e., coniferyl-alcohol lignin to be used as asphalt binder for industrial applications. Oxidative aging of asphalt is a chemical process that continuously takes place, involving the reactions between oxygen molecules and species of bulk asphalt during its service life; this could lead to significant alterations to the desired physical properties of asphalt. Nowadays to alleviate asphalt aging a common practice consists of using different chemical additives or modifiers as antioxidants. The current state of knowledge in asphalt oxidation and antioxidant evaluation is focused on monitoring the degradation in asphalt's physical properties, above all the viscosity and ductility, which although meeting direct engineering needs does not contribute to the fundamental understanding of the aging and anti-aging mechanisms. A quantum chemistry (QC) based chemophysical environment has been developed in this study; it was able to analyze the various chemical reactions between asphalt component species and oxygen, as well as the incurred physical changes. The techniques of X-ray photoelectron spectroscopy (XPS) was used to prove the validity of the lignin-modified and unmodified asphalt models, from which the XPS results showed high agreement to the model predictions. From these models two distinct stages of asphalt aging can be identified according to the composition and the structure of generated chemical species and their generation speeds. Asphalts initially exhibited a high chain-breaking trend and a high reactivity with oxygen, and caused a rapid formation of light molecular weight alkanes and sulfoxides. This formation was followed by a slower rate of oxidation and hardening. Different oxidation mechanisms were effective during these two periods. During the initial spurt, sulfoxides are the major oxidation product that controls the increase of viscosity; after that, ketones become the major product. The ratio of ketones to sulfoxides formed therefore was dependent on sulfur content in asphalt. The oxidation of asphalt and lignin involved many stable radicals, and a number of intermediate chemicals that could only be observed at the atomic scale due to the high chemical instabilities of such intermediate products. Significant decomposition of saturates and evaporation of small-molecular-weight hydrocarbon were observed. Ketones and sulfoxides account for most of the oxidative reactions in the simulated asphalt. Therefore for the oxidative hardening of asphalt in typical service conditions, chain breaking of saturates, sulfoxidation, and ketonization at benzylic carbons are the major mechanisms. Lignins, when added in asphalt and not oxidized, will slow down the aging speed of asphalt. Also, usually added in solid powders, lignins can increase asphalt's stiffness. Lignins in general are more resistant to oxidation than asphaltenes and resins in asphalt under the same conditions. However, lignins do get oxidized at temperature T>150 °C and/or raised oxygen partial pressure, generating vanillin and glycolaldehyde. This means that when added in asphalt, the mixing temperature needs to be controlled to prevent the oxidation of lignin (46).

Abu-Dalo et al. studied the effectiveness of sulfonated Kraft lignin (LS) as a material for the corrosion inhibition of steel bar grade 60 (ASTM A615) in systems responsible for the water distribution. Potentiodynamic polarization and electrochemical impedance methods were utilized. Sulfonated lignin was evaluated primarily for iron-based materials in water distribution systems. The experiments executed on different solutions simulated internal conditions of water distribution pipelines without or with different corrosion inhibitors. While potentiodynamic polarization and electrochemical impedance were used to evaluate the corrosion resistance of iron-based material's under these conditions, the linear polarization resistance (LPR) tests instead were used to compare the efficiency of the corrosion inhibitor. The potentiodynamic polarization studies showed a reduction in the pitting potential to more noble potential for protected corrosion cell. The electrochemical impedance spectroscopy tests denoted an increase in the corrosion resistance for iron-based material treated by sulfonated lignin. Based on that, the sulfonated lignin optimal dosage was found to be 0.3–0.4 mg/L. The conducted polarization resistance tests showed a decrease in corrosion rates of sulfonated lignin treated iron. This study showed that lignin provided an increase in the protection of iron-based materials in water distribution pipelines through the inhibition of corrosion (47).

- **Lignin-based crosslinked matrices for composite materials:**

Thermosets are materials obtained by an irreversible curing reaction of the resins. The curing process creates covalent bonds between the reactive monomers and generates a network that cannot, unlike the thermoplastics, be remelted again. This gives advantages in terms of chemical and mechanical resistance and thermal stability which are fundamental properties for composite manufacture. Moreover, since the components before the curing usually have a low viscosity (compared to thermoplastics) they are considered ideal for wetting reinforcing fibers. Therefore the most common ones are, for example, unsaturated polyester resins for glass-fiber composites, and epoxy resins for carbon fiber composites. Lignin on the other way, showing an highly branched structure, functional groups such as hydroxyls, and free ring positions in the aromatic monomers, seems to be an ideal bio-based candidate to be employed in resin formulations for thermosets and thermoset composites (25).

Yin et al. prepared a crosslinked biomass-polymer composite containing a lignin amount of up to 60% through blending with an epoxy resin and a polyamine using a hot press molding process. The characteristics of the curing reaction between lignin and epoxy were studied be means of DSC and FTIR analysis. Through SEM, DMA, TGA indeed was investigated the effect of molding temperature and pressure on the mechanical properties and on the microstructure of the composite. Results showed that the composite properties like bending strength, Tg, impact strength, thermal stability were heavily influenced by the molding process. A good interfacial combination resulted between lignin and epoxy resin. With the increase of the molding temperature and pressure this combination

tended to further improve, resulting also in an increase of the ductile fracture in the fracture surface of the composite (48).

Canetti et al. realized a Poly(ethylene terephthalate) (PET) compounded with lignin (L) by a single-screw extruder. It has been studied the influence of lignin presence and its content on the thermal properties and on the crystalline structure of PET. From morphological analyses arose good dispersion of the lignin particles in the PET matrix. Techniques of Polarizing optical microscopy (POM) and small-angle X-ray scattering (SAXS) were carried out to measure the dimension of the lignin particles. The influence of lignin on the overall isothermal crystallization of PET was investigated by means of differential scanning calorimetry (DSC). The particles acted as nucleating agent in the composite and increased the crystallization rate. The crystallization process was composed of primary and secondary stages. As the content of lignin was increased in the composite, the primary crystallization progressively proceeded toward higher percentage of the crystallizable fraction of PET. As evidenced by SAXS and wide angle X-ray diffraction (WAXD), the presence of lignin produced a noticeable enhancement of PET crystallinity and crystal dimensions (49).

Siahmed et al. realized a composite material with polymer matrix (unsaturated polyester) reinforced with the lignin at various proportions and its mechanical and physico-chemical characteristics were compared to another type of composite material constituted of polymer matrix (unsaturated polyester) reinforced with Alfa fibers. The characterization of these composites materials was carried out through tensile and thermal degradation tests under isothermal conditions. In order to explain the deviation from the linear profile, in terms of weight losses, a mathematical model has been used to show that the energy of degradation is the same for all temperature ranges. This model was able to predict the activation energy (48 kJ/mole*K), which corresponds to the process of off-gassing, break of macromolecular chains and weight loss. The lignin extracted from Alfa grass has been obtained by means of sodium hydroxide in order to eliminate the main hemicellulose after a fragmentation step. A powder was obtained, constituted by particles of different size. The scanning electron microscope indicated that lignin has a polygonal morphology of various sizes. Moreover the UV / visible spectrum and FT-IR showed phenolic structure, a carboxylic function and a double bonds. The absence of absorption within the range 1750–1659 cm^{-1} confirmed the disappearance of the hemicellulose in the soda lignin. Lignin can replace partially the phenol of the pure resin and can behave dually as binder and as a load (50).

1.5 Aim of the thesis

The main body of this research work has been focused on the development of materials containing lignin as a main component. From the literature examples reported in the previous paragraph, lignin was employed in addition to other principal macromolecules in order to modify their properties, to confer determined characteristics or to improve some features of determined blends/ mixtures/ copolymers, etc. For this reason, the aim of this research was then the realization of materials in which lignin figured as the major constituent; three functionalizations have been carried out to obtain:

- Lignin-based polyesters to be applied as primer coatings for different substrates, due to their high adhesion strength.

- Silanized lignin-based materials to protect different metallic substrates like aluminum and steel from corrosion, due to their elevated corrosion resistance and adhesion strength.

- Lignin-based crosslinked matrixes for composite materials, in an effort to suggest new solutions for realization of industrial matrixes for fiber-reiforced composite materials.

References

1. **Smith, C. and Rees, G.** *Economic Development.* Basingstoke : Macmillan Business, 1998.

2. **Blewitt, J.** *Understanding Sustainable Development. Second edition.* New York : Routledge, 2015.

3. **L. R. Kahle, E. G.Atay, Eds.** *Communicating Sustainability for the Green Economy.* New York : M.E. Sharpe, 2014.

4. **Mann, S.** Visualising Sustainability. *Computing for Sustainability.* [Online] March 15, 2009. [Cited: November 24, 2016.] https://computingforsustainability.com/2009/03/15/visualising-sustainability/.

5. **Field, V.R. Barros, D.J. Dokken, K.J. Mach, M.D. Mastrandrea, T.E. Bilir, M. Chatterjee, K.L. Ebi, Y.O. Estrada, R.C. Genova, B. Girma, E.S. Kissel, A.N. Levy, S. MacCracken, P.R. Mastrandrea, and L.L. White (eds.).** *Climate change 2014:Impacts, Adaptations and Vulnerability.* Cambridge, United Kingdom and New York, NY, USA : Cambridge University Press, 2014.

6. Sustainable development. *Wikipedia.* [Online] [Cited: November 24, 2016.] https://en.wikipedia.org/wiki/Sustainable_development.

7. **Magee, Scerri, James, Thom, Padgham, Hickmott, Cahill.** Reframing social sustainability reporting: towards an engaged approach. *Environment, Development and Sustainability.* 2012, Vol. 15, 225-243.

8. **Kamm, B. Kamm . M.** Principles of biorefineries. *Applied Microbiology and Biotechnology.* 2004, Vol. 64, pp. 137–145.

9. **Walsh, P.** *Co-production of Food, Feed,Chemicals, Materials, Fuels, Power and Heat from Biomass***.** Copenhagen : IEA Bioenergy, 2007. Minutes of the third Task meeting.

10. **Cherubini, F.** The biorefinery concept: Using biomass instead of oil for producing energy. *Energy Conversion and Management.* 2010, Vol. 51, pp. 1412–1421.

11. **Vertès, Hodge, Qureshi.** *Biorefineries Integrated Biochemical Processes for liquid biofuels.* s.l. : Elsevier, 2014.

12. **V. B. Agbor, N. Cicek , R. Sparling , A. Berlin , D. B. Levin.** Biomass pretreatment: Fundamentals toward application. *Biotechnology Advances.* 2011, Vol. 29, pp. 675–685.

13. **Kobayashi, Hirokazu and Fukuoka, Atsushi.** Synthesis and utilisation of sugar compounds derived from lignocellulosic biomass. *Green Chemistry.* 2013, Vol. 15, pp. 1740-1763.

14. **S. Laurichesse, L. Avérous.** Chemical modification of lignins: Towards biobased polymers. *Progress in Polymer Science.* 2014, pp. 1266–1290.

15. **G. Pilate, A. Dejardin, J.C. Leple.** Field Trials with Lignin- Modified Transgenic Trees. [book auth.] Jouanin and Lapierre. *Advances in Botanical Research.* s.l. : Elsevier, 2012, pp. 1-36.

16. **S. Laurichesse, L. Avérous.** Chemical modification of lignins: Towards biobased polymers. *Elsevier.* 2013, Vol. 39, pp. 1266–1290.

17. **Ralph J, Lundquist K, Brunow G, Lu F, Kim H, Schatz PF, Marita JM, Hatfield RD, Ralph SA, Christensen JH, et al.** Lignins: natural polymers from oxidative coupling of 4-hydroxyphenylpropanoids. *Phytochemistry Reviews.* 2004, pp. 29-60.

18. **Argyropoulos DS, Jurasek L, Krištofová L, Xia Z, Sun Y, Paluš E.** *Abundance and reactivity of dibenzodioxocins in softwood lignin***.** 658-666, 2002, Journal of Agricultural and Food Chemistry.

19. **Reale S, Di Tullio A, Spreti N, De Angelis F.** *Mass spectrometry in the biosynthetic and structural investigation of lignins* .2004, Mass Spectrometry Reviews, pp. 87-126.

20. **R. Vanholme, B. Demedts, K. Morreel, J.Ralph and W. Boerjan.** *Lignin Biosynthesis and Structure.*2010, American Society of Plant Biologists, pp. 895-905.

21. **K.K.Pandey.** *A study of chemical structure of soft and hardwood and wood polymers by FTIR spectroscopy.* 1999, The journal of applied polymer science, pp. 1969–1975.

22. **C.L. Chen, D. Robert.** Characterization of lignin by 1H and 13C NMR spectroscopy. *Methods in enzymology.* 2004.

23. **Hatcher, J.L. Fadon and Patrick G.** Is There Any Order in the Structure of Lignin? *Energy Fuels.* 1994, pp. 402-407 .

24. **G, Brunow.** Methods To Reveal The Structure Of Lignin. *Biopolymers Online.* 2001, p. 106.

25. **O. Faruk, M. Sain.** *Lignin in polymer composites.* s.l. : Elsevier, 2016.

26. The chemical reactions in Kraft pulping process. *pulp paper mill.* [Online] 2015. http://www.pulppapermill.com/the-chemical-reactions-in-kraft-pulping-process/.

27. **A. Agrawal, N. Kaushik, S. Biswas.** Derivatives and Applications of Lignin – An Insight. *The scitech journal.* 2014.

28. [Online] http://www.ieabioenergy.com/wp-content/uploads/2013/10/Task-42-Biobased-Chemicals-value-added-products-from-biorefineries.pdf .

29. **J. Zhang, Y. Chen, P. Sewell and M. A. Brook.** *Utilization of softwood lignin as both crosslinker and reinforcing agent in silicone elastomers.*2015, Royal Society of Chemistry.

30. **C. Jiang, H.He, X. Yao, P. Yu, L. Zhou, D. Jia.** *In situ dispersion and compatibilization of lignin/epoxidized natural rubber composites: reactivity, morphology and property.* 2015, Journal of applied polymer science.

31. **S. L. Hilburg, A.N. Elder, H. Chung, R. L. Ferebee.** A universal route towards thermoplastic lignin composites with improved mechanical properties. *Polymer.* 4, 2014, Vol. 55.

32. **G.Griffini, V. Passoni, R. Suriano, M. Levi, and S. Turri.** *Polyurethane Coatings Based on Chemically Unmodified Fractionated Lignin.* 2015, ACS Sustainable Chemistry & Engineering, Vol. 3,p. 1145−1154.

33. **C.A. Cateto, M. F. Barreiro, C.Otti, M. Lopretti, A. E. Rodrigues and M. N. Belgacem.** *Lignin-based rigid polyurethane foams with improved biodegradation.* 2014, journal of cellular plastics.

34. **Chen, Zhiyuan Peng & Fangeng.** *Synthesis and Properties of Lignin-Based Polyurethane Hydrogels.*2011, International Journal of Polymeric Materials and Polymeric Biomaterials.

35. **Y. Nonaka, B. Tomita, and Y. Hatano.** Progress in development of epoxy resin systems based on wood biomass in Japan. *Wood industries.* 1996.

36. **S. Tai, M. Nagata, J. Nakano, and N. Migita.** Studies on utilization of lignin. *Mokuzai Gakkaishi.* 1967, Vol. 13.

37. **Scarica, C.** , Lignin as a renewable material for industrial applications, Ph.D. Thesis in Material Engineering, Politecnico di Milano, year 2014-2015.

38. **C. Vilela, A. F. Sousa, A. C. Fonseca, A. C. Serra, J. F. J. Coelho, C. S. R. Freire and A. J. D. Silvestre.** The quest for sustainable polyesters – insights into the future. *Royal society of chemistry.* 2014.

39. **Wool, Wim Thielemans and Richard P.** *Lignin Esters for Use in Unsaturated Thermosets: Lignin Modification and Solubility Modeling.*2005, Biomacromolecules, pp. 1895-1905.

40. **S. C. Fox, and A. G. McDonald.** Chemical and thermal characterization of three industrial lignins and their corresponding lignin esters. *Bioresources.* 2010, pp. 990-1009.

41. **G. Sivasankarapillai, A. G. McDonald.** *Synthesis and properties of lignin-highly branched poly (ester-amine) polymeric systems.*2011, biomass and bioenergy , pp. 919-931.

42. **Chen, Cai, Frihart, Lorenz, Ibach.** *Chemical modification of kraft lignin: effect on chemical and thermal properties.*2014, bioresources.

43. **A. García, A. Toledano, M. Á. Andrés, J. Labidi.** Study of the antioxidant capacity of Miscanthus sinensis lignins. *Process biochemistry.* 2010, Vol. 45, pp. 935–940.

44. **M. H. Hussin, A.A. Rahim, M. N. M. Ibrahim,N. Brosse.** The capability of ultrafiltrated alkaline and organosolv oil palm (Elaeis guineensis) fronds lignin as green corrosion inhibitor for mild steel in 0.5 M HCl solution. *Measurement.* 2016, Vol. 78, pp. 90–103.

45. **M.Yu. Vagin, S. A. Trashin, A. A. Karyakin.** Corrosion protection of steel by electropolymerized lignins. *Electrochemistry Communications.* 2005, Vol. 8, pp. 60–64.

46. **Pan, Tongyan.** A first-principles based chemophysical environment for studying lignins as an asphalt antioxidant. *Construction and Building Materials.* 2012, pp. 654–664.

47. **M.A. Abu-Dalo, N. A.F. Al-Rawashdeh, A. Ababneh.** Evaluating the performance of sulfonated Kraft lignin agent as corrosion inhibitor for iron-based materials in water distribution systems. *Desalination.* 2013, Vol. 313, pp. 105–114.

48. **Yin, Yang,Sun, Di.** *Preparation and properties of lignin-epoxy resin composite.*2012, bioresources,Vol. 7, pp. 5737-5748.

49. **M. Canetti, F.Bertini.** Supermolecular structure and thermal properties of poly(ethylene terephthalate)/lignin composites. *Composites science and technology .* 2007, Vol. 67,pp. 3151–3157.

50. **F.Siahmed, A. Lounis and L. Faghi.** *Elaboration, characterization, and degradation of composite material: Lignocellulosic/unsaturated polyester.*2012, Journal of Composite Materials,Vol.11, pp. 2965–2972.

2 MATERIALS AND METHODS

2.1 Lignin Polyesters

2.1.1 Raw materials

The starting materials for the realization of the primary products consisted of a specific type of lignin and of a versatile solvent:

- INDULIN® AT: is a pine kraft lignin supplied by MeadWestvaco (USA). It appears as a dark brown fine powder, as it is possible to see below in **Figure 14**.

Figure 14 Image of Indulin AT powder

- Tetrahydrofuran (THF): it's a colorless and water soluble solvent, belonging to the family of the heterocyclic compounds (**Figure 15**). It has a density of 0.889 g/mL at 25 °C and a boiling point of 65-67 °C. It was supplied by Sigma-Aldrich, with a purity up to 99.9%.

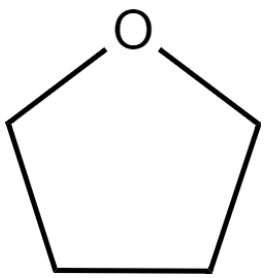

Figure 15 schematic representation of THF (51)

2.1.2 Soluble Lignin Fraction (SLF)

Soluble Lignin Fraction was obtained through a process of fractionation of the Indulin AT: 4 grams of lignin were dissolved in 150 mL of THF, and maintained for three days under magnetic stirring in a round-bottom flask. Under these conditions, the soluble part of the lignin was able to dissolve in the solvent. After three days, the two parts were separated by a filter Whatman 1001-125, the soluble part was recovered and separated from the solvent by means of a rotary evaporator IKA . The fractionation yield was found to be about 60%; to correlate this result with the thermodynamic miscibility of lignin in THF solvent, the Flory-Huggins polymer-solvent interaction parameter χ_{PS} was calculated according to the Hildebrand approach. According to this theory, the solubility parameter δ_{tot} of a substance can be expressed as the sum of three contributions, namely dispersive (δ_d), polar (δ_p) and hydrogen bonding (δ_h), so that:

Eq. 1

$$\boldsymbol{\delta_{tot}^2 = \delta_d^2 + \delta_p^2 + \delta_h^2}$$

Inserting these terms in the expression of χ_{PS} :

Eq. 2

$$\mathbf{X_{PS} = 0.34 + \frac{v_S\left[(\delta_{dS}-\delta_{dP})^2+(\delta_{pS}-\delta_{pP})^2+(\delta_{HS}-\delta_{HP})^2\right]}{RT}}$$

where v_S is the molar volume of the solvent, R is the gas constant (8.314 J/(mol K)), T is the absolute temperature and the subscripts *P* and *S* stand for polymer and solvent, respectively.

The calculation of the individual contributions to the solubility parameter of the solvent were based on the Hansen approach and the temperature employed in **Equation 2** was the boiling temperature of the solvent. The results of these calculations are presented in **Table 2**. The solubility parameter and the Van der Waals volume of lignin Indulin AT are reported in literature. (37)

	δ_d	δ_p	δ_h	δ_{tot}	V_m	X_{PS}
	$[(J/cm^3)^{1/2}]$	$[(J/cm^3)^{1/2}]$	$[(J/cm^3)^{1/2}]$	$[(J/cm^3)^{1/2}]$	$[cm^3/mol]$	
Ind	16,7	13,7	11,7	24,6	2869,2	
THF	16,8	5,7	8	19,4	81,7	0,79
DMSO	18,4	16,4	10,2	26,7	71,3	0,7

Table 2 Hansen solubility parameter δtot (with dispersive δd, polar δp, and hydrogen bonding δh components) and molar volume Vm for the lignin and the solvent employed in this work. (37)

The different contributions (dispersive δ_d, polar δ_p, and hydrogen bonding δ_h) to the solubility parameter of lignin showed relatively similar values, reflecting the fact that they all affect in a comparable way the total solubility parameter of lignin (δ_{tot} = 24.6 $(J/cm^3)^{0.5}$). This behavior may be ascribable to the complex chemical nature of lignin in which aromatic, aliphatic, carbonyl and hydroxyl groups can all give rise to different intermolecular interactions of comparable size. The ability to form such intermolecular interactions has affects the solubility of lignin in a given solvent. To evaluate this effect, the Flory-Huggins interaction parameter for the lignin/dimethyl sulfoxide couple was calculated. Because dimethyl sulfoxide is normally found to be the best solvent for kraft lignin (solubility > 99% at room temperature), the χ_{PS} value obtained for the lignin/dimethyl sulfoxide (χPS = 0.70) system may act as reference as it theoretically represents the maximum allowable value to achieve complete dissolution of lignin, in accordance with the Flory-Huggins theory. Positive deviations from this value lead to a progressively poorer solubilization of lignin in the given solvent. As shown in **table 2**, tetrahydrofuran was found to exhibit a quite low χ_{PS} (0.79), close to the DMSO one, well correlating with the fractionation yield obtained for this solvent. (37)

2.1.3 Succinic Anhydride Lignin (SAL)

Succinic Anhydride Lignin was obtained starting from SLF by means of an esterification reaction with Succinic Anhydride conducted for three hours at a temperature of 60°C in a three neck round-bottom flask maintained under vigorous stirring. An example of setup of the reaction is visible in **Figure 16** below:

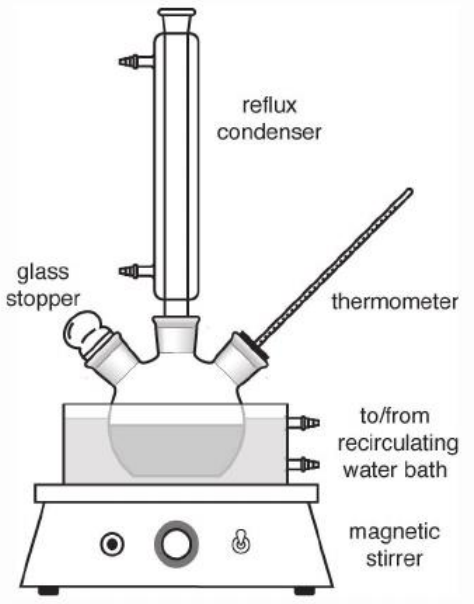

Figure 16 experimental apparatus of the reaction (52)

Under these conditions of temperature and time, five esterification reactions with different weight percentages of Succinic Anhydride with respect to the number of -OH- groups present in Soluble Lignin Fraction ($\%w_{SA}/[OH]_{SLF}$) were executed to find out the best ($\%w/[OH]_{SLF}$) proportion. All of the reactions were realized using 1-methylimidazole as catalyst. The obtained products were separated from the solvent by means of rotary evaporator and dried under vacuum in oven for 24 hours at 50°C. Details of each of the five reactions are visible in **Table 3** below. A representative scheme of reaction between lignin and succinic anhydride is shown in **Figure 17** below:

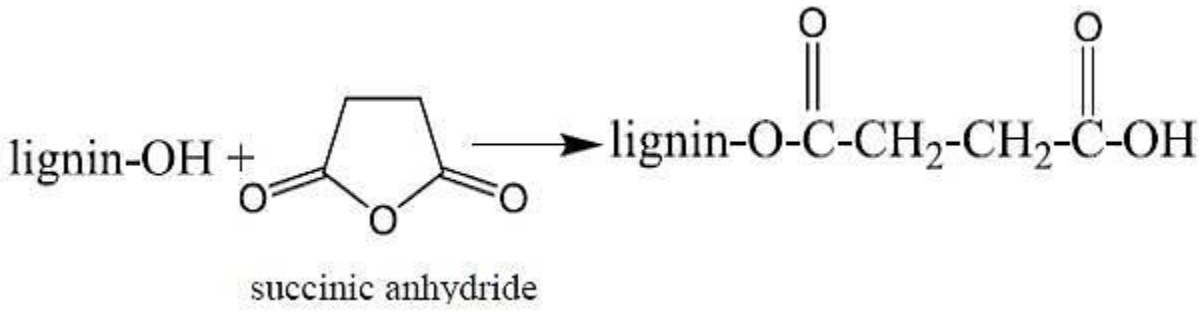

Figure 17 SAL schematic representation of the reaction (37)

SAMPLE NAME	AMOUNT OF SA ($\%w/[OH]_{SLF}$)	SLF (g)	SA (g)	CATALYST (µL)	SOLVENT (mL)	REACTION TIME (h)	TEMPERATURE (°C)
SAL 103	10	1	0,062	50	15	3	60
SAL 203	20	1	0,125	50	15	3	60
SAL 303	30	1	0,187	50	15	3	60
SAL 403	40	1	0,25	50	15	3	60
SAL 503	50	1	0,312	50	15	3	60

Table 3 Details of the stoichiometric ratios and of the amounts of reagents for each of the five reactions

2.1.4 Crosslinked coatings

By means of the production of SLF and SAL, seven different formulations were prepared to obtain seven different coatings. The crosslinking agent used for this experimental part is CYMEL 303,supplied by Cytec Industries; it consists of a commercial grade of hexamethoxymethylmelamine (HMMM) supplied in liquid form at >98% non-volatile. The catalyst instead, is the p- toluenesulfonic acid (PTSA), provided by Sigma-Aldrich.

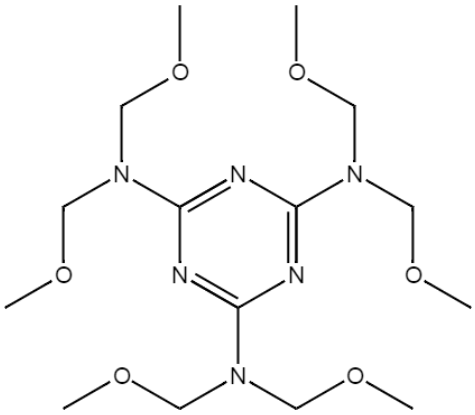

Figure 18 Representation of HMMM structure (53)

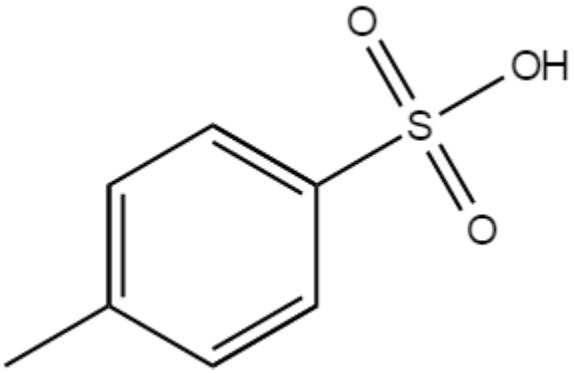

Figure 19 Representation of PTSA (54)

The systems realized differ from each other by the weight ratios of SAL and SLF to the CYMEL; the stoichiometric ratios of each of the formulations are visible in **Table 4** below.

- SAL Self: it is the system 100% made of SAL, concentrated at 20%w/v in solution with the THF solvent, with the addition of PTSA (1% w/w with respect to lignin) to catalyze the self-crosslinking reaction.

- SAL-CYM 97-3: system made with the addition of 3%w/w of CYMEL with respect to the SAL, in solution with the THF solvent.

- SAL-CYM 95-5: system made with the addition of 5%w/w of CYMEL with respect to the SAL, in solution with the THF solvent.

- SAL-CYM 93-7: system made with the addition of 7%w/w of CYMEL with respect to the SAL, in solution with the THF solvent.

- SLF-CYM 97-3: system made with the addition of 3%w/w of CYMEL with respect to the SLF, in solution with the THF solvent.

- SLF-CYM 95-5: system made with the addition of 5%w/w of CYMEL with respect to the SLF, in solution with the THF solvent.

- SLF-CYM 93-7: system made with the addition of 7%w/w of CYMEL with respect to the SLF, in solution with the THF solvent.

SAMPLE	THF (mL)	SAL (g)	SLF (µL)	CYMEL (g)	PTSA (mg)
SAL Self	4	0,8	/	/	8
SAL-CYM 97-3	4	0,776	/	0,024	8
SAL-CYM 95-5	4	0,76	/	0,04	8
SAL-CYM 93-7	4	0,744	/	0,056	8
SLF-CYM 97-3	4	/	0,776	0,024	8
SLF-CYM 95-5	4	/	0,76	0,04	8
SLF-CYM 93-7	4	/	0,744	0,056	8

Table 4 stoichiometric ratios and amounts of reagents for the seven lignin-based polyesters formulations

All these systems, after having been deposited by means of the spin coating technique on different substrates, were subjected to a thermal treatment at 200°C for 30 minutes to allow the crosslinking reaction to happen.

2.2 Silanized lignin-based coatings

2.2.1 Raw Materials

The starting materials to obtain the silanized lignin were:

- Soluble Lignin Fraction (SLF)
- Tetrahydrofuran (THF)
- 3-Isocyanatopropyltrimethoxysilane (IPTMS): it is a silane with a molecular weight of 205,28 g/mol and a density of 1g/cm^{3}at 25°C. Supplied by Wacker Silicones.

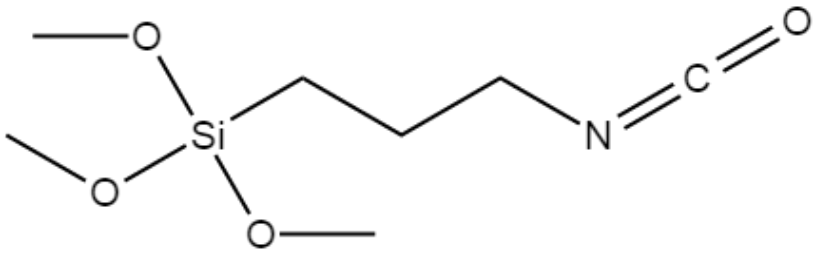

Figure 20 Schematic structure of IPTMS

- Dibutyltin dilaurate (DBTDL): catalyst with a density of 1.066 g/mL at 25 °C and a molecular weight of 631,56 g/mol. Supplied by Sigma-Aldrich.

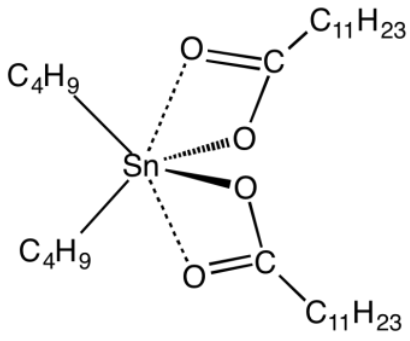

Figure 21 Schematic structure of DBTDL

2.2.2 Silanized Lignin (LKSi)

LKSi was obtained through a chemical reaction between OH groups of Soluble Lignin Fraction (SLF) and the NCO groups of IPTMS, catalyzed by DBTDL. According to Griffini et al.(2015), to evaluate the reactivity of the lignin toward NCO groups, it was necessary to determine its hydroxyl content by means of quantitative ^{13}C- NMR spectroscopy executed on lignin after acetylation. The determination of the hydroxyl (aliphatic and phenolic) content was done through the calculation of the number of carbon atoms associated with OH groups (aliphatic or aromatic) per aryl unit. Subsequently, the actual molar concentration (mmol/g) of OH groups in lignin was obtained on the basis of the molecular weight of the phenyl propanic unit, the latter assumed to be 184 g/mol for kraft lignin. (55)

From these considerations (55) , it was possible to calculate the amount of IPTMS for 1 gram of SLF to use in the reaction:

Eq. 3 $$mmol_{-reactive\ OH} = mmol_{NCO} = mmol_{IPTMS} = 1.05 = 1000\frac{g_{IPTMS}}{MW_{IPTMS}}$$

Eq. 4 $$g_{IPTMS} = \frac{1.05}{1000} MW_{IPTMS} = 0.2153\ g$$

In a three neck round-bottom flask 3.2g of Soluble Lignin Fraction (SLF) were reacted with 3.2* 0.2153=0.6889 g of IPTMS, in 64 mL of THF. The reaction was maintained at 60°C in an oil bath heated by means of a hot plate, under an inert atmosphere obtained through the insufflation of N_2 in the flask. Below in **Figure 22** it is possible to take a look at the reaction apparatus.

Figure 22 Setup of the silanization reaction

After the insertion of the catalyst, the reaction was monitored at three different times (t0, t2, t4) through FTIR analysis: the disappearance after about four hours of the NCO peak at 2270 cm^{-1} in **figure 23** indicated the absence of NCO groups in the system, so that the reaction took place.

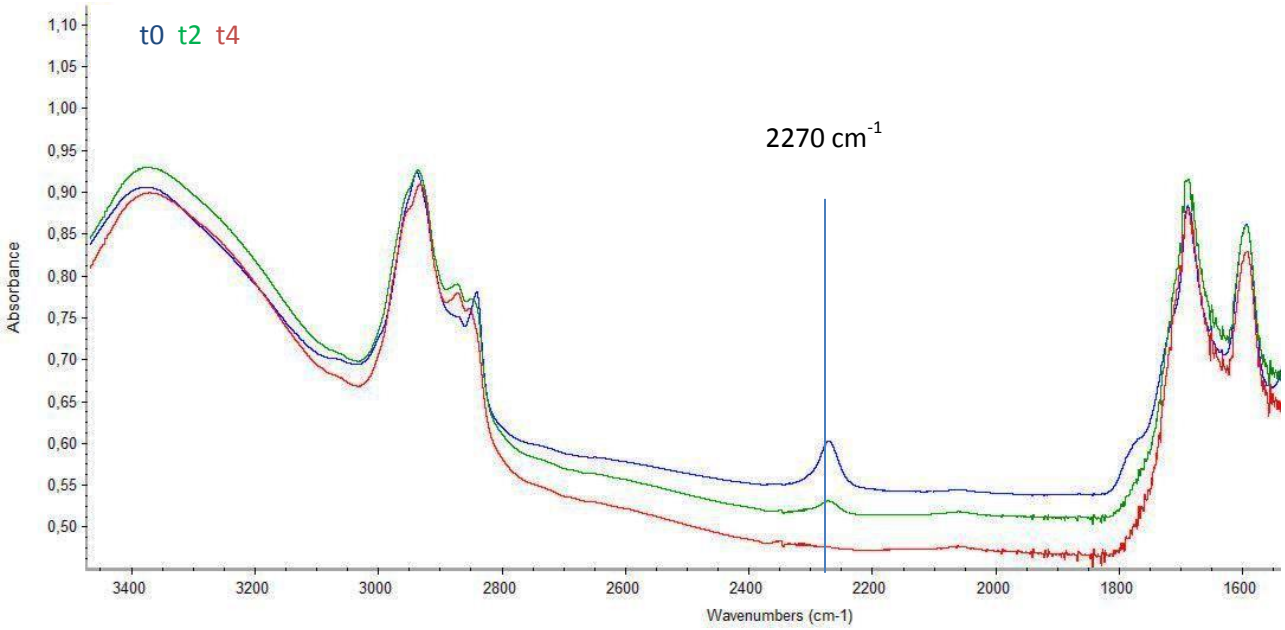

Figure 23 FTIR spectra of the silanization reaction at different times.

2.2.3 Silanized Lignin Coatings

Four different types of coatings were prepared, and the stoichiometric ratios of each of the formulations are visible in **Table 5** below.

- LKSi: realized with the LKSi dissolved in THF solvent at two different concentrations, 20% and 0,5%, with the addition of Acetic Acid (99% pure) in order to obtain a solution with a pH around 3-4. Deposition occurred by means of a spin coater, at 1000 rpm for 80 seconds.

- LKSi- TEOS: made with TEOS (Tetraethyl orthosilicate, MW=208.33 g/mol; density= 0.933 g/mL) in a ratio of 5% with respect to the LKSi, at two different concentrations with respect to the THF solvent (20%, 0,5%). 3% of distilled water with respect to the solvent was also added, together with Acetic Acid in order to obtain a solution with a pH around 3-4.

- [LKSi]+ GLYCEROL: realized with the Silanized Lignin dissolved in THF solvent at two different concentrations, 20% and 0,5%, with the addition of Glycerol (1.25 g/mL, supplied by Sigma-Aldrich) in a ratio of 10% with respect to the LKSi and of Acetic Acid in order to obtain a solution with a pH around 3-4.

- [LKSi-TEOS]+ GLYCEROL: made with TEOS in a ratio of 5% with respect to the LKSi, at two different concentrations with respect to the THF solvent (20%, 0,5%). 3% of distilled water with respect to the solvent was also added, together with Glycerol in a ratio of 10% with respect to the LKSi and Acetic Acid in order to obtain a solution with a pH around 3-4.

SAMPLE	THF (mL)	LKSi (g)	TEOS (µL)	WATER (µL)	GLYCEROL (µL)	ACETIC ACID (mL)
[LKSi]20%	4	0,8	/	/	/	1
LKSi]0,5%	4	0,02	/	/	/	0,75
[LKSi-TEOS]20%	4	0,76	42,8	120	/	1
[LKSi-TEOS]0,5%	4	0,019	1,07	120	/	0,75
[LKSi]20%+GLY10%	4	0,8	/	/	64	1
[LKSi]0,5%+GLY10%	4	0,02	/	/	1,6	0,75
[LKSi-TEOS]20%+ GLY10%	4	0,76	42,8	120	64	1
[LKSi-TEOS]0,5%+ GLY10%	4	0,019	1,07	120	1,6	0,75

Table 5 stoichiometric ratios of the four silanized lignin-based formulations

Deposition of all the solutions occurred by means of a spin coater, at 1000 rpm for 80 seconds. The solutions deposited on different substrates were then subjected to a thermal treatment of 200°C for 15 minutes.

2.2 Lignin-based crosslinked matrices for composite materials

2.2.1 Raw Materials

In order to realize the two systems that will further be described, the following materials have been used:

- Indulin® AT, described in the previous paragraphs;
- Acronal®, supplied by BASF, water-based acrylic dispersion used as binder in high quality architectural coatings, adhesives, construction and fiber bonding applications;
- Saduren 163®, provided by BASF, binder for nonwovens made from mineral fibers core active crosslinking agent for polymer dispersions; it is an aqueous solution of a melamine-formaldehyde resin etherified with methanol;
- Primid QM 1260®: it is an improved hydroxyalkylamide crosslinker for the formulation of exterior durable powder coatings. Supplied by EMS-Griltech;
- P- toluenesulfonic acid (PTSA), catalyst supplied by Sigma-Aldrich.
- Carbon fibers, non woven with an areal weight of 20 g/m^2, supplied by PRF Composite Materials.

Two composite systems were realized and compared:

- A standard one, based on a matrix made of Saduren/Acronal [30%/70%] solution in different concentrations in the solvent, which consisted of distilled water; the samples were thermally treated in oven at 210°C for about 10 minutes, in order to achieve the crosslinking reaction of the matrix.

- An experimental one, based on a matrix made of Indulin AT dissolved in distilled water with the addition of the Primid crosslinker in a ratio of 10% to the lignin, and of the PTSA catalyst 1% with respect to the dry content. Being lignin insoluble in neutral water (pH7), it was necessary to increase the pH of the solution by means of Ammonium Hydroxide. Also This system was realized at different concentrations of solute in water solvent, in order to increase progressively the add-on of dry content of matrix in the composite material. The samples were

thermally treated in oven at 200°C for about 30 minutes, in order to achieve the crosslinking reaction of the matrix.

Both these systems were obtained by fibers impregnation inside bechers containing the two solutions. After the immersion, the impregnated carbon fibers were pressed inside rollers for the same number of times. Below in **Figure 24** an example of carbon fibers rollers is visible.

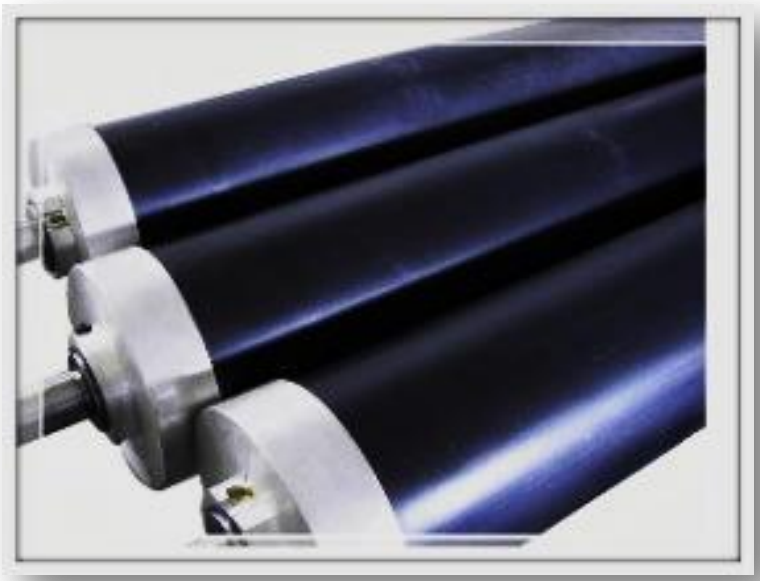

Figure 24 carbon fibers rollers

2.2.1 Composite Systems

In **Table 6** below it is possible to see the two systems compared according to the effective add-on of matrix with respect to the fibers.

SAMPLE NAME	CARBON FIBERS AREA [cm^2]	EFFECTIVE ADD-ON	SAMPLE NAME	CARBON FIBERS AREA [cm^2]	EFFECTIVE ADD-ON
Sad-Acr [10%]	12	20%	Ind-Pr [10%]	12	20%
Sad-Acr [20%]	12	30%			
Sad-Acr [30%]	12	50%	Ind-Pr [20%]	12	50%
Sad-Acr [40%]	12	70%			
Sad-Acr [60%]	12	100%	Ind-Pr [40%]	12	100%

Table 6 Comparison of the two composite systems realized

2.3 Characterization Techniques

2.3.1 Differential Scanning Calorimetry (DSC)

It is a technique in which the monitoring parameters are the difference in heat flow rate (or power) and the time while the samples are exposed to a temperature programme. The instrument is a *differential scanning calorimeter* and may work in two ways, as a *heat-flux DSC* or *power compensation DSC,* depending on which method of measurement is used. *In a heat-flux DSC* instrument, the temperature difference between sample and reference is recorded, after properly calorimetric calibration, as a direct measure of the difference in heat flow rate or the difference in power. In a *power compensation DSC* instrument instead is measured the difference in power supplied to the sample and to the reference, necessary to maintain their temperatures as nearly the same as possible. The power difference in units of watts (ΔP) should be plotted as ordinate. Since a positive input of power into the sample is demanded in endothermic reactions, the DSC convention requires the endothermic peaks to be plotted upwards, and t or T to increasing from left to right. (56)

2.4.1.1 Theory of DSC

The shape and the size of a typical DSC curve are determined not only by the environment surrounding the sample and reference materials but also by the mechanism controlling the transition and the sample material characteristics. **Figure 25** shows a theoretical DSC curve for a material which melts, and the other one usually obtained in practical situations. During a melting process, the reaction should exactly end at the peak when all the material has already melted and when the reaction that has produced the heat has ceased, so that the curve should then return abruptly to the baseline as in curve b. More often the curve obtained resembles that of curve a with a relatively slow return to the baseline. (56)

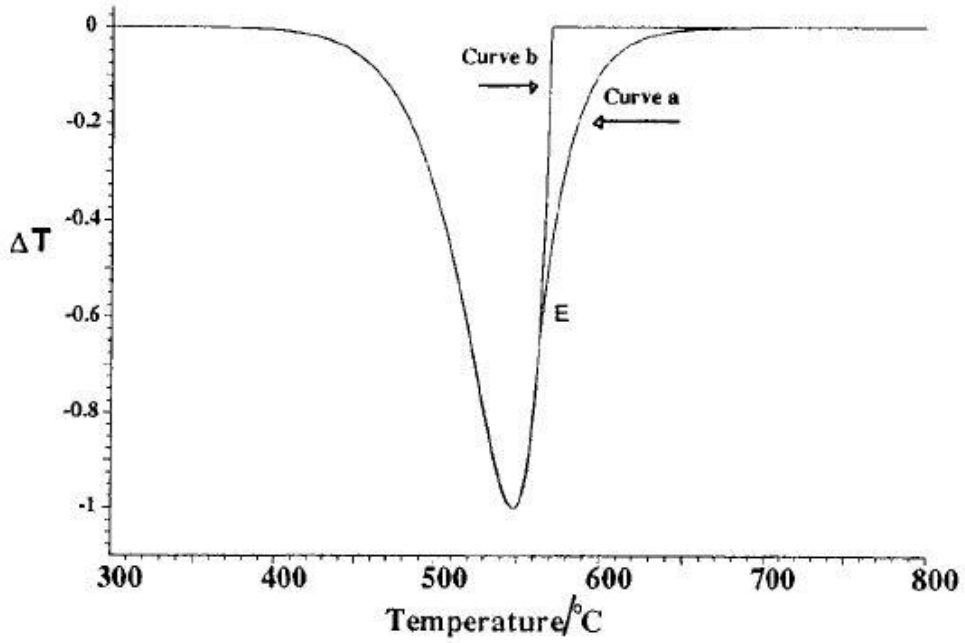

Figure 25 Examples of practical (a) and theoretical (b) DSC curves (56)

Theory of DSC is usually based on heat transfer equations such as the thermal analogue of Ohm's Law to simulate heat flow into the test materials:

Eq. 5 $$d\,q\,/\,d\,t = (\,T_F - Ts)\,/R_{SF}$$

Here $d\,q\,/\,d\,t$ is the heat flow in J s^{-1} between points F and S which have temperatures T_F and Ts , and between which the thermal resistance is R_{SF} K s J^{-1}. The integration of this equation contains a time constant: it means that the temperature Ts does not immediately follow T_F but shows a delay of a time t which depends on R_{SF}. Heat transfer equations of this form were used to develop equations by means of which the heat of reaction involved in a particular DSC peak could be calculated. According to this theory, when a reaction that is producing a peak stops, then the curve of the differential temperature returning to the baseline has an exponential form. This is clearly seen in **Figure 25**. Void defined the 'active area' under the peak as that from the beginning to that point where the curve form is exponential. The point at which this occurs can be determined if a plot of the logarithm of that part of the curve between the peak and its return to the baseline is plotted against time. When the curve is exponential the logarithm plot is linear. Void showed that if the slope of the linear part is A then the heat H absorbed by the reaction is related by:

Eq. 6 H= A. 'active area' (56)

2.4.1.2 Instrumentation of DSC

The parts of the system, visible in **Figure 26**, may be listed as:

- the DSC sensors plus their crucibles and signal amplifier;
- the furnace, its temperature sensor and any cooling and atmosphere facilities;
- the programmer or computer controller;
- the recorder, plotter or data processor.

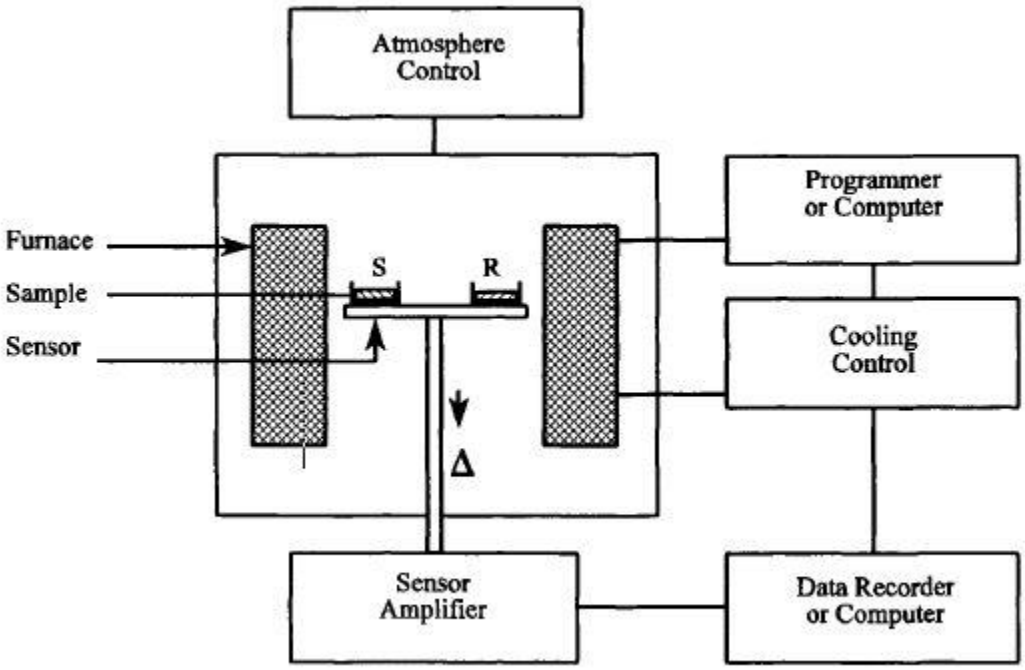

Figure 26 DSC instrumentation scheme (56)

2.4.2 Thermogravimetric analysis (TGA)

“Thermal Analysis (TA) indicates a group of techniques in which a property of the sample is monitored against time or temperature while the temperature of the sample, in a specified atmosphere, is programmed. Among them, TGA represents the measurement of mass as a function of temperature and/or time”. Measurements are used basically to determine the composition of the materials and to give a prediction of their thermal stability. The technique can characterize a variety of materials, all exhibiting weight loss or gain due to sorption/desorption of volatiles, decomposition, oxidation and reduction. The balance operates on a null-balance principle: at the zero, or “null” position equal amounts of light shine on the two photodiodes. If the balance then is moved out of the null position, an unequal amount of light shines on the two photodiodes. Current is then applied to the meter movement to return the balance to the null position. The amount of current applied is taken to be proportional to the weight loss or gain. Below in **Figure 27** has been reported a schematic representation of a TGA instrument. (56)

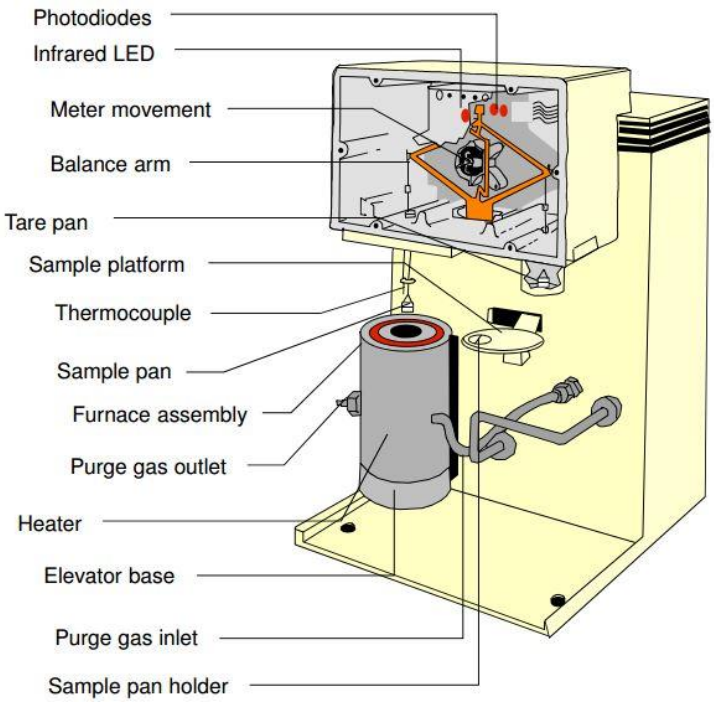

Figure 27 TGA schematic representation (56)

The thermogravimetric curve (TG) visible in **Figure 28** is obtained by plotting mass (mg) or percentage of weight loss in the ordinate versus temperature or time in horizontal axis . The method allows also to obtain the first derivative of the TG curve, called DTG curve, which highlights the start and end of each event of mass loss, indicating the temperature range where a particular decomposition reaction occurs. (57) Below it is possible to see an example of TG curve with its first derivative curve.

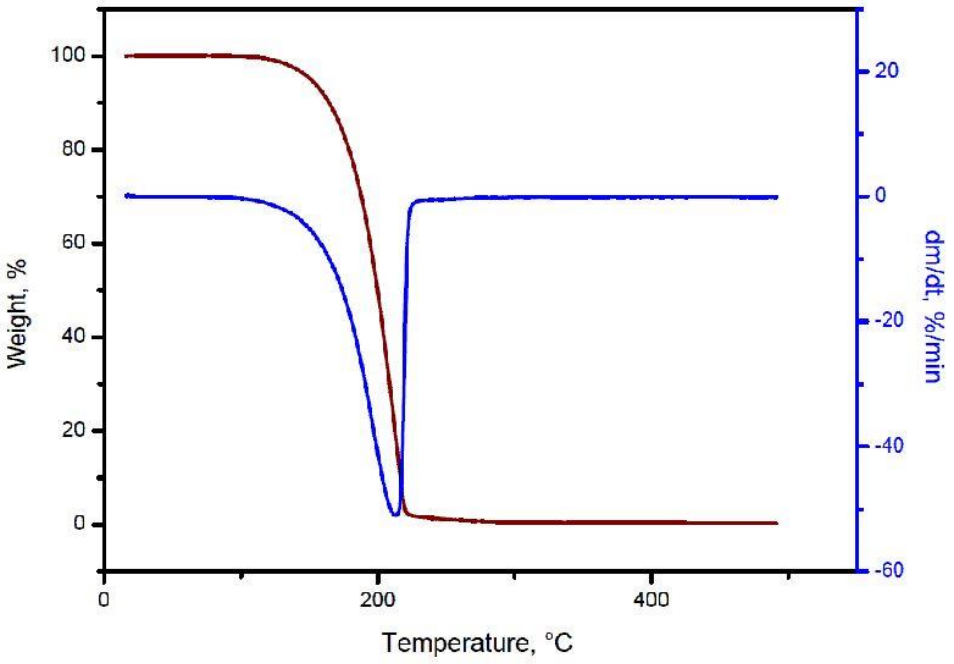

Figure 28 Examples of TG and DTG curves (57)

2.4.3 Contact angle measurement

A drop of water deposited on a solid surface can show either wetting or non wetting effect. Consider a sessile drop on an ideal homogeneous solid surface as shown in **Figure 29**: three different interfaces exist and they are represented by the corresponding surface free energies: γ_{sl} is the solid-liquid interfacial free energy, γ_{sv} is the solid-vapor interfacial free energy, and γ_{lv} is the liquid-vapor interfacial free energy. The liquid is resting on the solid surface at an equilibrium contact angle, θ . Each of the interfaces describes the contact line in a manner so that the corresponding interfacial area is minimized. By looking at the balance of forces along the x-direction, we obtain the following relation: (58)

Eq. 7

$$\sum F_X = \gamma^{sv} - \gamma^{sl} - \gamma^{lv} \cos\theta = 0$$

by re-arranging equation, we can derive the Young's equation as follows:

Eq. 8

$$\gamma^{lv} \cos\theta = \gamma^{sv} - \gamma^{sl}$$

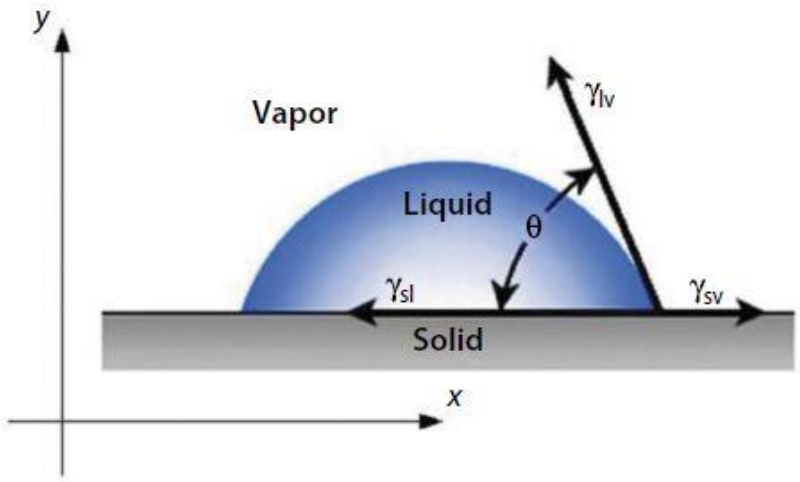

Figure 29 Surface free energies in case of a liquid drop residing on a solid surface (58)

From the point of view of thermodynamic equilibrium, there exist two distinct equilibrium regimes: complete and partial wetting; while complete wetting means that the contact angle between a liquid and a flat solid surface is zero (θe = 0, (c)), and in this case, the liquid forms a very thin film on the solid surface and the long range character of the molecular interactions needs to be taken into account, instead partial wetting occurs if the contact angle is finite (θe > 0 (a) and (b)). The liquid does not spread down to a mesoscopic or a microscopic thickness. Thus, it can be described in terms of macroscopic quantities. Partial wetting, with contact angles greater than 90° (a), are often called "non-wetting" situations when the liquid tends to ball-up and run off the surface easily. (59) The different wetting situations are visible in **Figure 30.**

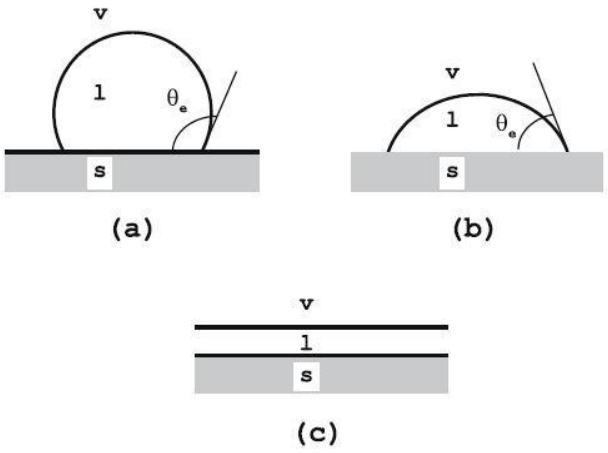

Figure 30 Different wetting situations of a small droplet in contact with a solid surface (59)

In the case of partial wetting, the shape of a liquid drop is determined by a combination of surface tension and gravity effects: the surface forces tend to give drops spherical form, whereas gravity tends to flatten a sessile drop or to elongate them. The shape of the drop is governed by the Laplace equation of capillarity, as follows:

Eq. 9

$$\Delta P = \gamma \left(\frac{1}{R_1} + \frac{1}{R_2} \right)$$

According to this well-known equation, the pressure difference Δ*P* across a liquid–fluid interface is related to its interfacial tension γ and curvature, where *R*1 and *R*2 are the principal radii of curvature. The equilibrium in the boundary region between two bulk phases can be treated mathematically, using either the concept of "surface tension" or the (mathematically) equivalent concept of "surface free energy". This mathematical equivalence allows both terms to be used interchangeably. Frequently, the term "surface tension" or "surface free energy" is used if one of the phases is a gas or a vapour; instead the term "interfacial tension" is used to describe the tension between two immiscible liquids like water and oil. The terms "interfacial tension" or "interfacial free energy" are also used in a more general way to describe the free energy of solid–liquid, solid–vapour, liquid–vapour and liquid–liquid interfaces. The surface tension can be defined as a force per unit length. If the value of this force per unit length is represented by γ, then the work done in extending a movable side a distance d*x* is

Eq. 10

$$\text{Work} = \gamma * l * dx$$

Since l d*x* = d*A,* it gives the change in area and can be equally written as

Eq. 11

$$\text{Work} = \gamma * dA$$

Now, γ represents the work necessary to any reversible process to form a unit area of new surface. It is reported in dyne/cm or mN/m, but also in erg/cm^2 or mJ/m^2 which have the same numerical values. According to the thermodynamics of interfaces, γ_{ij} can be written as the surface excess free energy. That is, γ_{ij} is the change in surface excess free energy produced by a unit increase in area, either of a solid–vapour, solid–liquid, liquid–liquid or liquid–vapour interface, respectively. In general,

Eq. 12 $$\gamma_{ij} = \left(\frac{\partial G}{\partial A_{ij}}\right)_{T,p,n} \quad \text{or} \quad \gamma_{ij} = \left(\frac{\partial F}{\partial A_{ij}}\right)_{T,V,n}$$

where *G* is the Gibbs free energy of the system and *F* the Helmholtz free energy, and A_{ij} the area of the interface between phases *i* and *j*. The subscript "*n*" denotes the assumption of adsorption equilibrium, in the case of multicomponent systems. In the thermodynamics of interface, the Gibbs and the Helmholtz free energy are defined as excess quantities, if an imaginary dividing mathematical surface (Gibbs surface) id designed between the two phases separated by the interface. (59)

The derivation of the Young equation resumes several hypotheses like that the solid surface is smooth, homogeneous, isotropic, insoluble, non-reactive and non-deformable. Then, a unique contact angle is expected for a given solid–liquid system. However, in contact angle experiments, a range of contact angles is usually obtained, and each contact angle gives rise to a mechanically stable liquid meniscus: indeed when liquid is added to a drop on a solid or withdrawn from it, the contact angle is observed to increase or decrease, respectively. The maximum contact angle θ_a is called *advancing*, and the minimum θ_r is called *receding*. The difference between them is called *contact angle hysteresis*.

The equilibrium state that corresponds to the absolute minimum in energy is the stable state; the others are metastable with energy barriers between them. (59)

2.4.3.1 Surface Tension Component Approach

The surface tension component approach was studied by Fowkes. He assumed that the total surface tension can be expressed as the sum of different surface tension components, each of which arises due to a specific type of intermolecular forces. According to Fowkes, in Van der Waals systems, only dispersion forces could effectively operate across the interface. Therefore, he obtained :

Eq. 13 $$\gamma_{sl} = \gamma_{sv} + \gamma_{lv} - 2\sqrt{\gamma_{sv}^{d}\gamma_{lv}^{d}}$$

where γ_{sv}^{d} and γ_{lv}^{d} are the dispersion force components of the solid and liquid surface tension, respectively. Combining previous equation with Young's equation, one obtains:

Eq. 14

$$\cos\theta = -1 + \frac{2\left(\gamma_{sv}^{d}\gamma_{lv}^{d}\right)^{1/2}}{\gamma_{lv}}$$

known as the Girifalco–Good–Fowkes–Young equation. Using this equation, it was possible to evaluate the dispersion components of the solid or liquid surface tension. Owens and Wendt and Kaelble and others stated that the "polar" interaction could be computed using the same geometric mean mixing rule as for the dispersion force interaction. One obtains the following equation:

Eq. 15

$$\gamma_{sl} = \gamma_{sv} + \gamma_{lv} - 2\sqrt{\gamma_{sv}^{d}\gamma_{lv}^{d}} - 2\sqrt{\gamma_{sv}^{p}\gamma_{lv}^{p}}$$

where $\gamma_{sv}^{\ p}$ and $\gamma_{lv}^{\ p}$ are the polar force components of the solid and liquid surface tension. If the contact angles of at least two liquids, usually a polar and a nonpolar liquid, with known $\gamma_{lv}^{\ d}$ and $\gamma_{lv}^{\ p}$ parameters are measured on a solid surface, the $\gamma_{sv}^{\ d}$ and $\gamma_{sv}^{\ p}$ parameters of that solid can be calculated by combining with the Young equation.

2.4.4 Adhesion Measurements

Adhesion is defined as the interatomic and intermolecular interaction that is established at the interface of two surfaces. Any consideration of adhesion mechanisms requires the knowledge of the physical and chemical properties of the adhering surfaces and the delamination surfaces in cases where adhesion has failed in use or as a result of mechanical testing. In literature adhesion is described through its subdivision in three main adhesion mechanisms: mechanical coupling, molecular bonding, and thermodynamic adhesion. The mechanical coupling or interlocking adhesion mechanism is based on the adhesive penetrating into the surface of the substrate. This is similar to having glue on wood, in that the glue penetrating into the rough irregularities on the surface of the wood explains the interlocking concept. Molecular bonding is the most widely accepted mechanism for explaining adhesion between two surfaces in close contact. It involves intermolecular forces between adhesive and substrate such as dipole-dipole interactions, van der Waals forces and chemical interactions like ionic, covalent and metallic bonding. This mechanism describes the strength of the adhesive joints by the presence of interfacial forces and also polar groups. Molecular bonding mechanisms requires a deep contact between the two substrates. However, intimate contact alone is often insufficient for good adhesion at the interface; this could be due to the presence of defects, cracks and air bubbles. The thermodynamic mechanism presents an advantage over the other mechanisms, since it doesn't necessitate of a molecular interaction for good adhesion, only of an equilibrium process at the interface. In neutral environments such as air, for instance, the thermodynamics of the polymer system will attempt to minimize the surface free energy through the orientation of the surface into the non-polar region of the polymer. When the polymer surface is in

contact with a polar substance such as water, good adhesion requires that the interfacial tension be minimized. (60)

Several adhesion measurement techniques exist, able to highlight different surface properties of the materials; in this work, a PosiTest AT-M Manual adhesion PULL-OFF tester visible in **Figure 31** was used to evaluate the adhesion of several coatings on different substrates. In particular, it measures the force required to pull a specified test diameter of coating away from its substrate using hydraulic pressure. Below it is possible to take a look at the sperimental apparatus:

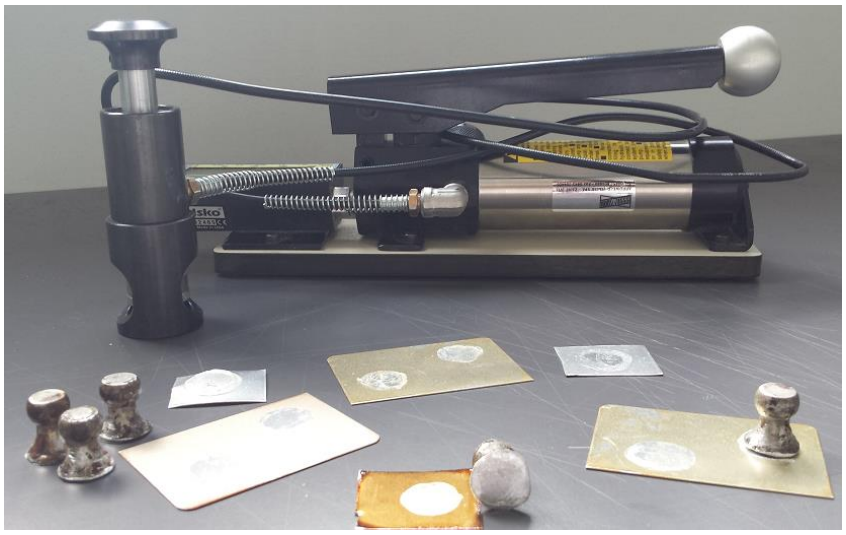

Figure 31 Pull-Off experimental apparatus

2.4.5 Fourier Transform Infrared Spectroscopy (FTIR)

2.4.5.1 Theory of IR

Infrared spectroscopy is a technique based on the vibrations of the atoms of a molecule. An infrared spectrum is usually derived by passing infrared radiation through a sample and determining what fraction of the incident radiation is absorbed at a certain particular energy. The energy at which any peak in an absorption spectrum appears is correlated to the frequency of a vibration of a part of a sample molecule. The visible part of the electromagnetic spectrum is defined as the radiation visible to the human eye. Other detection systems reveal radiation beyond the visible regions of the spectrum and these are classified as radiowave, microwave, infrared, ultraviolet, X-ray and γ-ray. These regions are illustrated in **Figure 32**, together with the processes involved in the interaction of the radiation of these regions with matter. The electromagnetic spectrum and the many interactions between these radiations and the various forms of matter can be considered in terms of either classical or quantum theories. The nature of the various radiations shown in **Figure 32** have been

interpreted by Maxwell' s classical theory of electro- and magneto-dynamics , from which, the term electromagnetic radiation. According to it, radiation is considered as made of two mutually perpendicular electric and magnetic fields, oscillating in single planes at right angles to each other. These fields are in phase and are being propagated as a sine wave, as shown in **figure 33**. The magnitudes of the electric and magnetic vectors are represented by *E* and *B*, respectively. (61)

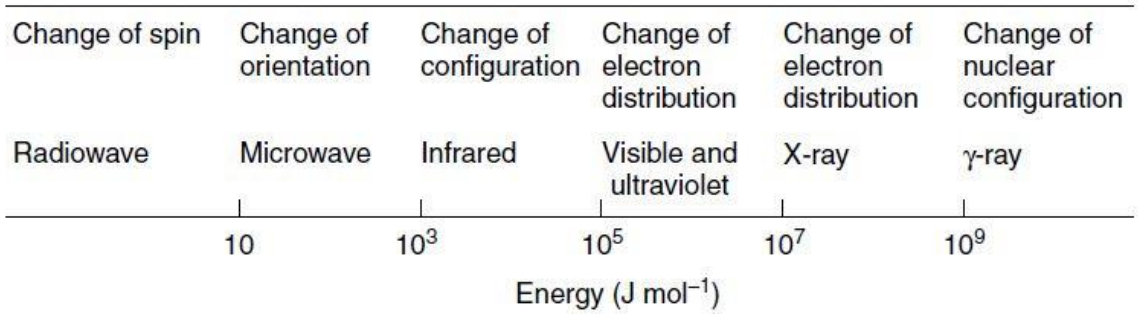

Figure 32 Regions of the electromagnetic spectrum (61)

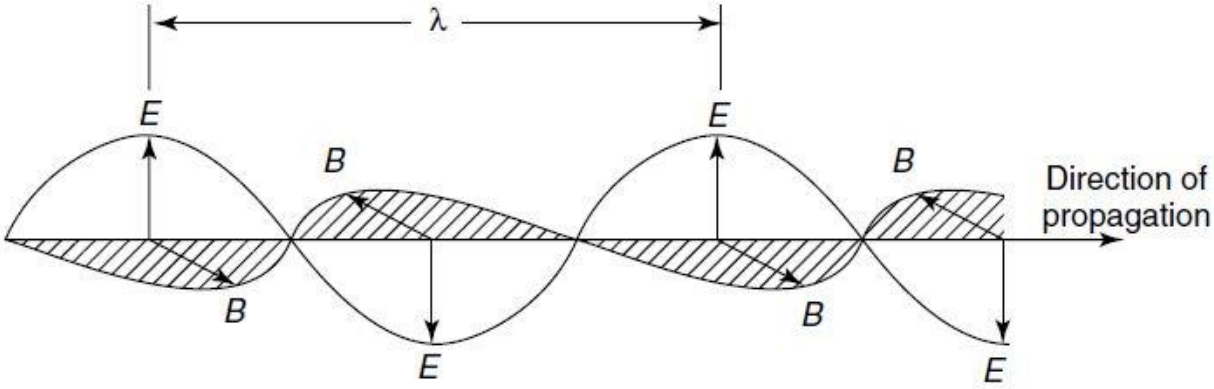

Figure 33 Representation of an electromagnetic wave (61)

A significant discovery made about electromagnetic radiation allowed to determine the velocity of light, *c*, which has the value 2.997 925 × 108 m s^{-1}. If one complete wave travelling a fixed distance each cycle is visualized, it may be observed that the velocity of this wave is the product of the wavelength, λ (the distance between adjacent peaks), and the frequency, ν (the number of cycles per second). Therefore:

Eq. 16 $c = \lambda\nu$

The presentation of spectral regions may be in terms of wavelength as meters or sub-multiples of a meter. Another unit which is widely used in infrared spectroscopy is the wavenumber, ν, in cm^{-1}. This is the number of waves in a length of one centimeter and is given by the following relationship:

Eq. 17 $$\nu = 1/\lambda = \nu/c$$

This unit has the advantage of having a linear behavior with energy. During the 19th Century, a number of experimental observations were made which were not consistent with the classical view that matter could interact with energy in a continuous form. Studies made by Einstein, Planck and Bohr indicated that in many ways electromagnetic radiation could be considered as a stream of particles (or quanta) whose energy, *E*, is given by the Bohr equation, as follows:

Eq. 18 $$E = h\nu$$

where *h* is the Planck constant ($h = 6.626 \times 10^{-34}$ J s) and ν is equivalent to the classical frequency. Processes of change, including changes of vibration and rotation associated with infrared spectroscopy, can be represented in terms of quantized discrete energy levels E_0, E_1, E_2, etc., as shown in **Figure 34**. Each atom or molecule in a system has to exist in one or other of these levels. In a large assembly of molecules, there will be a distribution of all atoms or molecules among these various energy levels. These energy levels are a function of an integer (the quantum number) and a parameter associated with the particular atomic or molecular process associated with that state. Every time a molecule interacts with radiation, a quantum of energy (or photon) is either emitted or absorbed. In each case, the energy of the quantum of radiation must exactly fit the energy gap $E_1 - E_0$ or $E_2 - E_1$, etc. The energy of the quantum is related to the frequency according to **Eq. 18**; hence, the frequency of emission or absorption of radiation for a transition between the energy states E_0 and E_1 is given by:

Eq. 19 $$\nu = (E1 - E0)/h$$

Associated with the uptake of energy of quantized absorption is some deactivation mechanism whereby the atom or molecule returns to its original state. Associated with the loss of energy by emission of a quantum of energy or photon is some prior excitation mechanism. Both of these associated mechanisms are represented by the dotted lines in **Figure 34.**

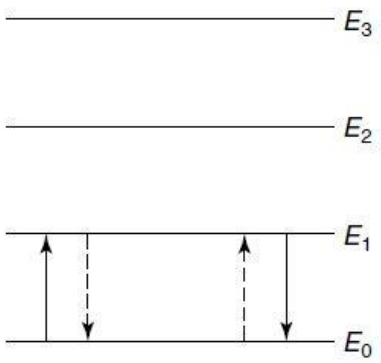

Figure 34 Illustration of quantized discrete energy levels (61)

2.4.5.2 Infrared Absorptions and Normal Modes of Vibration

To be able to show infrared absorptions, a molecule must possesses a specific feature; for example, an electric dipole moment of the molecule must change during the vibration. This is the selection rule for infrared spectroscopy. **Figure 35** shows an example of an infrared-active molecule, a heteronuclear diatomic molecule. The dipole moment of such a molecule changes as the bond expands and contracts. By comparison, an example of an infrared-inactive molecule is a homonuclear diatomic molecule because, since its dipole moment remains zero no matter how long the bond could be. (61)

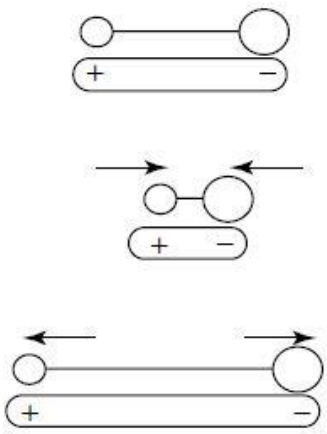

Figure 35 Change in the dipole moment of a heteronuclear diatomic molecule (61)

The interactions between infrared radiation and the matter could be understood in terms of changes in molecular dipoles associated with vibrations and rotations. In order to begin with a basic model, a molecule can be approximately considered as a system of masses joined by bonds with spring-like properties. Taking first the simple case of diatomic molecules, such molecules have three degrees of translational freedom and two degrees of rotational freedom. The atoms in the molecules can also move each one with respect to the other, that is, bond lengths can vary or one atom can move out of its present plane. This is a description of stretching and bending movements that are collectively referred to as vibrations. For a diatomic molecule, only one vibration, corresponding to the stretching and compression of the bond, is possible. This accounts for one degree of vibrational freedom. Polyatomic molecules containing many (*N*) atoms will have 3*N* degrees of freedom. (61)

A molecule can only absorb radiation when the incoming infrared radiation possesses the same frequency as one of the fundamental modes of vibration of the molecule. This means that the vibrational motion of a small part of the molecule is increased while the rest of the molecule is left unaffected. Vibrations can involve either a change in the length of the bond, named stretching, or in the angle of the bond, defined bending. Some bonds can stretch in-phase (symmetrical stretching) or out-of-phase (asymmetric stretching), as shown in **Figure 36**. If a molecule has different terminal

atoms, then the two stretching modes are no longer symmetric and asymmetric vibrations of similar bonds, but will have varying proportions of the stretching motion of each group. In other words, the amount of coupling will vary. (61)

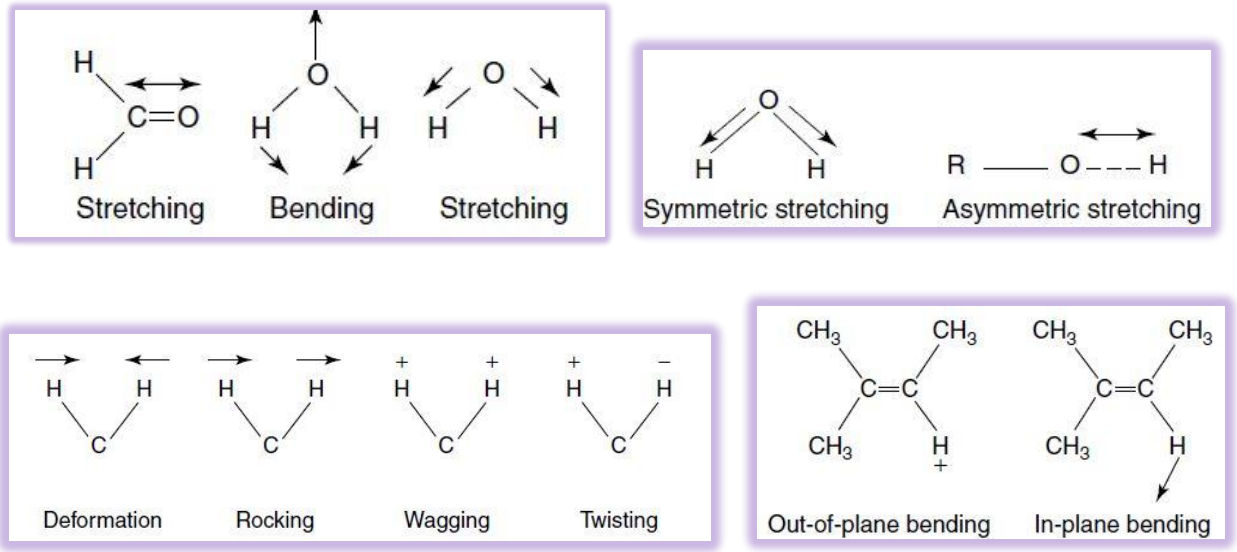

Figure 36 Modes of vibration (61)

2.4.5.3 Fourier-Transform Infrared Spectrometers

Fourier-transform infrared (FTIR) spectroscopy is based on the creation of the interference of radiation between two beams in order to obtain an interferogram. The latter is a signal produced as a function of the change of the length of the path between the two beams. The two distance and frequency domains are interconvertible by the mathematical method of Fourier-transformation. The basic components of an FTIR spectrometer are illustrated schematically in **Figure 37**. The radiation coming from the source is passed through an interferometer to the sample before reaching the detector. Upon amplification of the signal, in which contributions at high-frequency have been cut off by means of a filter, the data are converted to digital form by an analog-to-digital converter and transferred to the computer for Fourier-transformation. The most common interferometer used in FTIR spectrometry is a Michelson interferometer, which is made of two perpendicularly plane mirrors, one of which can travel in a direction perpendicular to the plane. A semi-reflecting film called the beamsplitter, bisects the planes of these two mirrors. The material used to build the beamsplitter has to be chosen according to the region to be examined: materials such as germanium or iron oxide are coated onto an infrared-transparent substrate such as potassium bromide to produce beamsplitters for the mid- or near-infrared regions, while thin organic films, such as polyethylene terephthalate, are used in the far-infrared region. If a collimated beam of monochromatic radiation of wavelength λ (cm) is forced to pass into an ideal beamsplitter, 50% of the incident radiation will be reflected to one of

the mirrors, while the remaining 50% will be transmitted to the other mirror. The two beams are reflected from these mirrors, returning to the beamsplitter where they recombine and interfere. Fifty percent of the beam reflected from the fixed mirror is transmitted through the beamsplitter while the remaining 50% is reflected back towards the source. The beam which comes out of the interferometer at 90° to the input beam is called transmitted beam: it is the beam detected in FTIR spectrometry. The moving mirror produces an optical path difference between the two arms of the interferometer. For path differences of (n + 1/2)λ, the two beams interfere destructively in the case of the transmitted beam and constructively in the case of the reflected beam. (61)

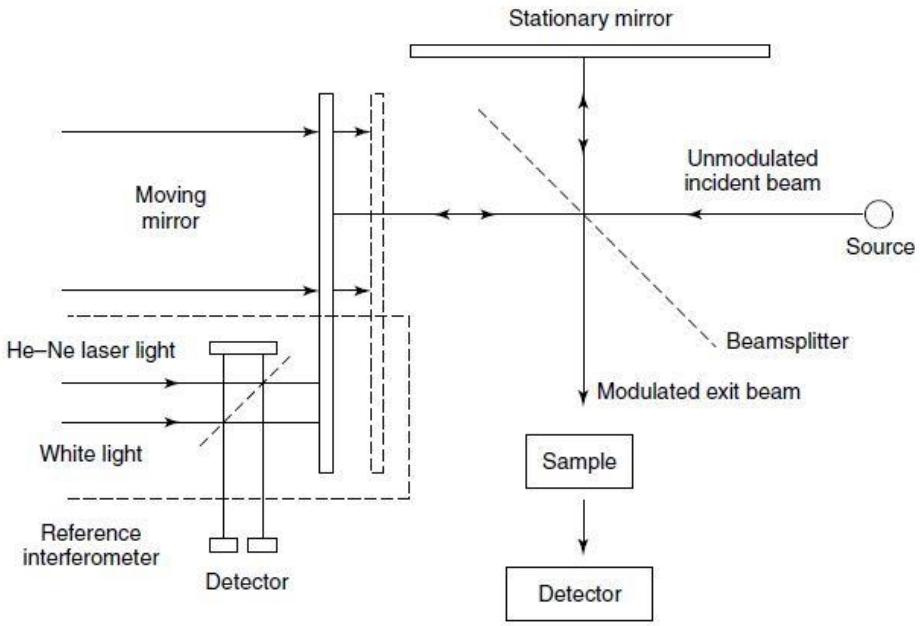

Figure 37 Schematic of a Michelson interferometer (61)

2.4.6 Scanning Electron Microscopy

Scanning electron microscopy (SEM) is a very important technique widely used among the scientific and technological communities. The modern scanning electron microscope can provide imaging details of the order of tens of Angstroms, that is sub nanometers, according to the limits of electron–specimen interactions. Electrons can be provided by many sources and driven by an electrical potential along an evacuated column. Electrons that have been generated in this way are called primary electrons, and they can be formed into a finely focused beam and systematically scanned across a surface of interest. When primary electrons strike the surface of a specimen, a wide range of useful interactions can occur, causing the generation of various charged particles and photons. Electrons that are emitted can be collected and used to form an image, diffraction pattern or chemical

spectrum. In addition, for thin specimens, primary electrons can be transmitted through the material and similarly used. Typical signals are shown schematically in **figure 38**. (62)

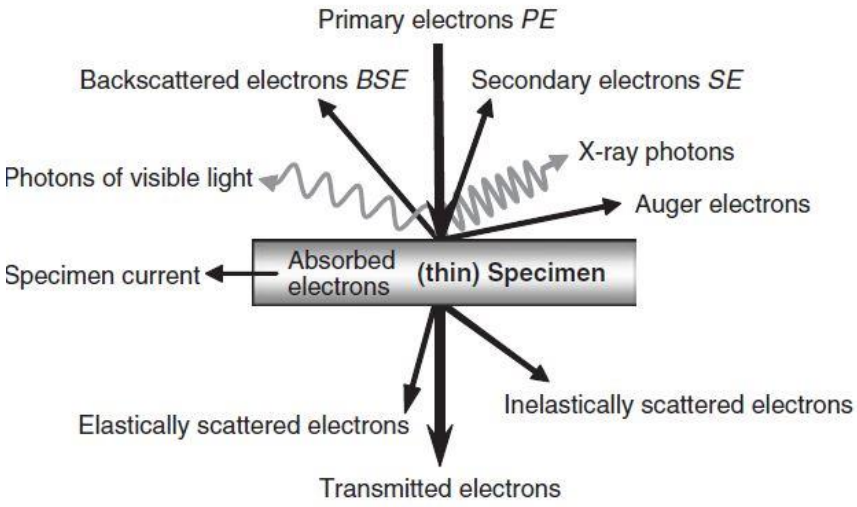

Figure 38 Some of the useful signals that are generated when a focused electron beam strikes a specimen. (62)

In SEM, the principal electron signals that are used are backscattered electrons (BSEs) and also secondary electrons (SEs). These signals are affected as far as it concerns their generation, transport and escape, by differences in specimen composition and surface topography. Images formed in an SEM are the result of variations in electron signal intensity collected at each point (pixel) as the electron beam briefly resides within the scanned area. In addition to the strong interactions of electrons with matter, their mass and charge make it easy to direct them to where we want them, using electromagnetic fields to act as lenses and mirrors, rather like glass lenses and deflectors are used in a light microscope. A simplified schematic diagram of an SEM system is depicted in **figure 39**. The system basically consists of:

- an electron source;
- lenses and apertures;
- coils for rastering (scanning) the beam;
- control electronics and high-voltage supplies;
- a deflector/acquisition system for collecting and processing the signal
- information;
- a monitor to display the information;
- a vacuum system for the source, column and specimen chamber.

The SEM electron source generally operates under a vacuum of 10^{-3} to 10^{-5} Pa (10^{-5}–10^{-7} torr), depending on the type of electron source and the pumping method. There are two good reasons to require a vacuum system:

- the electron source is easily contaminated;
- electrons scatter off anything that gets in the way.

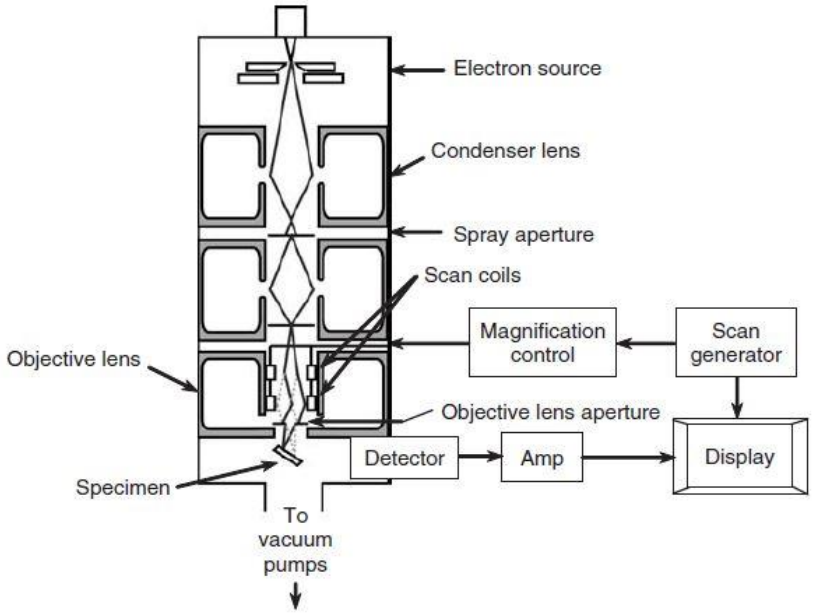

Figure 39 Simplified schematic diagram of the basic components of an SEM. (62)

A high voltage needs to be applied to the filament to produce a beam of electrons. The filament may be a thermionic emitter or a field emission source. The emitted electrons are controlled by an electrode that focuses them into a crossover of diameter $d0$ and convergence semi-angle of $\alpha 0$. The brightness of the source β is a very important parameter; it is given by the current density per unit solid angle (in steradians), written as $A \cdot m^{-2}\ sr^{-1}$ or A/m^2 sr, and is given by:

Eq. 20
$$\beta = {j_b}/{(\pi\alpha^2)} = {4i_b}/{(\pi^2\alpha^2 d_0)}$$

where j_b is the beam current density, i_b is the emission current, $\alpha = \alpha_0$ is the convergence semi-angle and d_0 the crossover diameter of the beam. The brightness of the source increases linearly with accelerating voltage V_0. (62)

A series of electromagnetic lenses is used to get in shape and focus the electron beam. Electromagnetic lenses are made of many thousands of windings of copper wire inside a soft iron shell, called the polepiece. When an electric current is passed through the windings, both electric E

and magnetic *B* fields are generated, applying a force *F* to the electrons in the beam according to the Lorentz equation:

Eq.21 $$F = e\left(\overline{E} + \overline{v \oplus B}\right)$$

where *v* is the velocity of the electrons in the beam. As electrons pass through the lens, they are subjected to both radial and circumferential forces and so they begin to spiral towards the center of the lens (the optical axis), bringing the beam to focus. The primary electron beam is usually scanned over a square area of the specimen. This scanning typically occurs line by line, with the scanning of each line occurring from left to right over the area of interest, with a fast fly-back from right to left between the lines. The corresponding image is displayed on a monitor, where the screen raster is synchronous with the one of the electron beam. The intensity of each screen pixel is determined by the intensity of the signal arriving at the detector at each point. (62)

2.4.7 Atomic Force Microscopy

Atomic force microscopy is a forefront technique able to let us see and measure the surface structure with resolution and accuracy without precedents. An atomic force microscope (AFM) allows us, for example, to get images showing the individual arrangement of atoms in a sample, or to see the structure of individual molecules. It is rather different from other microscopes, because it does not form an image by focusing light or electrons onto a surface, like an optical or electron microscope: in fact an AFM physically 'feels' the sample's surface with a sharp probe, building up a map of the height of the sample's surface. This is very different from an imaging microscope, which measures a two-dimensional projection of a sample's surface, creating an image free of any height information in it; with a traditional microscope, we must infer such information from the image or rotate the sample to see feature heights. The data from an AFM must be treated to form an image of what we expect to see from a microscope. The main components of an AFM, visible in **Figure 40**, are the microscope stage itself, control electronics and a computer. The microscope stage contains the scanner, which is the mechanism for moving the AFM tip in relation to the sample, sample holder and a force sensor, to hold and monitor the AFM tip. The stage usually also includes an integrated optical microscope to view the sample and tip. Often, the stage is mounted on a vibration isolation platform which reduces noise and increases the resolution obtainable. The control electronics usually appears in the form of a large box interfaced to both the microscope stage and the computer. The electronics are used to generate the signals used to drive the scanner and any other motorized components in the microscope stage. The three basic concepts that one must be familiar with in order to understand the operation of an AFM are piezoelectric transducers (in AFM, often known as piezoelectric scanners), force transducers (force sensors), and feedback control. Basically, the piezoelectric transducer is responsible for the movement of the tip over the sample surface, the force transducer is able to feel

the force between the tip and the surface, and the feedback control provides the signal from the force transducer back in to the piezoelectric, to maintain a fixed force between the tip and the sample. (63)

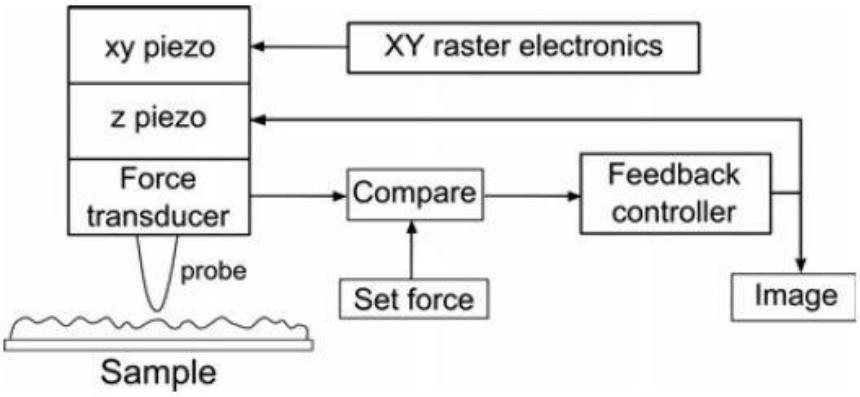

Figure 40 Block diagram of AFM operation (63)

2.4.7.1 Operating Modes

The basis of AFM as a microscopic technique is that it measures the topography of the sample. The datasets generated from this instrument are not conventional images, as produced by optical microscopy, but rather can be intended as a map of height measurements. These may be later transformed into a more naturalistic image with light shading, perspective to help us figure the shape of the sample. In order to make these height measurements, a variety of modes have been developed, and can be divided into those modes which measure the static deflection of the AFM cantilever, and those that measure the dynamic oscillation of the cantilever. The differences between the modes lead not only to different experimental procedures, but to differences in the information available, differing suitability for particular samples, and even to differences in the interpretation of the data. (63)

- **Contact mode**: was the first mode developed for AFM. It is the simplest mode conceptually, and constitutes the basis for the development of the later modes. It is capable of obtaining very high-resolution images. It is also the fastest of all the topographic modes, as the deflection of the cantilever leads directly to the topography of the sample, so no summing of oscillation measurements is required which can slow imaging. In order to understand the way

AFM modes work, it is necessary to use so called force–distance curves. As the name implies, these curves reported in **Figure 41** are a plot of force on the ordinate versus the distance on the horizontal axis. Such a curve is simple to acquire with the AFM. It is calculated from a deflection–distance curve which is easily measured by monitoring the deflection of the cantilever as the piezo is used to move the tip towards the sample. Typically, at a set deflection level, the direction is reversed, and the tip withdraws from the sample. This results in a deflection versus distance curve, which may be converted to a force–distance curve. (63)

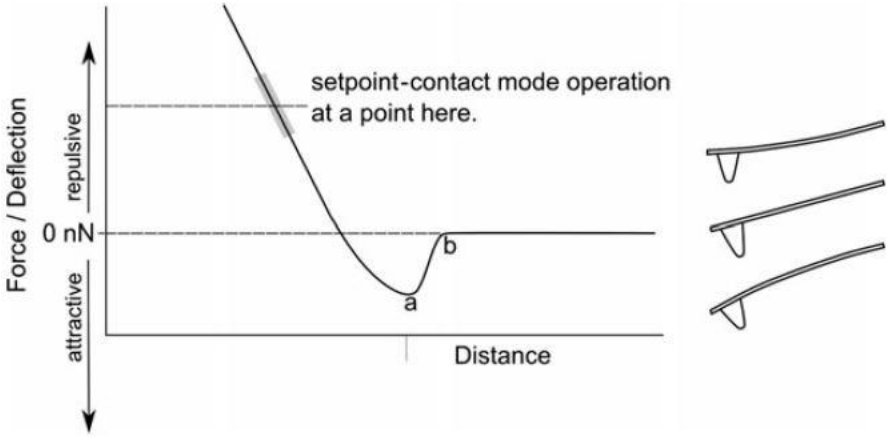

Figure 41 Simplified force–distance curve showing contact (repulsive region) scanning regime (63)

- **Oscillating mode:** the primary motivation for the utilization of oscillating mode in an AFM is to take advantage of the signal-to-noise benefits associated with modulated signals. Thus, an AFM that works in oscillating modes can measure images with a small probe–sample force. There are now a large number of dynamic modes of operation; anyway, all of these modes visible in **Figure 42** are variations on a theme. The cantilever is oscillated, usually with the addition of a piezoelectric element, and typically at its resonant frequency. When the oscillating probe approaches the sample surface, the oscillation changes thanks to the interaction between the probe and the force field from the sample. The effect results in a damping of the cantilever oscillation, which leads to a frequency and amplitude reduction of the oscillation. The oscillation is monitored by the force transducer which is the optical lever, and the scanner adjusts the vertical height via the feedback loop to maintain the probe at a fixed distance from the sample, just as in contact-mode AFM. The only real differences between the various oscillating modes available are in the size or amplitude of the oscillation applied to the probe, and the method used to detect the change in oscillation. (63)

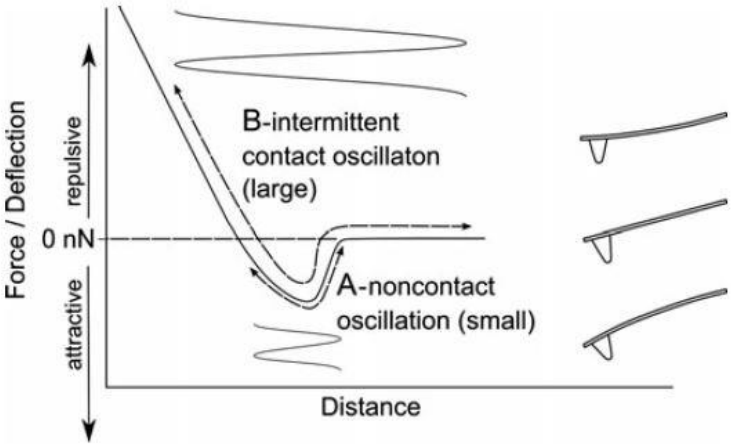

Figure 42 Different operating regimes for oscillating AFM modes. A: with a small amplitude of oscillation, the probe can be kept in the attractive regime. B: with a larger oscillation the probe moves through non-interacting, attractive and repulsive regimes, resulting in intermittent contact. (63)

2.4.7.2 Hardness measurements

The hardness value of a certain sample can be calculated through a nanoscratch resistance test, a test that consists of making different scratches on the sample surface, each of them realized by means of a certain force applied in order not to overcome a certain maximum penetration depth. Surface hardness can be calculated according to the following equation:

Eq. 22

$$Hs = \frac{\eta * F_N}{w^2}$$

Where F_N is the normal force applied to the tip, η is a constant related to the tip geometry and w is the scratch width. The diamond tip usually used has a trapezoidal shape; assuming a tetrahedral geometry on the tip, the constant value η can be calculated using the following equation:

Eq. 23

$$\eta = \frac{4}{\sqrt{3}}\left(1 + \frac{\tan\beta}{\tan\alpha}\right)$$

The setting of the value of the normal force, can be realized on the basis of the position of the photodetector z(t-b) according to the following equation:

Eq. 24

$$F_N = \frac{k * z(t-b)}{sensitivity}$$

Where k corresponds to the spring constant, and is equal to 171 N/m for the diamond tip, and z(t-b) is considered as the vertical displacement of the laser position on the photodetector.

2.4.8 Microindentation Measurements

2.4.8.1 Theory

The nature of the stresses coming from the contact between two elastic bodies has a considerable importance and was first studied by Hertz. He focused on the nature of the localized deformation and the distribution of pressure between two elastic bodies staying in mutual contact. He attempted to assign a shape to the surface of contact that could satisfy certain boundary conditions, namely:

- The displacements and stresses must satisfy the differential equations of equilibrium for elastic bodies, and the stresses must vanish at a great distance from the contact surface.
- The bodies are in frictionless contact.
- At the surface of the bodies, the normal pressure is zero outside and equal and opposite inside the circle of contact.
- The distance between the surfaces of the two bodies is zero inside and greater than zero outside the circle of contact.
- The integral of the pressure distribution within the circle of contact with respect to the area of the circle of contact gives the force acting between the two bodies. (64)

For the case of a sphere, the required distribution of pressure is:

Eq. 25
$$\frac{\sigma_z}{p_m} = -\frac{3}{2}\left(1 - \frac{r^2}{a^2}\right)^{1/2} \qquad r \leq a$$

A description in a mathematical point of view of the indentation stress field associated with a particular indenter needs to start with the analysis of the condition of a point contact. This was studied by Boussinesq in 1885. The so-called Boussinesq solution for a specific point contact allows to determine the stress distribution for any distribution of pressure within a contact area by means of the principle of superposition. Any contact configuration, such as indentation with a spherical or cylindrical flat punch indenter, can be viewed as an appropriate distribution of point loads of varying intensity at the specimen surface, and the stress distribution within the interior is given by the superposition of each of the point-load indentation stress fields.

Figure 43 below summarizes the distribution of surface normal pressures to be considered:

Indenter type	Equation for normal pressure distribution r < a
Sphere	$\frac{\sigma_z}{p_m} = -\frac{3}{2}\left(1-\frac{r^2}{a^2}\right)^{1/2}$
Cylinder 2-D	$\sigma_z = -\frac{2P}{\pi a}\left(1-\frac{x^2}{a^2}\right)^{1/2}$
Cylindrical Flat punch	$\frac{\sigma_z}{p_m} = -\frac{1}{2}\left(1-\frac{r^2}{a^2}\right)^{-1/2}$
Uniform pressure	$\sigma_z = -p_m$
Cone	$\frac{\sigma_z}{p_m} = -\cosh^{-1}\frac{a}{r}$

Figure 43 Equations for surface pressure distributions beneath the indenter for different types of indentations. (64)

2.4.8.2 Microindentation test

Typically, a specimen with polished surface is mounted on the horizontal plate of a universal testing machine. Then the load is applied through an indenter, causing the crosshead of the testing machine to move downward at a constant rate of displacement with time. A clip gauge is attached in order to measure the load-point displacement as shown in **Figure 44**. The output signal from the clip gauge is often interfaced to a computer system that is able to record displacement at regular intervals of time during the application of load. A fully elastic response, for a spherical indenter, is given by:

Eq. 26 $$\delta = \frac{a^2}{R}$$

In order to obtain meaningful results from a compliance test, it is necessary to make certain corrections to the clip-gauge output, according to the nature of the experimental apparatus. For example, in **Figure 44**, the clip gauge is positioned between fixed points on the crosshead post and the indenter surface. The slip gauge thus measures both the indentation and the longitudinal strain arising from the compression of the post. All that is actually required is the displacement of the crosshead arising from indentation of the specimen. (64)

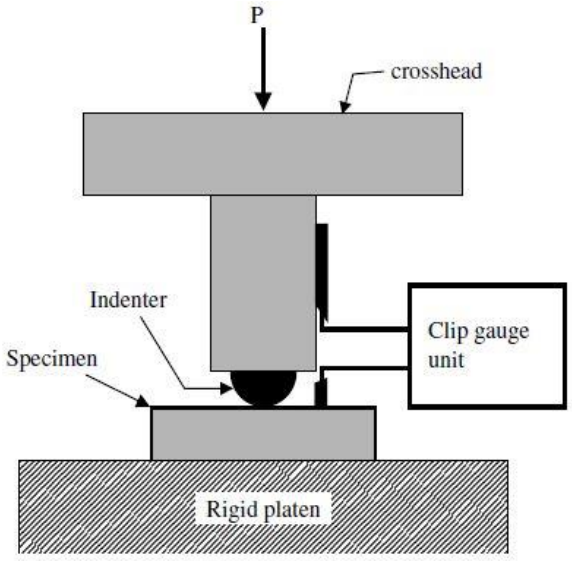

Figure 44 Compliance testing schematic (64)

2.4.8.3 Vickers Hardness Test

The Vickers hardness number is one of the most widely used measurements of hardness. In a typical hardness tester, the diamond indenter is positioned on a sliding plate brought to bear on the specimen, which is mounted on the flat movable plate. The indenter and mechanism can then be moved to the side and a calibrated optical microscope positioned over the indentation to measure the dimensions of the residual impression. **Figure 45** shows typical shapes of indentations made with a Vickers indenter. The Vickers diamond indenter has the form of a square pyramid with opposite faces at an angle of 136° (edges at 148°). The Vickers diamond hardness, VDH, is calculated using the indenter load and the actual surface area of the impression. The resulting quantity is usually expressed in kilogram-force/square millimeters . The area of the pyramid base, at a plane in line with the surface of the specimen, is equal to 0.927 times the surface area of the faces that actually contact the specimen. The mean contact pressure p_m is given by the load divided by the projected area of the impression. Thus, the Vickers hardness number is lower than the mean contact pressure by ≈ 7%. In many cases, it is preferred to use the projected area for determining hardness because this gives the mean contact pressure—a value of some physical significance—while also providing a comparative measure of hardness. The hardness calculated using the actual area of contact does not have any physical significance and can only be used as a comparative measure of hardness. The Vickers diamond hardness is found from:

Eq. 27

$$VDH = \frac{2P}{d^2}\sin\frac{136^\circ}{2}$$

with *d* the length of the diagonal as measured from corner to corner on the residual impression. The projected area of contact can be readily calculated from a measurement of the diagonal and is equal to:

Eq. 28 $$A_p = \frac{d^2}{2}$$

Vickers hardness data are usually quoted together with the load used and the loading time, which corresponds to the one at which full load is applied. (64)

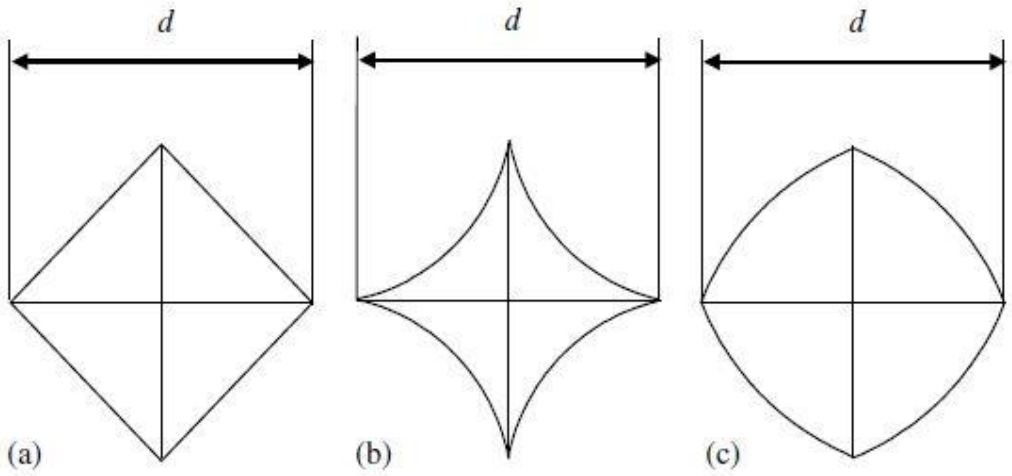

Figure 45 Residual impression made using a Vickers diamond pyramid indenter. (64)

2.4.9 Dynamic Mechanical Analysis

This technique provides information about major transitions as well as secondary and tertiary transitions not readily identifiable by other methods, and also allows characterization of bulk properties directly affecting material performance. DMA can be simply described as the procedure of apply an oscillating force to a sample and of analyze the material's response to that force. From this, one can calculate properties like the tendency to flow, called viscosity, from the phase lag and the stiffness or modulus from the sample recovery. These properties are often described as the ability to release energy as heat through a damping mechanism and the ability to recover from deformation. The applied force is called stress and is denoted by the Greek letter σ. When subjected to a stress, a material will exhibit a deformation or strain, γ. The data obtained in **Figure 46** have traditionally been acquired from mechanical tensile testing at a fixed temperature. The slope of the line gives the relationship of stress to strain and is a measure of the material's stiffness, the so called modulus. It is dependent on the temperature and the applied stress, and also indicates how well a material will work in a specific application in the real world. For example, if a polymer is heated so that it passes

through its glass transition and changes from glassy to rubbery, the modulus will often drop several decades. This drop in stiffness can lead to serious problems if it occurs at a temperature different from expected. (65)

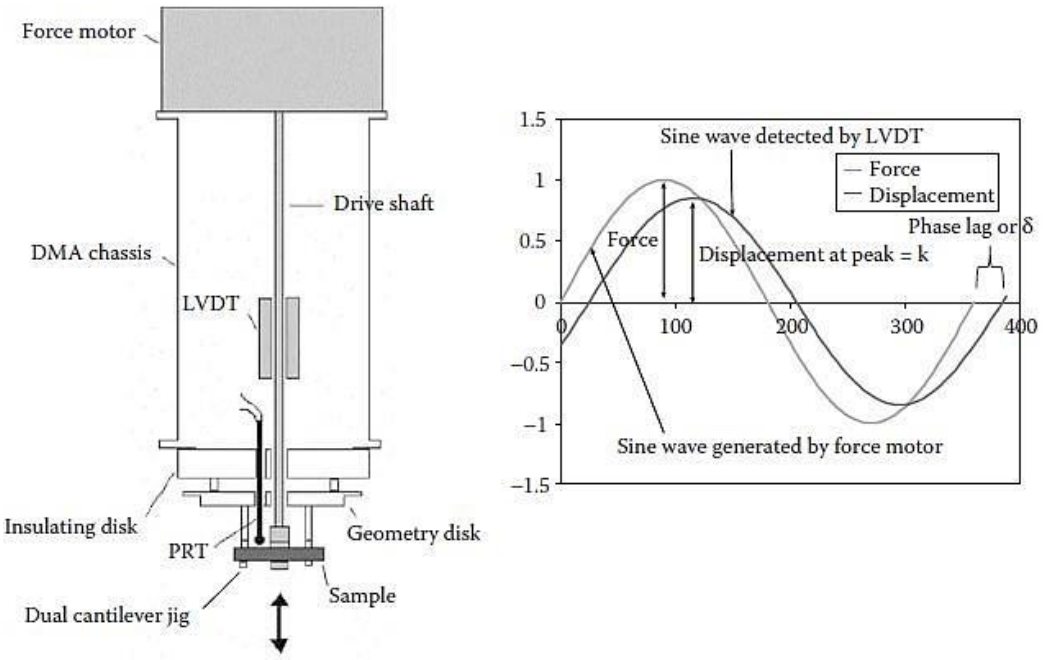

Figure 46 The DMA supplies an oscillatory force, causing a sinusoidal stress to be applied to the sample, which generates a sinusoidal strain. By measuring both the amplitude of the deformation at the peak of the sine wave and the lag between the stress and strain sine waves, quantities like the modulus, the viscosity, and the damping can be calculated. (65)

The modulus measured in DMA is, however, not exactly the same as the Young's modulus of the classic stress–strain curve.As visible in **Figure 47**, Young's modulus is the slope of a stress–strain curve in the initial linear region. In DMA, a complex modulus (E*), an elastic (storage) modulus (E') and an imaginary (loss) modulus (E") are calculated from the material response to the sine wave. These different moduli allow better characterization of the material because we can now examine the ability of the material to return energy (E'), to lose energy (E"), and the ratio of these effects (tan delta), which is called damping. (65)

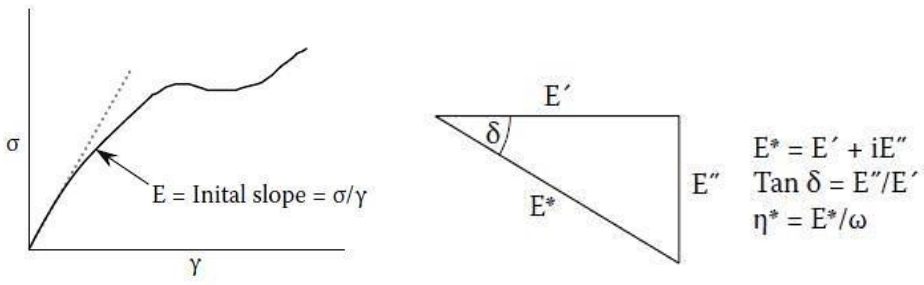

Figure 47 Young's modulus of the classic stress–strain curve and the complex modulus measured in DMA. (65)

2.4.10 Corrosion Measurements

Corrosion is an electrochemical process of oxidation and reduction reactions. As corrosion occurs, electrons are released by the metal (oxidation) and incorporated by elements (reduction) in the corroding solution. Since there is a flow of electrons (current) in the corrosion reaction, it can be measured and controlled electronically; therefore, controlled electrochemical experimental methods can be used to make a characterization of the corrosion properties of metals and metal components in combination with various electrolyte solutions. The corrosion characteristics are unique to each metal/solution system. (66)

Electrochemical reactions visible in **Figure 48** occur in an electrochemical cell with oxidation reactions occurring at one electrode and reduction reactions occurring at the other electrode; they are often defined as either cathodic reactions or anodic reactions. By definition, a cathodic reactions consists of a type of reaction resulting in reduction, such as:

Eq. 29 $M^{2+}(aq) + 2e- \rightarrow M(s)$

An anodic reaction instead is the type of reaction resulting in oxidation, such as:

Eq. 30 $M(s) \rightarrow M^{2+}(aq) + 2e-$

Because of the production of electrons during oxidation and the consumption of electrons during reduction, oxidation and reduction are coupled events. (67)

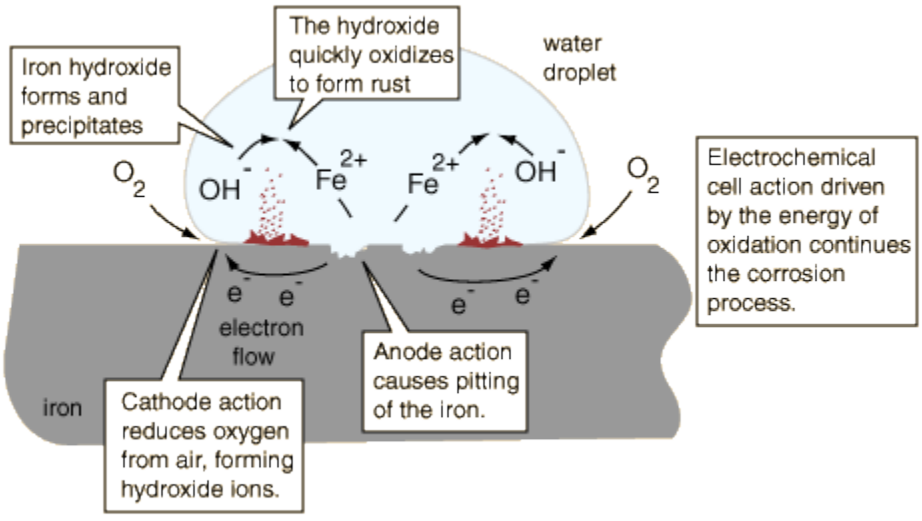

Figure 48 Schematic representation of electrochemical processes occurring on a piece of bare iron left outside where it is exposed to moisture. (68)

2.4.10.1 Testing Procedures

In testing procedures, a polarization cell like the one visible in **Figure 49** is set up as made of the electrolyte 5% NaCl solution , the saturated calomel reference electrode, the coil platinum wire counter electrode, and the metal sample of interest connected to a specimen holder, called the working electrode. The electrodes are connected to an electronic instrument named a potentiostat. The working, reference, and counter electrodes are placed in the electrolyte solution, generally a solution that most closely represents the actual environment of application of the material being tested. In the solution, an electrochemical potential (voltage) is generated between the various electrodes. The corrosion potential (E_{CORR}) is measured by the potentiostat as an energy difference between the working electrode and the reference electrode. (66)

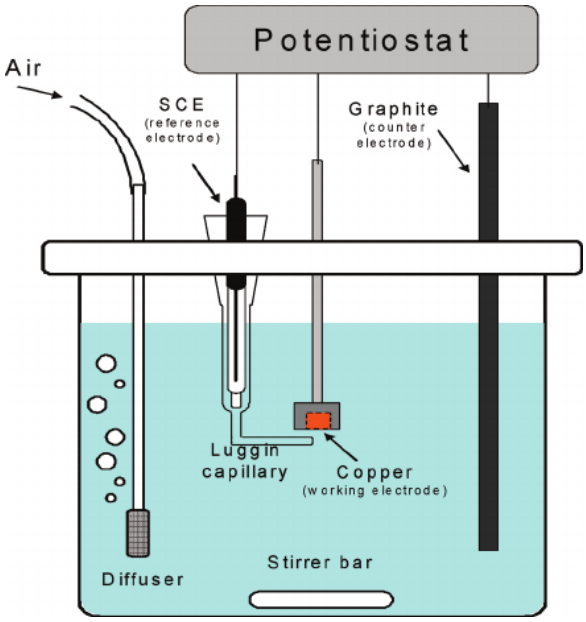

Figure 49 Schematics of the corrosion cell (69)

Electrochemical corrosion experiments measure and control the potential and the current of the oxidation-reduction reactions. Several types of experiments are possible by manipulating and measuring these two variables. In many experiments a potential is fixed on the working electrode and the resulting current is measured. A potentiostatic experiment imposes a constant potential on the working electrode for a specific period of time. The measured current is then plotted versus time. For potentiodynamic experiments, the applied potential is increased with time while the current is constantly monitored. The current or current density is plotted versus the potential. After the potential is scanned to a predetermined current density or potential, the potential scan may be reversed while the current continues to be measured. A potentiodynamic scan like this is called reverse polarization or cyclic polarization. It is also possible to control the current and measure the

resulting potential. Experiments where the current is imposed rather than the potential are referred to as galvanodynamic or galvanostatic. Galvanodynamic methods plot the variation in potential versus the controlled current. Galvanostatic tests maintain a constant current and plot the change in potential verses time. (66)

Potentiodynamic experiments can provide a variety of data connected to the pitting, the corrosion and the passivation behavior of specific sample-solution combinations. Examples of potentiodynamic polarization curves are visible in **Figure 50** below. With the increasing of the potential, pitting corrosion will begin at a certain value known as the breakdown potential (E_B, the lowest potential at which pitting occurs). Since pitting corrosion is related to an increase in the oxidation rate, the E_B is determined by the corresponding increase in measured current. An increase in E_B is associated to an higher resistance to pitting corrosion. As the potential decreases on the reverse scan, there is a decrease also in the current. However, hysteresis can be observed for the reverse scan and a hysteresis loop is traced. The sample is repassivated at the potential where the reverse scan crosses the forward scan. The repassivation potential, or protection potential (E_P), occurs at a lower potential than the E_B. The difference between E_B and E_P is related to susceptibility to crevice corrosion: indeed the greater the hysteresis in the polarization curve, the greater the crevice corrosion susceptibility. Electrochemical corrosion experiments may also be used to determine corrosion rates, active-passive characteristics for a specific sample-solution system, passivation rates, and anodic and cathodic protection. (66)

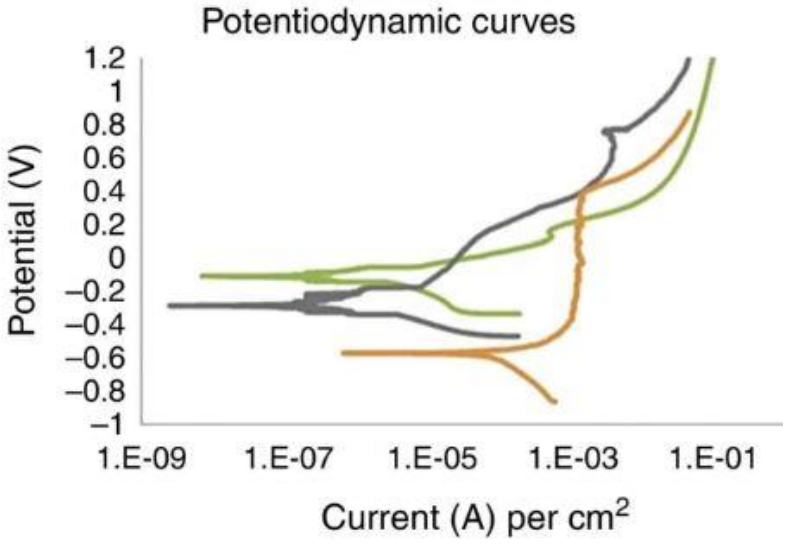

Figure 50 Examples of potentiodynamic polarization curves (70)

References

51. Tetrahydrofuran. *Wikipedia.* [Online] [Cited: November 24, 2016.] https://en.wikipedia.org/wiki/Tetrahydrofuran.

52. **S. M. Akers, J. L. Conkle, S. N. Thomas,K.B. Rider.** Preparation and Viscosity of Biodiesel from New and Used Vegetable Oil. *Journal of chemical education.* 2006.

53. **M.R. Lin, J.-Y. Yan, L.H. Chen, C.L. Liao.** *Composition for photosensitive organic dielectric material and application thereof. US20100084636* October 16, 2012.

54. p-Toluenesulfonic acid monohydrate. *Sigma Aldrich.* [Online] http://www.sigmaaldrich.com/.

55. **G. Griffini, V. Passoni, R. Suriano, M. Levi, and S. Turri.** Polyurethane Coatings Based on Chemically Unmodified. *Sustainable Chem. Eng.* 2015.

56. **Brown, M..** *Handbook of Thermal Analysis and Calorimetry.* s.l. : Elsevier, 2013.

57. **M. Y. Misutsu, L. F. Cavalheiro, T. G. Ricci, L. H. Viana, S. C. de Oliveira, A. M. Junior and L. C. S. de Oliveira.** Thermoanalytical Methods in Verifying the Quality of Biodiesel. *InTech.* 2015.

58. **K.L.Mittal.** *Advances in contact angle, wettability and adhesion* . Wiley.2015.

59. **Stamm, M.** *Polymer Surfaces and Interfaces.* s.l. : Springer, 2008.

60. **F. Awaja, M. Gilbert , G. Kelly, B. Fox, P. J. Pigram.** Adhesion of polymers. *ScienceDirect.* 2009, pp. 948–968.

61. **Stuart, B.** *Infrared Spectroscopy: fundamentals and applications.* s.l. : Wiley, 2004.

62. **Stokes, D. J.** *Principles and Practice of Variable Pressure/Environmental Scanning Electron Microscopy (VP-ESEM).* s.l. : Wiley, 2008.

63. **P.Eaton, P.West.** *Atomic Force Microscopy.* s.l. : Oxford University Press, 2010.

64. **Fischer-Cripps, Anthony C.** *Introduction to Contact Mechanics.* s.l. : Springer, 2007.

65. **Menard, K.P.** *Dynamic Mechanical Analysis.* s.l. : CRC Press, 2008.

66. Electochemical corrosion testing. *Materials evaluation and engineering.* [Online] http://www.mee-inc.com/.

67. **Jr. Covino, Bernard S., Stephen D. Cramer.** *Handbook of Corrosion: fundamentals, testing and protection.* s.l. : ASM International, 2003.

68. Corrosion as an Electrochemical Process. *Hyperphysics.* [Online] http://www.hyperphysics.phy.

69. **M.K. Hsieh, D. A. Dzombak, R. D. Vidic.** Effect of Tolyltriazole on the Corrosion Protection of Copper against Ammonia and Disinfectants in Cooling Systems. *Industrial & Engineering Chemistry Research.* 2010.

70. **M. L. Lethabanea, P. A. Olubambia,H. K. Chikwanda.** Corrosion behaviour of sintered Ti–Ni–Cu–Nb in 0.9% NaCl environment. *The Journal of Materials Research and Technology.* 2015.

3 RESULTS AND DISCUSSIONS

In this chapter the main results obtained through the different characterization techniques are discussed, all divided in three parts previously identified in Chapters 1 and 2:

- Lignin Polyesters
- Silanized lignin-based coatings
- Lignin-based crosslinked matrices for composite materials

A detailed analysis of the outcomes is provided, in an effort to understand the properties and the behavior of the materials developed in this work.

3.1 Lignin Polyesters

In this section, the esterification reaction between the Soluble Lignin Fraction (SLF) and the Succinic Anhydride (SA) will be discussed. The resulting material, Succinic Anhydride Lignin (SAL), able to self-crosslink, will be compared to:

- SAL with the addition of a crosslinker (CYMEL), in three different ratios.
- SLF with the addition of a crosslinker (CYMEL), in three different ratios.

The formulations will be thoroughly investigated.

3.1.1 Esterification reaction

Five esterification reactions with different weight percentages of Succinic Anhydride (SA) with respect to the number of -OH- groups present in Soluble Lignin Fraction (SLF) ($\%w_{SA}/[OH]_{SLF}$) were executed to find out the best ($\%w/[OH]_{SLF}$) proportion, which it was find out to be dependent on the maximum amount of reactive hydroxyl groups present in the Soluble Lignin Fraction (SLF), pointed out by means of ^{13}C-NMR Spectroscopy. The effect of increase the amounts of SA in the SLF/SA ratio was highlighted by Gel Permeation Chromatography (**Table 7**) and Fourier Transform Infrared Spectroscopy analysis and confirmed what was found by ^{13}C-NMR Spectroscopy .

SAMPLE	SA (%w/[OH]$_{SLF}$)	REACTION TIME (h)	M_w (Da)	Mw (Da)	PDI
SLF	/	/	1736	1800	1.6
SA 103	10	3	2027	2000	1.8
SA 203	20	3	2153	2150	1.8
SA 303	30	3	2795	2800	2.2
SA 403	40	3	2314	2310	1.9
SA 503	50	3	2362	2360	1.9

Table 7 GPC results

The GPC results obtained on the SA XX3 (XX stands for the amount of succinic anhydride used in the three hours reaction with the SLF) samples showed higher molecular weights than SLF sample, clear evidence of the occurred reaction between succinic anhydride and lignin. The maximum M_W was reached for a quantity of 30% of SA. (71)

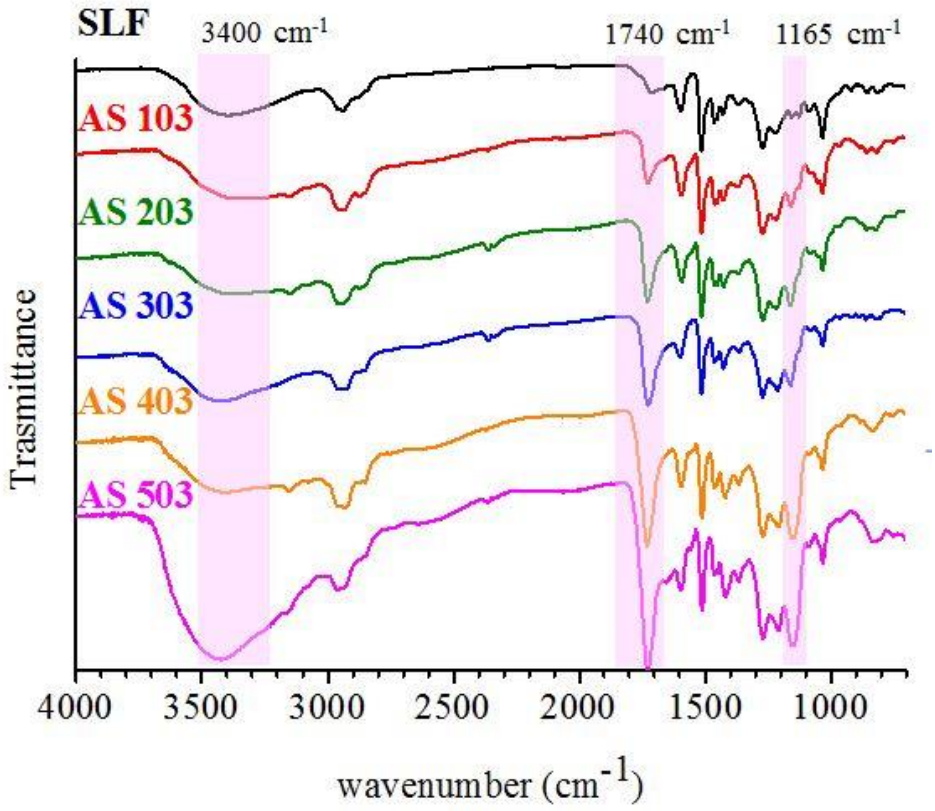

Figure 51 FTIR specta of the SA(X) samples compared to SLF

The SA X03 samples in the FTIR spectra (**Figure 51**) were compared with the starting SLF. In the samples SA 103, SA 203 and SA 303, the esterification resulted in a:

- decrease of hydroxyl group signal of lignin at 3400 $cm^{-1;}$
- major absorption bands at 1740 ÷ 1712 cm^{-1} ,which is attributed to a -COO- stretching;
- peak at 1165 cm^{-1} ,which showed a C-O stretching of the esters;
- absence of bands at 1790 and 1860 cm^{-1} ,which showed no unreacted SA. (71)

Unreacted succinic anhydride is instead visible for the samples SA 403 and SA 503 as shown by shoulder at 1790 cm^{-1} related to SA.

Following these results, the material obtained by reacting SLF with SA in a SLF/SA ratio of 30% was selected as precursor for the preparation of the samples to be crosslinked and characterized. More specifically, the following seven formulations were examined:

- SAL Self: it is the system 100% made of SAL, concentrated at 20%w/v in solution with the THF solvent, with the addition of PTSA (1% w/w with respect to lignin) to catalyze the self-crosslinking reaction.
- SAL-CYM 97-3: system made with the addition of 3%w/w of CYMEL with respect to the SAL, in solution with the THF solvent.
- SAL-CYM 95-5: system made with the addition of 5%w/w of CYMEL with respect to the SAL, in solution with the THF solvent.
- SAL-CYM 93-7: system made with the addition of 7%w/w of CYMEL with respect to the SAL, in solution with the THF solvent.
- SLF-CYM 97-3: system made with the addition of 3%w/w of CYMEL with respect to the SLF, in solution with the THF solvent.
- SLF-CYM 95-5: system made with the addition of 5%w/w of CYMEL with respect to the SLF, in solution with the THF solvent.

- SLF-CYM 93-7: system made with the addition of 7%w/w of CYMEL with respect to the SLF, in solution with the THF solvent.

The samples were spin coated on glass substrates at 600rpm for 40 seconds each; then the crosslinking reaction was achieved by means of a curing process in oven at 200°C for 30 minutes. In **Figure 52** below it is possible to see some of the prepared samples.

Figure 52 Some representative samples realized on glass substrates

3.1.2 Solvent resistance test

To evaluate the extent of crosslinking, solvent resistance tests were performed; in particular, rubbing test with methyl ethyl ketone (MEK) and evaluation of insoluble fraction were executed, according respectively to the ASTM D5402 international standard and to the ASTM D2765 - 11 international standard. It was found that all samples were able to withstand more than 100 MEK double rubs and also to maintain about 99% of initial weight after extraction with solvent Dimethyl sulfoxide (DMSO) and THF. The results clearly confirm the formation of a fully crosslinked network following the reaction between the carboxyl group of SAL or the hydroxyl group of SLF and the methoxy groups of CYMEL. The results of the solvent resistance tests are presented in **Table 8** .

Sample	MEK Rubs	Solvent extraction (DMSO)
SAL Self	> 100	<1%
SAL-CYM 97-3	> 100	<1%
SAL-CYM 95-5	> 100	<1%
SAL-CYM 93-7	> 100	<1%
SLF-CYM 97-3	> 100	<1%
SLF-CYM 95-5	> 100	<1%
SLF-CYM 93-7	> 100	<1%

Table 8 Solvent resistance tests results

3.1.3 FTIR Analysis

The reaction between the carboxyl groups of SAL and hydroxyl groups of SLF with methoxyl groups of CYMEL was confirmed by FTIR analysis made on the samples: the peak obtained at 1739 cm^{-1} ,highlighted in **Figures 53-54** and corresponding to the C=O ester group, became progressively more pronounced with the increasing of the amount of CYMEL in the samples.

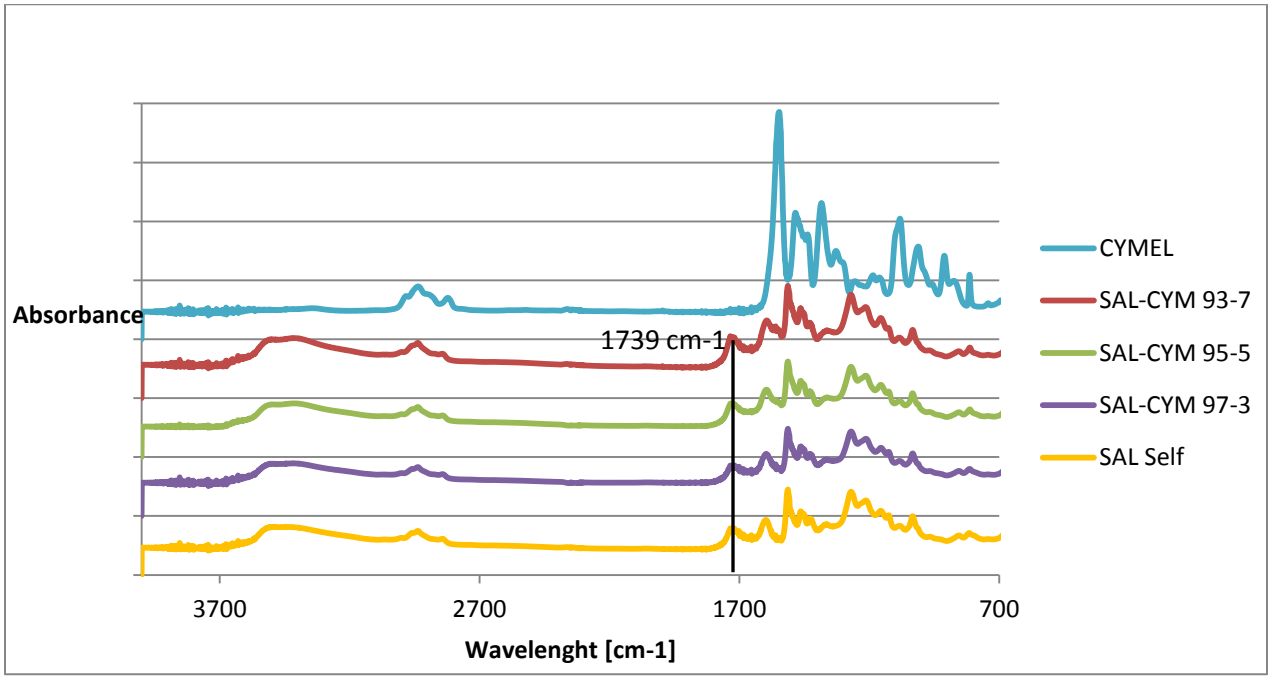

Figure 53 FTIR spectra of SAL Self, SAL-CYMEL and CYMEL samples

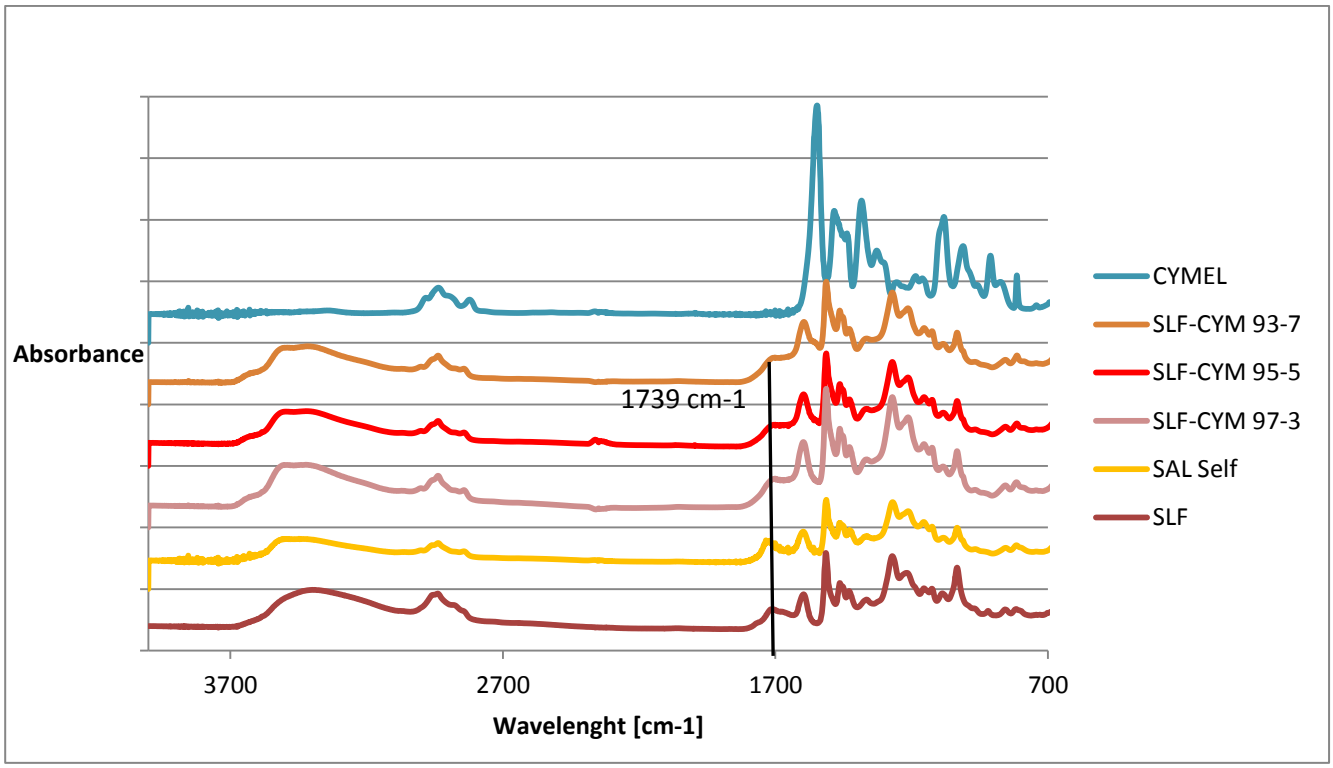

Figure 54 FTIR Spectra of SAL Self, SLF-CYMEL and CYMEL samples

The modification of the C=O peak at 1739 cm^{-1} became clear in the magnification of the spectrum visible in **Figures 55-56**. The latter was done normalizing the intensity of each peak with respect to the intensity of the signal at 1515 cm^{-1} considered as an invariant band: it corresponds to the pure aromatic skeletal vibrations in lignin, the C=C stretching. While **Figure 55** showed an increase of the absorption intensity of the peak going from SAL Self toward SAL-CYM 93-7, instead **Figure 56** showed a modification of the peak position and intensity: the spectra of SLF and SLF-CYM samples presented a less intensive signal of C=O with respect to the SAL Self one clearly above them.

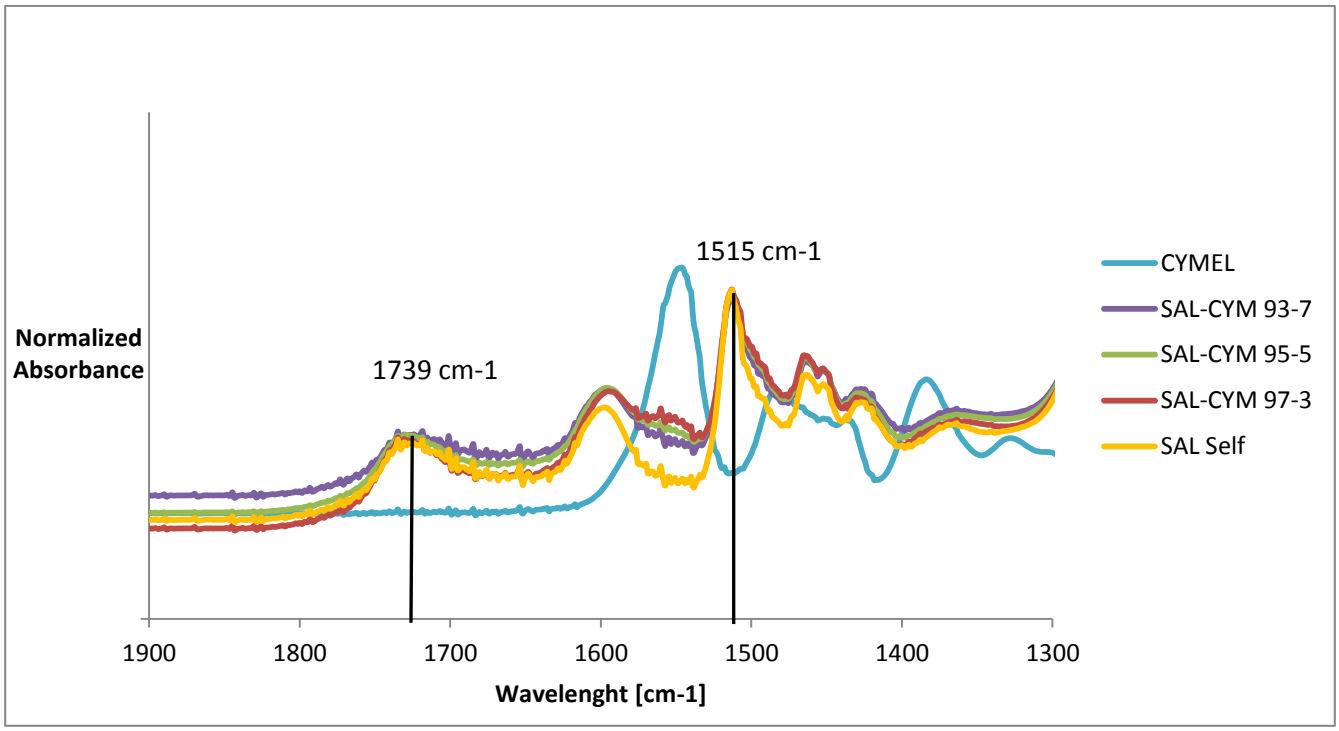

Figure 55 magnification of the FTIR spectra for SAL Self, SAL-CYMEL and CYMEL samples; the intensity of the peak increase going from SAL Self to SAL-CYM 93-7.

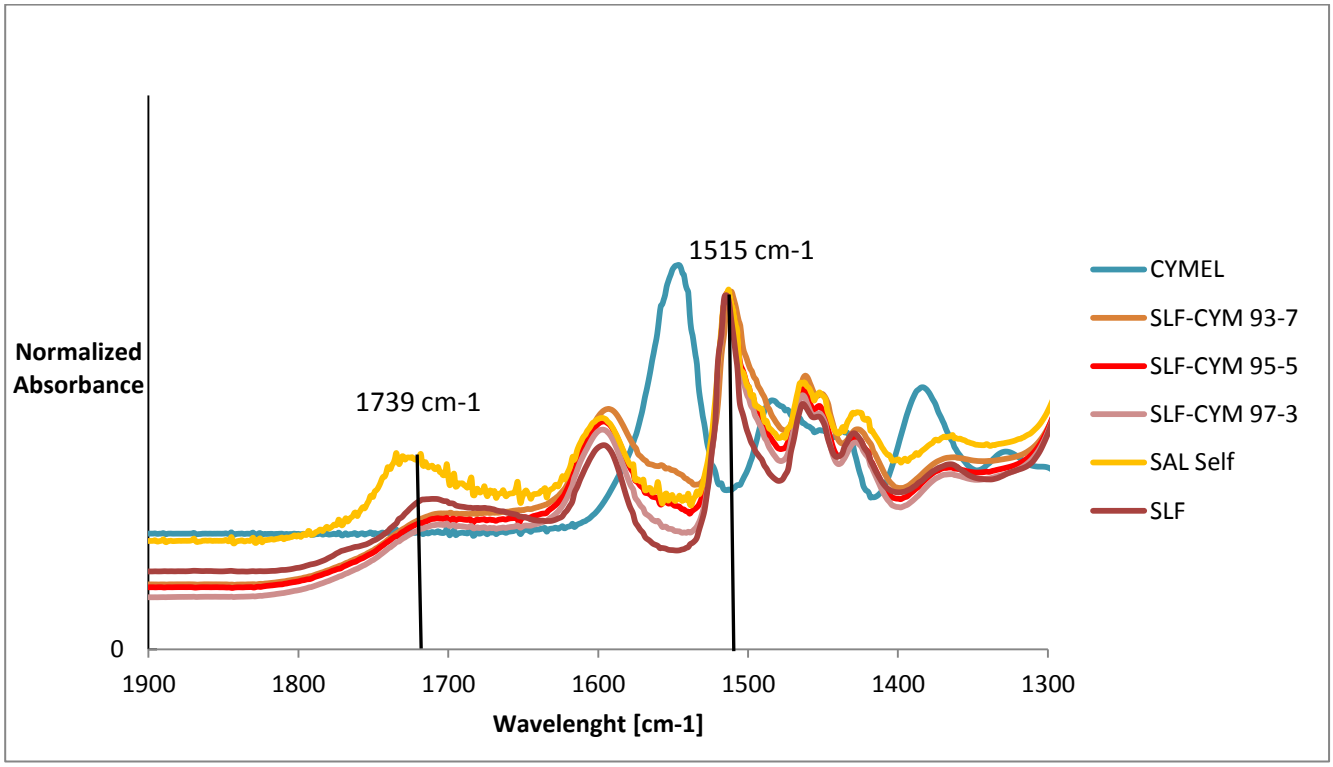

Figure 56 magnification of the FTIR spectra for SAL Self, SLF,SLA-CYM and CYMEL samples; the intensity of the peak varies in intensity and position.

3.1.4 Thermal Analysis

DSC and TGA analysis were performed to understand the thermal behavior of the samples.

3.1.4.1 DSC

It was performed for all the samples at a rate of 20°C/min to measure the transition temperatures (Tg) of the systems. First of all, the SAL Self, SAL-CYMEL and SLF-CYMEL samples visible in **Figures 57-58** showed higher Tg than the uncured SLF(92°C) and SAL(70°C), which indicates that a decrease in the free volume of the molecules took place, as a further confirmation of the occurrence of the crosslinking reaction. In addition, a progressively increase in the value of the Tg was found as the amount of CYMEL was increased: this is due to the higher density of crosslinking. Taking a look at the calorimetric behavior of the SAL samples with respect to the SLF ones, it was possible to notice a difference of 5-10 °C between them: the lower values of the SAL samples were attributed to the internal plasticization effect induced by the addition of succinic anhydride. In the magnification of the **Figures 57-58,** visible in **Figure 59,** SAL-CYM and SLF-CYM samples containing 5% and 7% of melamine have been reported; doing that, it was possible to observe clearly the glass transition temperatures that were not enough visible in the total plots. Results of the DSC analysis are presented in **Table 9**.

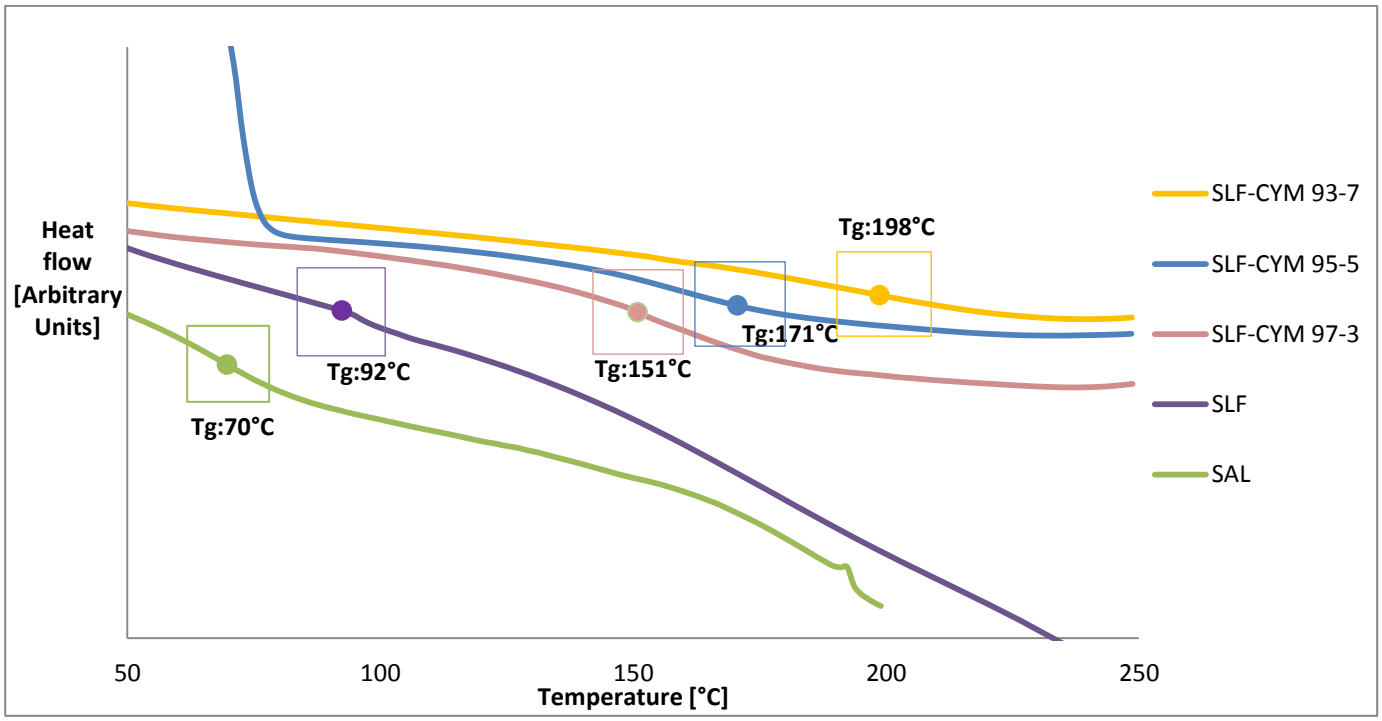

Figure 57 DSC of SAL, SLF and SLF-CYM samples

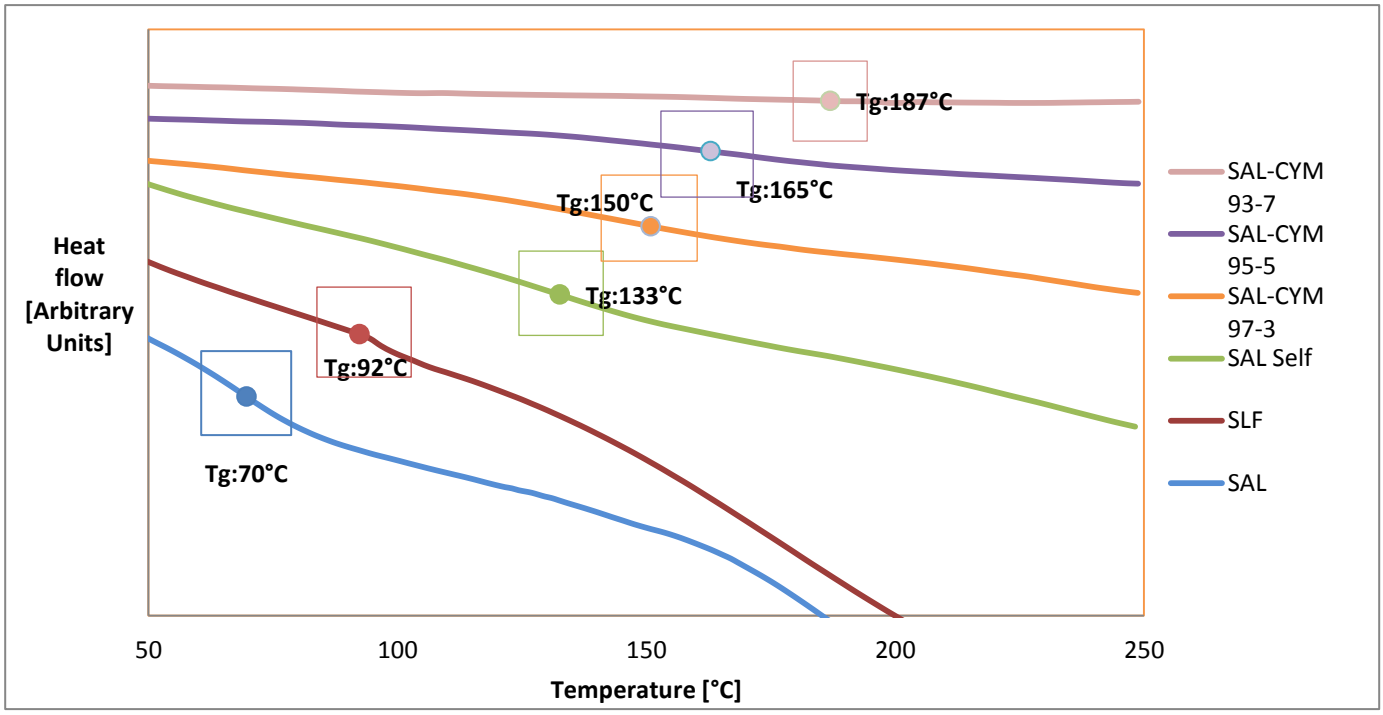

Figure 58 DSC of SAL, SLF, Sal Self and SAL-CYM samples

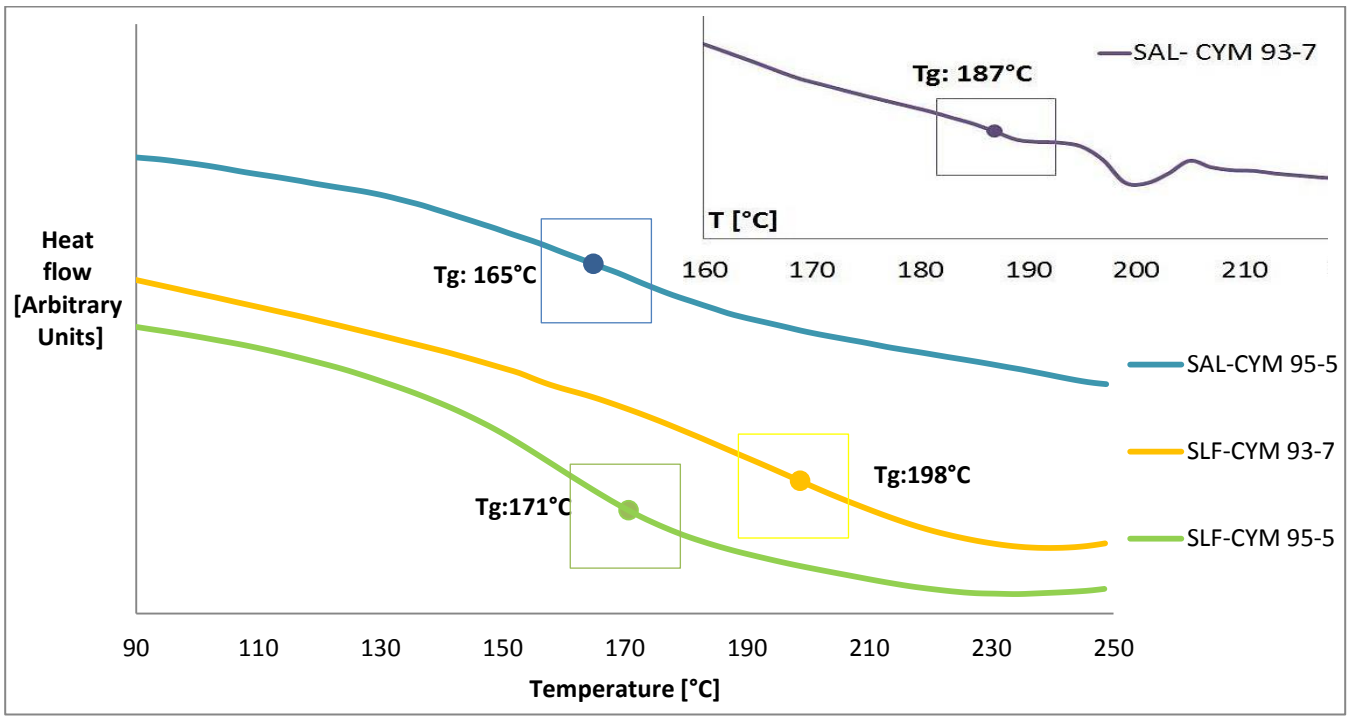

Figure 59 magnification of the DSC curves reporting SAL-CYM and SLF-CYM samples with 5% and 7% of melamine

SAMPLE NAME	T_g [°C]
SAL-CYM 93-7	187
SAL-CYM 95-5	165
SAL-CYM 97-3	150
SAL Self	133
SLF-CYM 93-7	198
SLF-CYM 95-5	171
SLF-CYM 97-3	151
SLF	92
SAL	70

Table 9 DSC temperature values results

3.1.4.2 TGA

The TGA analysis was performed for all the samples at a rate of 10°C/min from room temperature to 800°C, both under air and nitrogen atmosphere. The purpose of this test was to investigate the thermal stability of each system, and to measure the percentage of weight losses at different temperatures. Results are visible in **Figures 60-61-62-63**. In comparison to SLF uncured sample, the seven crosslinked systems showed higher thermal stability than the precursor, a further confirmation of the occurred crosslinking reaction. In particular, the thermal stability slightly increased with the amount of melamine in the samples. In **Table 10** below the values of residual mass at different temperatures are summarized; in particular at 780°C under nitrogen stream the residual masses for SAL-CYM 97-3, 95-5 and 93-7 were 24%, 41% and 46%, while uncured SLF had a residual mass of 25%; similar behavior showed the SLF-CYM 97-3, 95-5 and 93-7, with residual masses of 32%, 37% and 43%. Under air stream instead no significant differences were recorded in residual mass values. The temperatures at which 3% weight loss occurred was greatly increased with respect to the values encountered for the SLF: the SAL Self and the SAL-CYM samples showed 3% weight loss at 203-238 °C according to the different formulations, the SLF-CYM samples at 247-260 °C and the SLF at only 81°C. Likewise, 10% weight loss occurred in SAL Self and SAL-CYM samples at 270-296°C, in SLF-CYM samples at 312-327°C and in SLF at only 135°C.

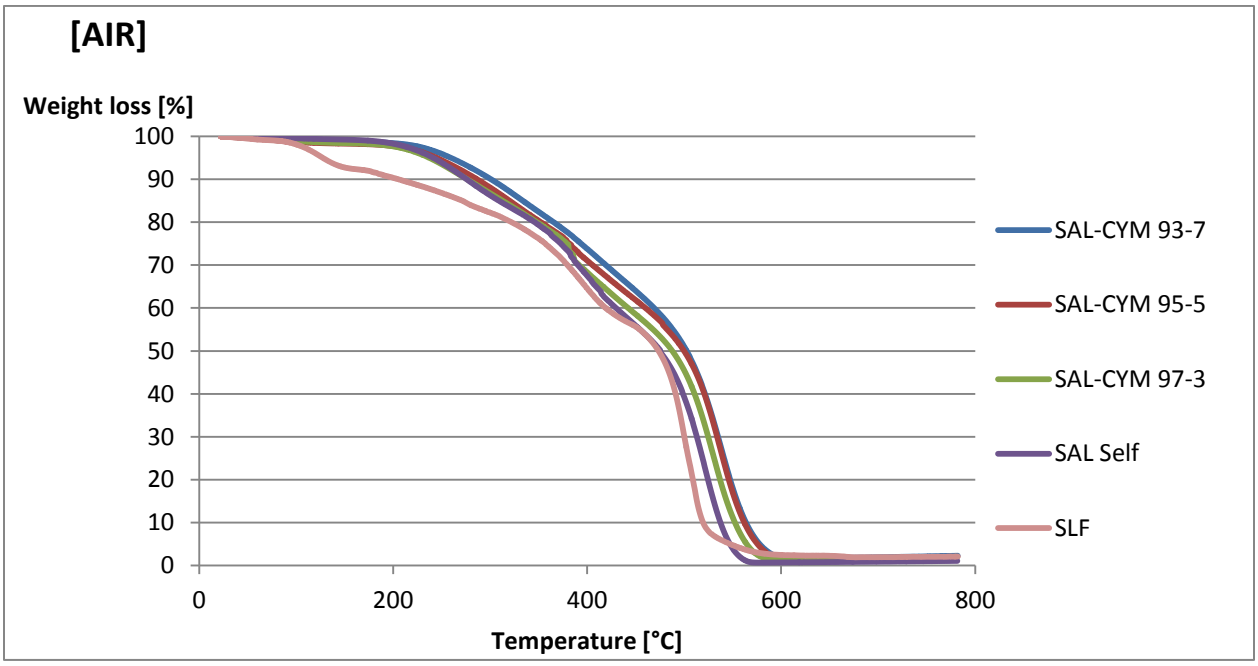

Figure 60 TGA curves of SAL-CYM, SAL Self and SLF samples under air stream

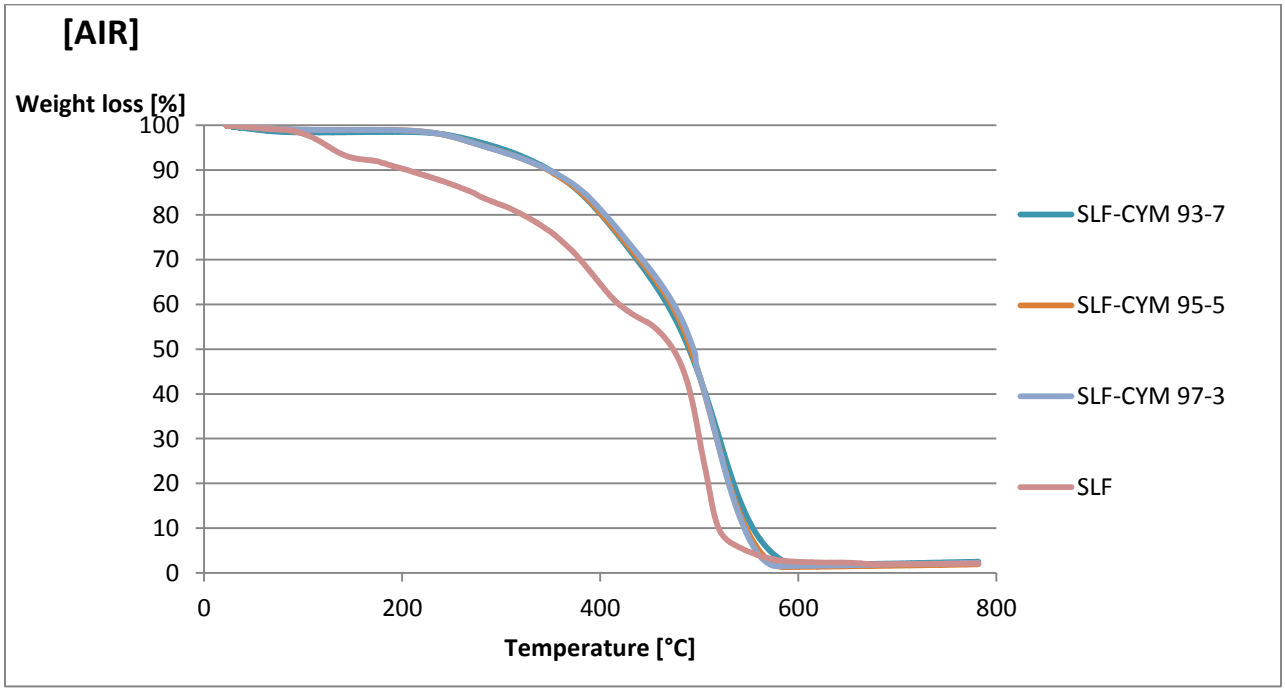

Figure 61 TGA curves of SLF and SLF-CYM samples under air stream

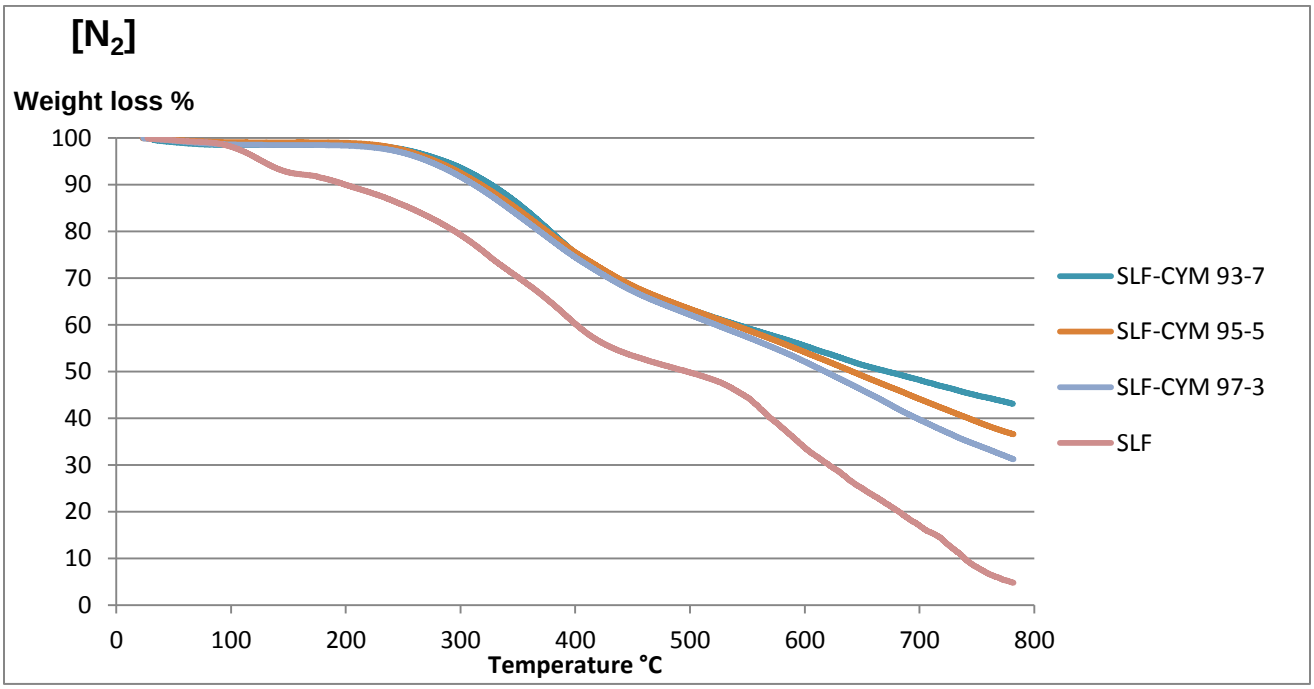

Figure 62 TGA curves of SLF and SLF-CYM samples under nitrogen stream

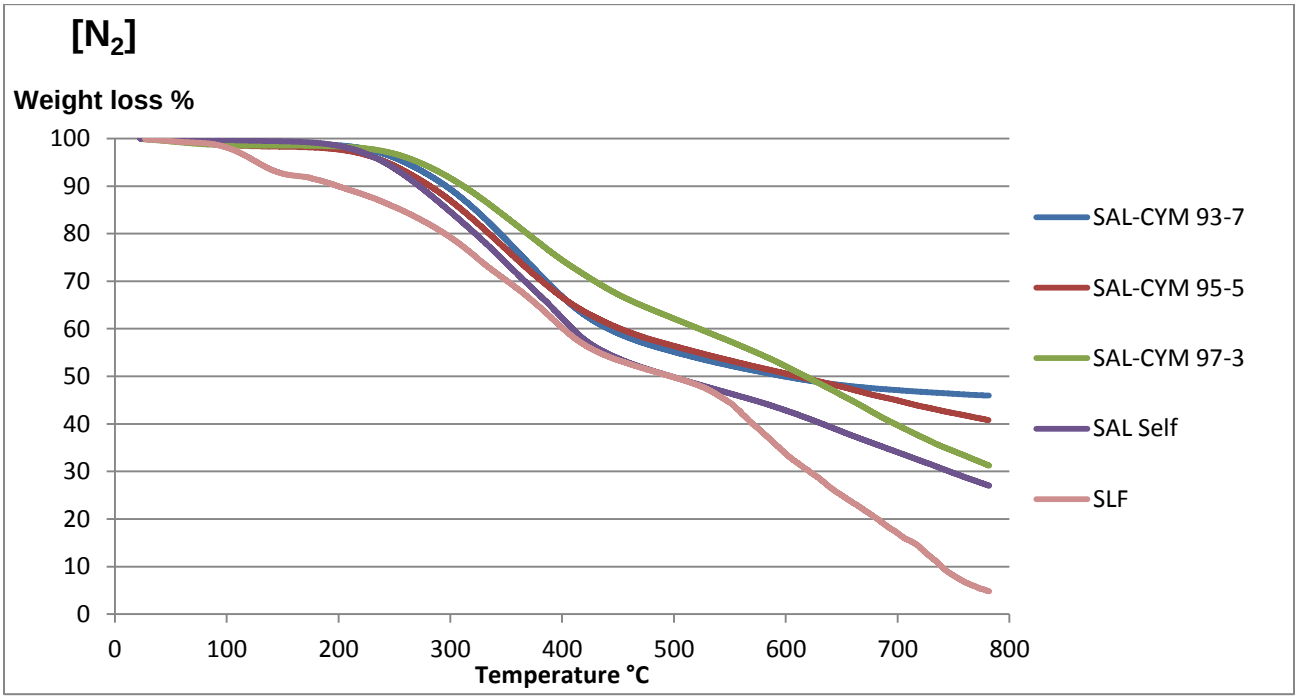

Figure 63 TGA curves of SAL Self, SAL-CYM and SLF samples under nitrogen stream

[N_2]	$T_{3\%}$	$T_{5\%}$	$T_{10\%}$	R_{780}
SAL Self	223	241	272	27
SAL-CYM 93-7	238	260	296	46
SAL-CYM 95-5	217	244	282	41
SAL-CYM 97-3	209	233	270	24
SLF	81	97	135	25
SLF-CYM 93-7	260	286	327	43
SLF-CYM 95-5	256	278	317	37
SLF-CYM 97-3	247	272	312	32

[AIR]	$T_{3\%}$	$T_{5\%}$	$T_{10\%}$	R_{780}
SAL Self	221	241	276	< 5%
SAL-CYM 93-7	237	260	301	< 5%
SAL-CYM 95-5	218	245	286	< 5%
SAL-CYM 97-3	213	237	277	< 5%
SLF	84	100	142	< 5%
SLF-CYM 93-7	264	297	349	< 5%
SLF-CYM 95-5	258	287	347	< 5%
SLF-CYM 97-3	258	286	348	< 5%

Table 10 TGA results: temperatures at which 3%, 5% and 10% weight loss occurs and residual mass values at 780°C in nitrogen and air atmosphere

3.1.5 Mechanical Analysis

The mechanical properties of the systems were examined by means of microindentation tests and dynamic hardness measurements performed by AFM.

3.1.5.1 Microindentation test

To obtain information about the mechanical properties of the seven systems, microindentation test was carried out according to ISO 6441-1 and ISO 6441-2 International Standars, which cover the determination of the indentation hardness of organic material coatings when applied to an acceptable plane rigid substrate like, in this case, glass. The apparatus consisted of a load applicator (a pyramidal shape indenter) and a microscope fitted with a movable micrometer stage. According to the typical testing procedure, the indenter has been put into contact with the test surface with negligible impact, the selected full load has been applied, maintained for a certain period of time and then withdrawn. In this specific case, a maximum force equal to 10 mN has been applied, and the maximum penetration depth obtainable from the application of such a load has been evaluated, with the specific requirement of not to overcome the 10% of the total thickness of each coating. The load history was made of three different steps explained as follows:

1. Load ramp from 0 mN up to the maximum Force (F_{max}) = 10 mN in 60 seconds
2. Keeping the Fmax for 60s;
3. Release of the load till F_{min}, almost 0 mN, in 60 seconds.

The following parameters were obtained as output values for the test:

- HM: Martens hardness in N/mm² at maximum load;
- HIT: Indentation Hardness in N/mm² at maximum load.
- HV: Hardness value according to Vickers.
- E_{IT}: Indentation Modulus expressed in GPa; According to ISO 14577, "*the indentation modulus [..] is comparable with the Young's modulus of the material. However, significant differences between the indentation modulus, EIT, and Young's modulus can occur, if either pile-up or sink-in is present*".
- h_{max}: Maximum indentation depth of the indenter in µm at maximum load. (72).

The results of the test are summarized in **Table 11** below.

NAME OF THE SAMPLE	HM [N/mm²]	HV	H_{IT} [N/mm²]	E_{IT} [GPa]	h_{max} [µm]	Coating Thickness [µm]
SLF	466,51 ±17,8	53,72 ±1,8	568,31 ±18,9	15,61 ±0,8	0,7165 ±0,016	8,34±0,9
SLF-CYM 97/3	551 ±13,3	61,68 ±1,08	652,73 ±11,4	19,67 ±0,6	0,6467 ±0,005	10,21±1,1
SLF-CYM 95/5	561,81 ±55,8	73,92 ±12,7	781,72 ±13,4	16,01 ±0,6	0,6112 ±0.057	9,85±1,5
SLF-CYM 93/7	528,78 ±21,2	61,05 ±3,8	646,02 ±40,3	17,08 ±1,05	0,6635 ±0.026	11,15±1,84
SAL Self	654,63±32,2	71,79 ±3,4	759,63±36,1	26,56 ±1,8	0,5764±0,020	8,23±2,3
SAL-CYM 97/3	581,97±10,6	63,22 ±0,9	669,01 ±9,6	22,76 ±0,6	0,6274 ±0,006	9,93±1,4
SAL-CYM 95/5	573,98 ±17,0	63,23 ±2,4	669,09 ±24,9	22,06 ±0,7	0,63 ±0,014	12,43±2,04
SAL-CYM 93/7	622,88 ±53,9	69,89 ±7,7	739,62 ±41,02	23,36 ±2,8	0,596 ±0,041	10,57±1.9

Table 11 Microindentation results

As is it possible to see, the penetration depth of all the samples didn't exceed 10% of their thickness; the samples reported a value of the Indentation Modulus higher than the uncured SLF sample (15,6 GPa), as a further confirmation of the occurred crosslinking reaction. The numerical values of the detected data, anyway, appeared to be overestimated: the range within the fell is not typical of polymeric materials, even if crosslinked, and neither of lignin itself, which according to literature stands at around 2 GPa (73). The most probable reason able to explain this results is related to the fact that the microindentation test is highly sensible to the thickness of the samples, which often allow the instrument to feel the underlying substrate; this situation is quite common and widely predicted from ISO 14577 International Standard. The modulus values recorder then have been compared to each other's, as indication of a higher rigidity of the crosslinked samples with respect to the uncured SLF.

Taking then a look at the hardness values, SAL Self, SLF-CYM and SAL-CYM systems showed to possess higher Martens Hardness, Vickers Hardness and Indentation Hardness than the uncured SLF. The Martens Hardness values found for the SLF-CYM, SAL Self and SAL-CYM ranged from 528 to 654 [N/mm^2], while the SLF hardness gave a HM value of 466 [N/mm^2], much more low than the

crosslinked samples. Same considerations could be done for the Vickers Hardness values: the SLF-CYM, SAL Self and SAL-CYM showed values ranging from 61 to 73, while the SLF hardness gave a HM value of 53, much more low than the crosslinked samples. The Indentation hardness values found for SLF-CYM, SAL Self and SAL-CYM ranged instead from 761 to 646 [N/mm^2], against the 568 [N/mm^2] of the uncured SLF. Same considerations previously done for the modulus value could be done for the hardness values obtained, which according to literature (74) appeared to be overestimated due to the sensibility of the indenter to the samples thicknesses. Attention should be paid to the fact that the SAL Self system appeared competitive like the SAL-CYM and the SLF-CYM systems even if crosslinked without the addition of CYMEL. The maximum penetration depth, as expected, was obtained for SLF sample with a value of 0,72 µm; the SLF-CYM, SAL Self and SAL-CYM values instead ranged from 0,58 µm to 0,65 µm, as further proof of the higher hardness possessed by the crosslinked formulations that allowed the indenter to reach shorter penetration depths.

3.1.5.2 Dynamic hardness measurements

In this part of the work only three types of samples were examined: SAL Self, SAL-CYM 97-3 and SLF-CYM 97-3.These three systems were selected due to the low amount of crosslinker (0% for the Self and 3% for the SAL-CYM and SLF-CYM), in order to take into account and characterize only the materials with the highest percentage of renewable carbon. Another sample of SAL Self in addition to the previous one was realized with a different coating technique in order to obtain a film with a higher thickness: the bar coating. By means of a glass bar, the solution was manually distributed on the glass substrate, giving after the thermal curing in oven a sample with higher thickness than the equivalent obtained by spin coating.

The dynamic hardness value of the different samples was calculated through a nanoscratch resistance test performed by means of an AFM instrument. To evaluate it, eight scratches of about 12µm length were made in different regions of the sample; four of them were performed at a rate of 0.1µm/s, while the other four were made at a rate of 10µm/s to evaluate the viscoelastic response of the coatings in terms of hardness to the change of velocity. In all of these cases, a force around 66µN was applied, in order not to overcome a maximum depth of penetration of the tip in the sample, which was around 10% of the film thickness. The width of the scratch was evaluated using topographic height images of 20µmxµm at a rate of 0.2Hz; to measure it, a distribution of three different line profiles along the scratch was used, taken away as much as possible from the debris.
Scratch tests indirectly provided an indication of the viscoelasticity of the examined samples: the surface deformation induced by the scratch was responsible for the formation of scratch lines characterized by regions of consecutive cracking. According to the nature of the examined materials, different response could be observed: in crosslinked polymers, the presence of the entanglements

along the polymeric chains did not allow enough mobility and strongly limited the response of the material to the increase of the velocity; as reported in **Table 14,** the penetration depths obtained for the four samples at a rate of 10µm/s were slightly smaller than the ones obtained at 0,1µm/s, and equally the hardness values found for the samples tested at 10µm/s were slightly higher than the ones obtained for the films tested at 0.1µm/s.

Figure 64 shows the formation of the debris on SAL Self spin and bar coated samples during a scratch test performed at 0.1µm/s. For SAL Self deposited using spin-coating it was possible to observe a big amount of debris formation at the bottom of the scratch.
Debris formation on the SAL Self deposited using a bar-coating technique instead seems to be apparently smaller and more homogeneously distributed along the scratch.

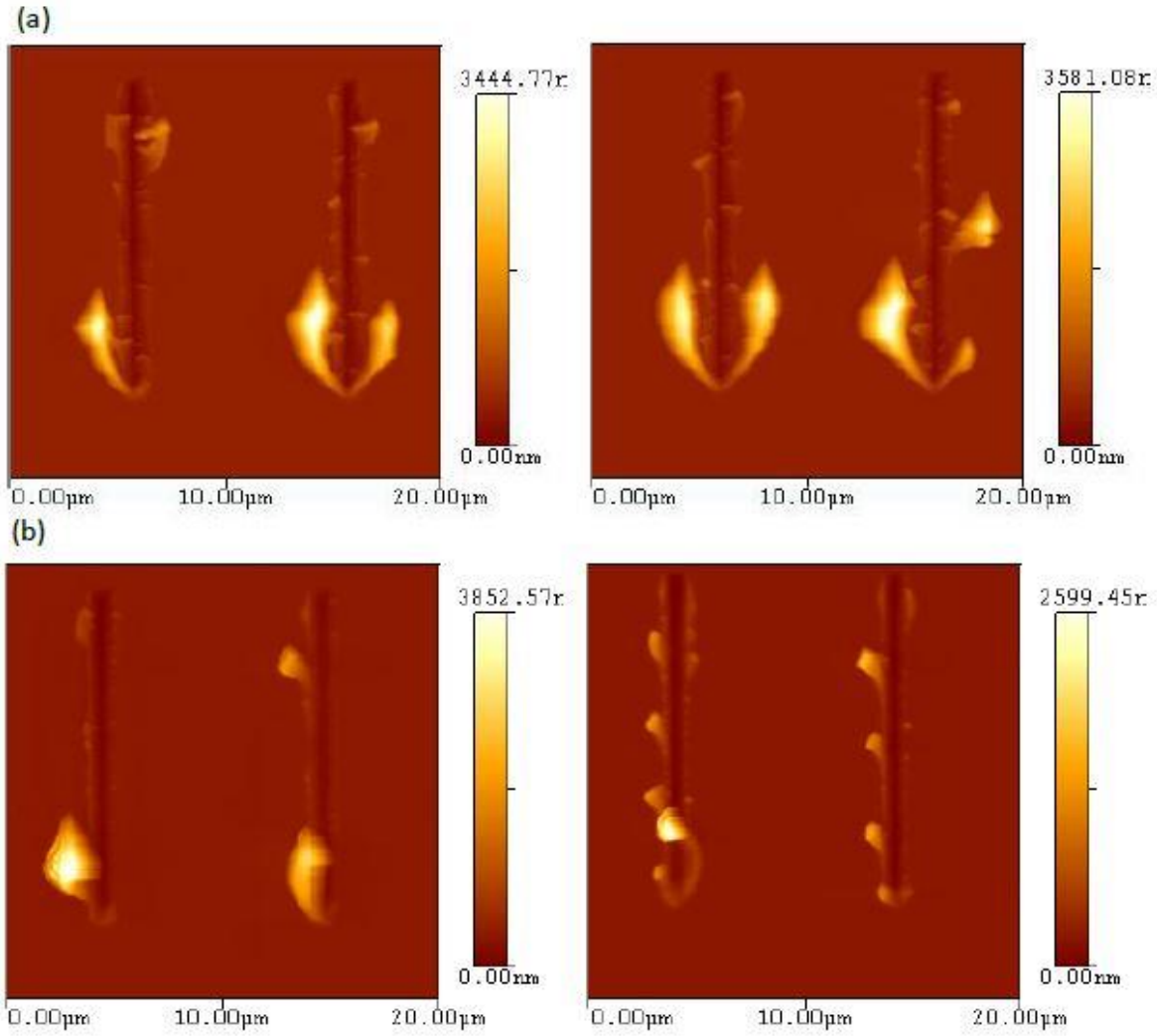

Figure 64 AFM height image (20µmx20µm), scratches performed at 0.1µm/s of: (a) Self crosslinked SAL deposited using spin-coating and (b) Self crosslinked SAL deposited using bar-coating.

Figure 65 shows response of SAL-CYM 97-3 and SLF-CYM 97-3 samples to the scratch performed at 0.1µm/s. While SLF-CYM samples presented a bigger amount of debris formation, especially at the bottom of the scratch, SAL-CYM samples instead presented a very little amount of debris.

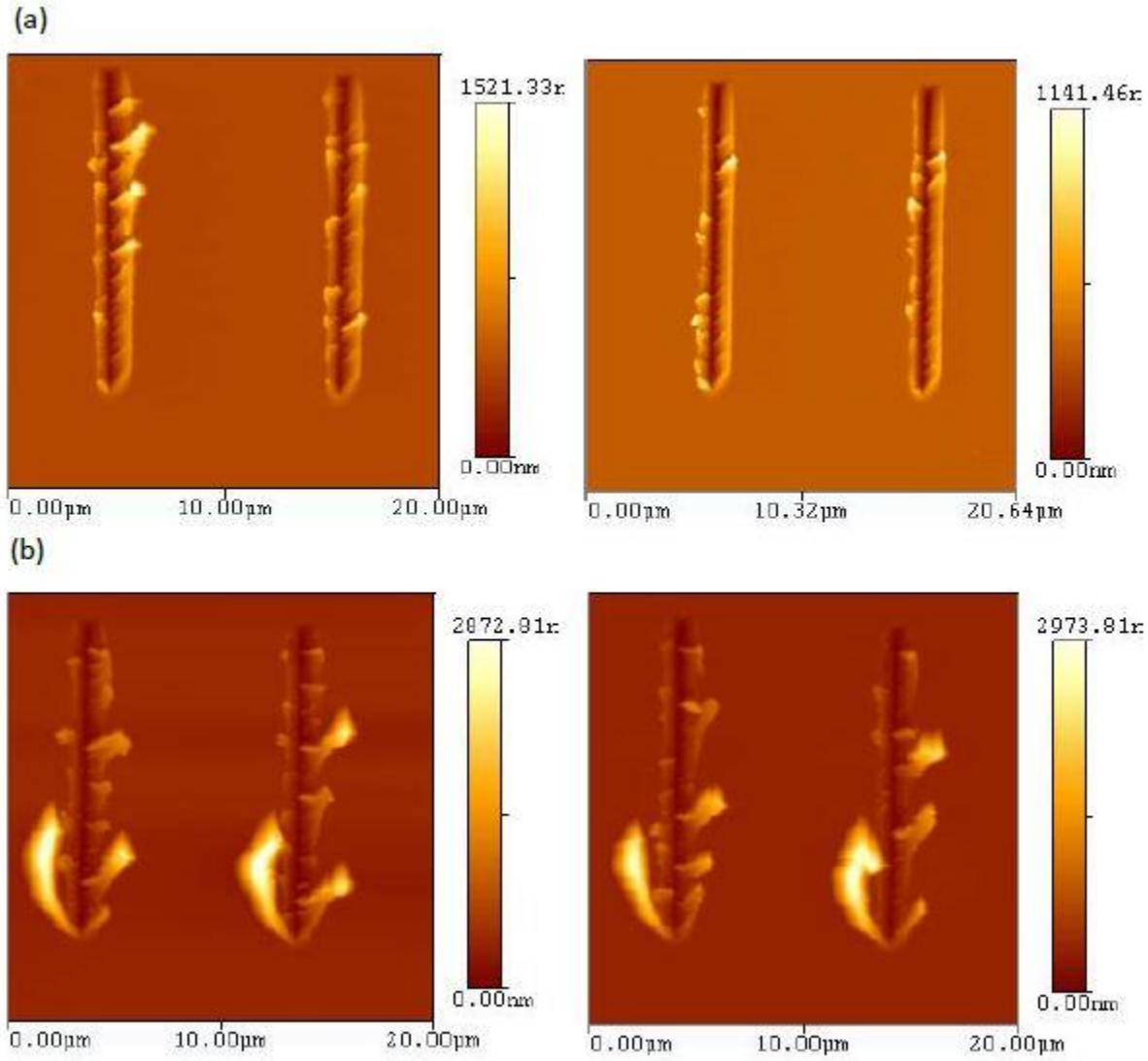

Figure 65 AFM height image (20µmx20µm), scratches performed at 0.1µm/s of: (a) SAL-CYMEL 97-3 and (b) SLF-CYMEL 97-3.

The presence of this debris formation has a match with the hardness results obtained and showed in **Table 12**. A high formation of debris usually is associated to lower values of surface hardness, while little amount of debris is related to higher hardness values.

	Rate = 0.1 µm/sec		Rate = 10 µm/sec	
Samples	**Hardness (GPa)**	**Average depth (nm)**	**Hardness (GPa)**	**Average depth (nm)**
SAL SELF -Spin Coating	0.42 ± 0.08	310 ± 16	0.47 ± 0.06	264 ± 9
SAL SELF - Bar Coating	0.52 ± 0.16	210 ± 49	0.53 ± 0.09	182 ± 18
SAL 97-3	0.63 ± 0.06	275 ± 30	0.64 ± 0.04	266 ± 11
SLF 97-3	0.42 ± 0.07	308 ± 21	0.51 ± 0.01	255 ± 13

Table 12 Hardness of crosslinked lignin based coating

Below in **Figures 66-67** were reported the values of hardness at 10 µm/sec rate. Comparing images, it was possible to observe a slight difference about debris formation when scratch rate was changed from 0,1 µm/sec to 10 µm/sec.

In **Figure 66** comparison between SAL Self spin and bar coated samples has been reported at 10 µm/sec rate; in **Figure 67** showed comparison between SAL-CYM and SLF-CYM samples for a scratch performed at 10 µm/sec. It was possible to observe a greater difference in scratching response of samples of the same type (a and b; c and d). This could be due to the presence of possible dis-homogeneities on the surface of the films.

Values of hardness found from these results could be compared to hardness values, already known in literature, ascribable to polymeric materials like for instance Polycarbonate PC, whose value measured by means of Dynamic Hardness measurement is about 0,2 GPa (75).

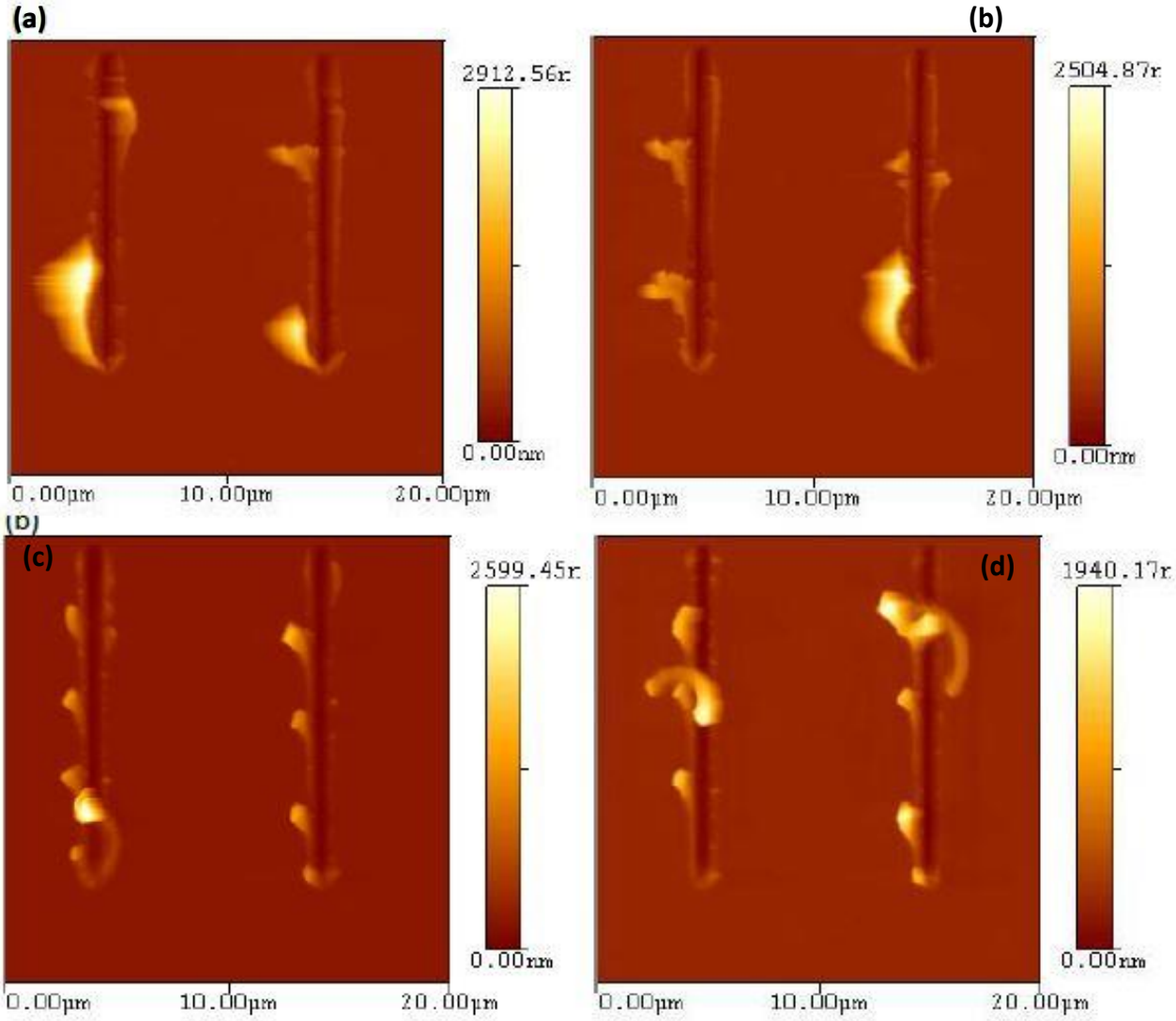

Figure 66 AFM height image (20µmx20µm), scratches performed at 10 µm/s of: (a-b) Self crosslinked SAL deposited using spin-coating and (c-d) Self crosslinked SAL deposited using bar-coating.

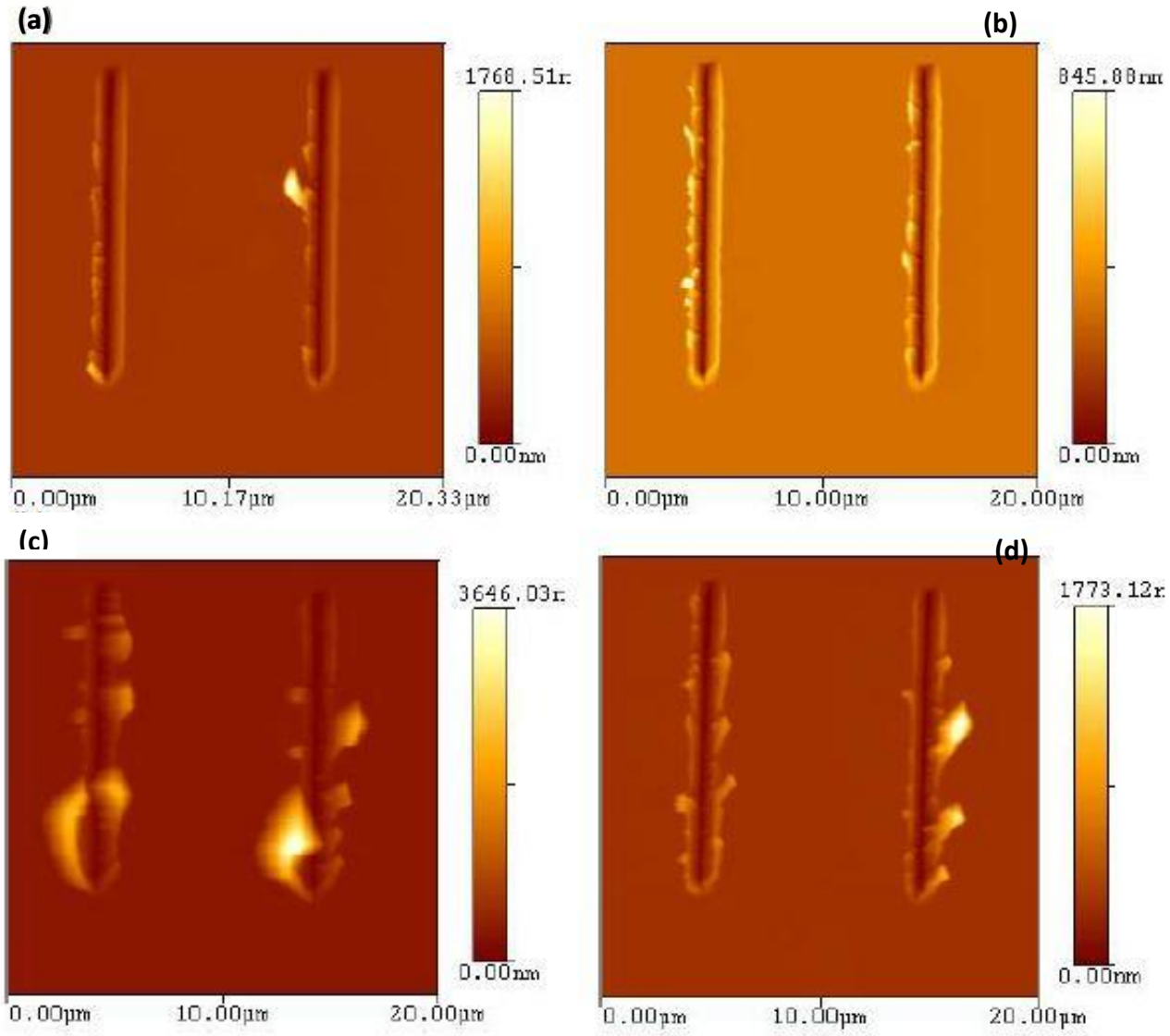

Figure 67 AFM height image (20µmx20µm), scratches performed at 10 µm/s of: (a-b) SAL-CYMEL 97-3 and (c-d) SLF-CYMEL 97-3.

3.1.6 Surface Characterization measurement

3.1.5.2 Surface morphology Analysis

As previously done for Dynamic Hardness measurements, in this part of the work only three types of samples were examined: SAL Self, SAL-CYM 97-3 and SLF-CYM 97-3. Another sample of SAL Self in addition to the previous one was realized with a different coating technique in order to obtain a film with a higher thickness: the bar coating.

A morphology analysis was first carried out by means of AFM instrument on the four samples. Two parameters were taken into account:

- Average Roughness, defined as $S_a = \frac{1}{L}\int |Z(x)|dx$, being Z(x) a function that describes the surface profile related to the height (Z) and position (x), and L the evaluation length.
- Root Mean Square Roughness defined as $S_q = \sqrt{\frac{1}{L}\int |Z^2(x)|dx}$. This parameter is more sensitive to the presence of peak and valleys.

The SAL Self spin coated sample and the SAL Self bar coated sample, visible in **Figures 68-69,** showed pronounced difference in values of Root Mean Square and Average Roughness related to the magnification 50µmx50µm: being the particles of the SAL Self spin coated film much more high than the SAL Self bar coated ones, as visible in **Figures 68 (a) -69 (a)**, these two parameters showed values 0,5-1,5 nm higher than the values obtained for the bar coated SAL Self.

In the higher 10µmx10µm magnification, SAL Self bar coated samples had much larger particles distributed around the surface. This justified the slightly higher values observed on the roughness parameter for the SAL Self sample deposited with bar coating compared with the spin coated one. The high root mean square value obtained in the spin coated sample is due to the presence of high particles in the surface; in the bar coated sample, indeed, due to the manual pressure exerted through the bar on the surface of the sample, the same value was found to be much smaller.

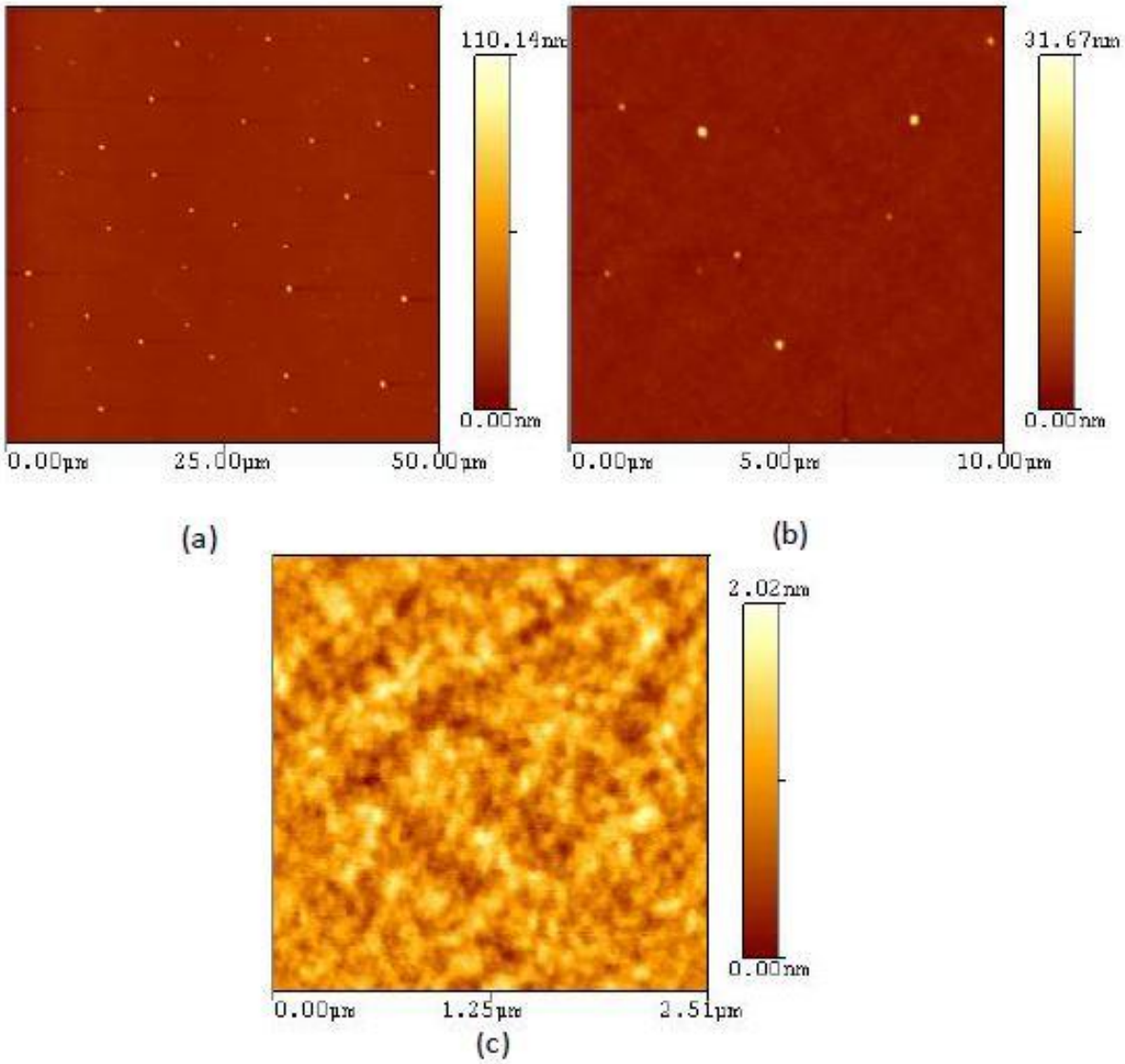

Figure 68 Height images at different magnifications of self-crosslinked SAL deposited using spin coating: (a) 50µmx50µm, (b) 10µmx10µm and (c) 2.50µmx2.50µm

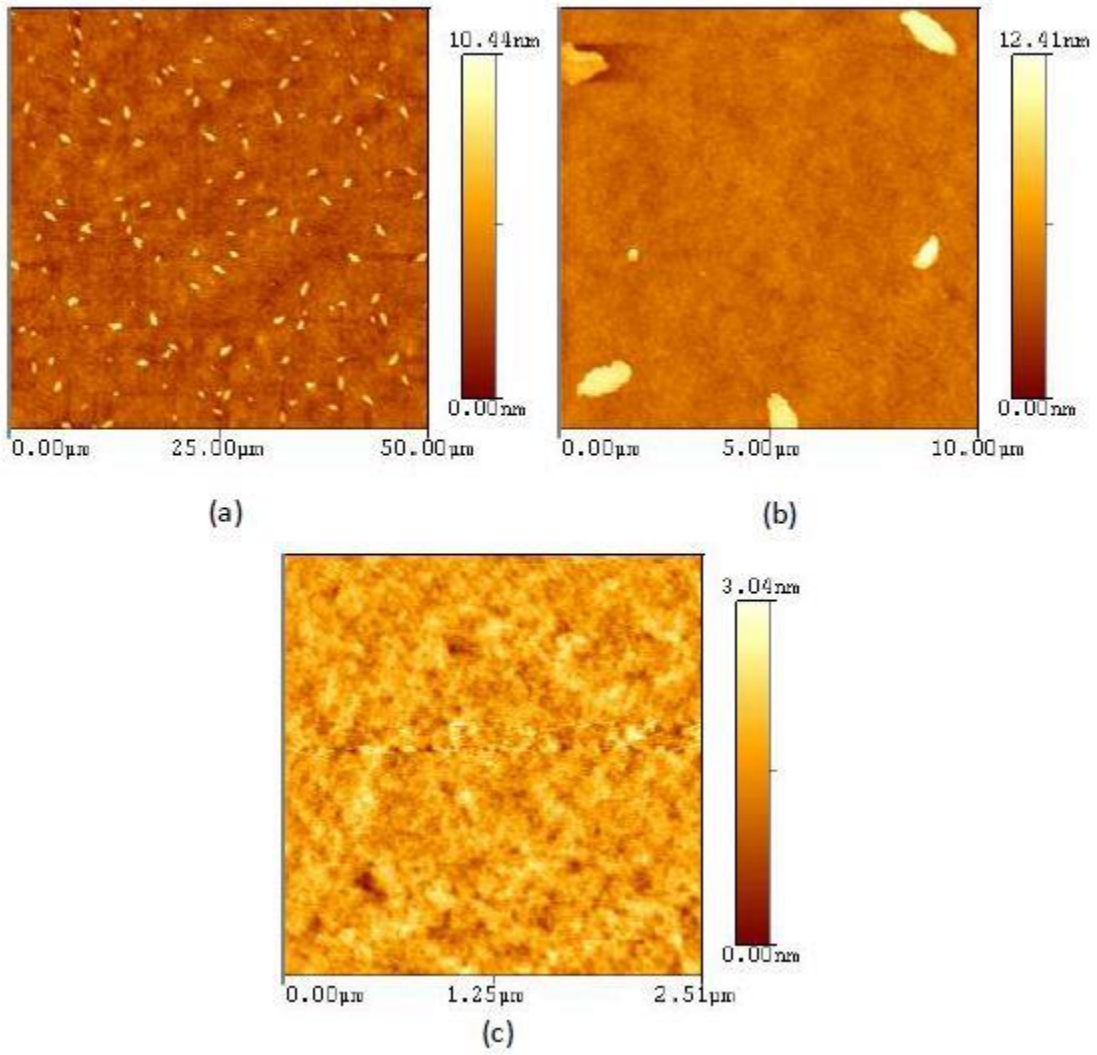

Figure 69 Height images at different magnifications of self-crosslinked SAL deposited using bar coating: (a) 50µmx50µm, (b) 10µmx10µm and (c) 2.50µmx2.50µm.

In **Table 13** below the main results concerning roughness of the two crosslinked samples at different magnifications are reported.

	SAL SELF - Spin Coating		SAL SELF - Bar Coating	
Magnification (µm)	**Average Roughness (nm)**	**Root mean square Roughness (nm)**	**Average Roughness (nm)**	**Root mean square Roughness (nm)**
50x50	0.97	2.79	0.54	0.90
10x10	0.32	0.79	0.50	0.99
2.50x2.50	0.21	0.26	0.26	0.33

Table 13 Roughness parameters on self-crosslink systems using two different deposition techniques

The SAL-CYMEL 97-3 and SLF-CYMEL 97-3 coatings, visible in **Figures 70-71** despite having been obtained by means of the same coating technique, showed pronounced difference in values of Root Mean Square and Average Roughness of the magnification 50µmx50µm: having SAL-CYM 97-3 larger particles on the surface than SLF-CYM 97-3, as visible also in **Figures 70 (a) -71 (a)**, this parameters showed values 1-2 nm higher than the ones obtained for SLF-CYM 97-3.

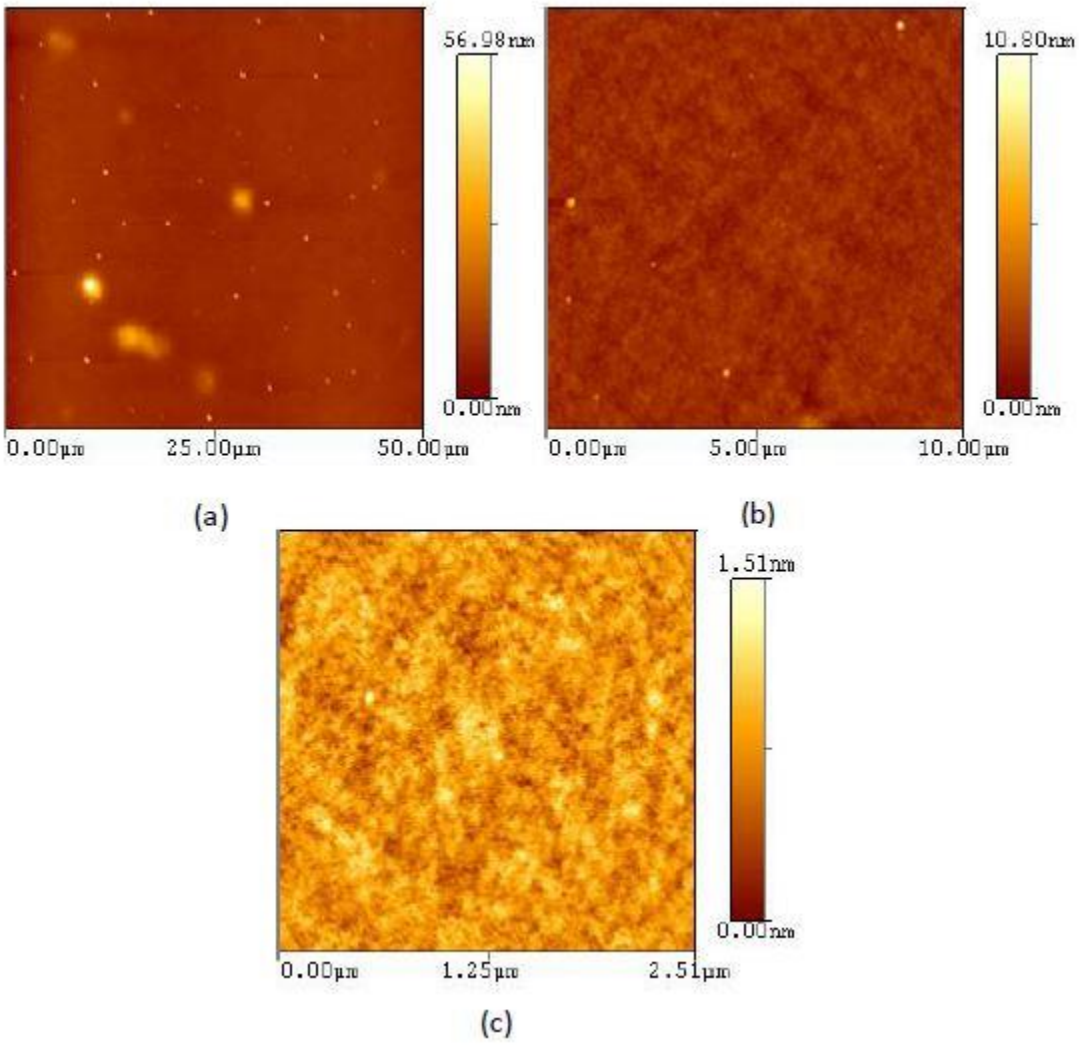

Figure 70 Height images at different magnifications of SAL-CYMEL 97-3: (a) 50µmx50µm, (b) 10µmx10µm and (c) 2.50µmx2.50µm

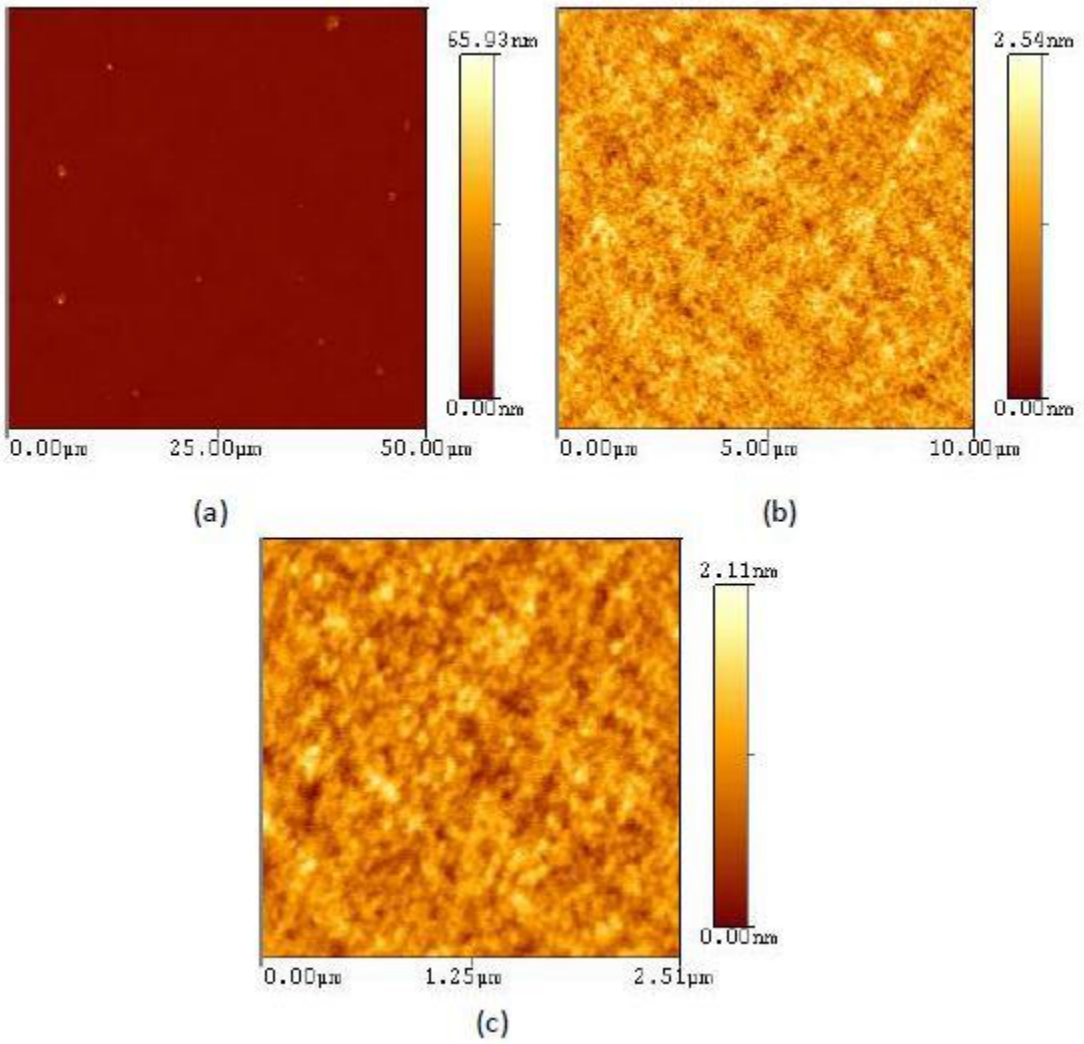

Figure 71 Height images at different magnifications of SLF-CYMEL 97-3: (a) 50µmx50µm, (b) 10µmx10µm and(c) 2.50µmx2.50µm.

In **Table 14** below the main results concerning roughness of the two samples at different magnifications are reported.

	SAL-CYMEL 97-3		SLF-CYMEL 97-3	
Magnification (µm)	**Average Roughness (nm)**	**Root mean square Roughness (nm)**	**Average Roughness (nm)**	**Root mean square Roughness (nm)**
50x50	1.13	3.04	0.33	0.78
10x10	0.29	0.60	0.24	0.30
2.50x2.50	0.16	0.20	0.19	0.24

Table 14 Roughness parameters SAL-CYM 97-3 and SLF-CYM 97-3 systems

3.1.6.1 Optical Contact Angle (OCA)

The surfaces of the seven samples previously introduced were characterized by means of contact angle measurements. In **Table 15** below the different values of contact angle, surface energy and its corresponding polar and dispersive components are summarized. **Figure 72** shows the behavior of the drops spread on the surface of the samples, which progressively become more hydrophilic moving from SAL-CYM toward SLF-CYM samples.

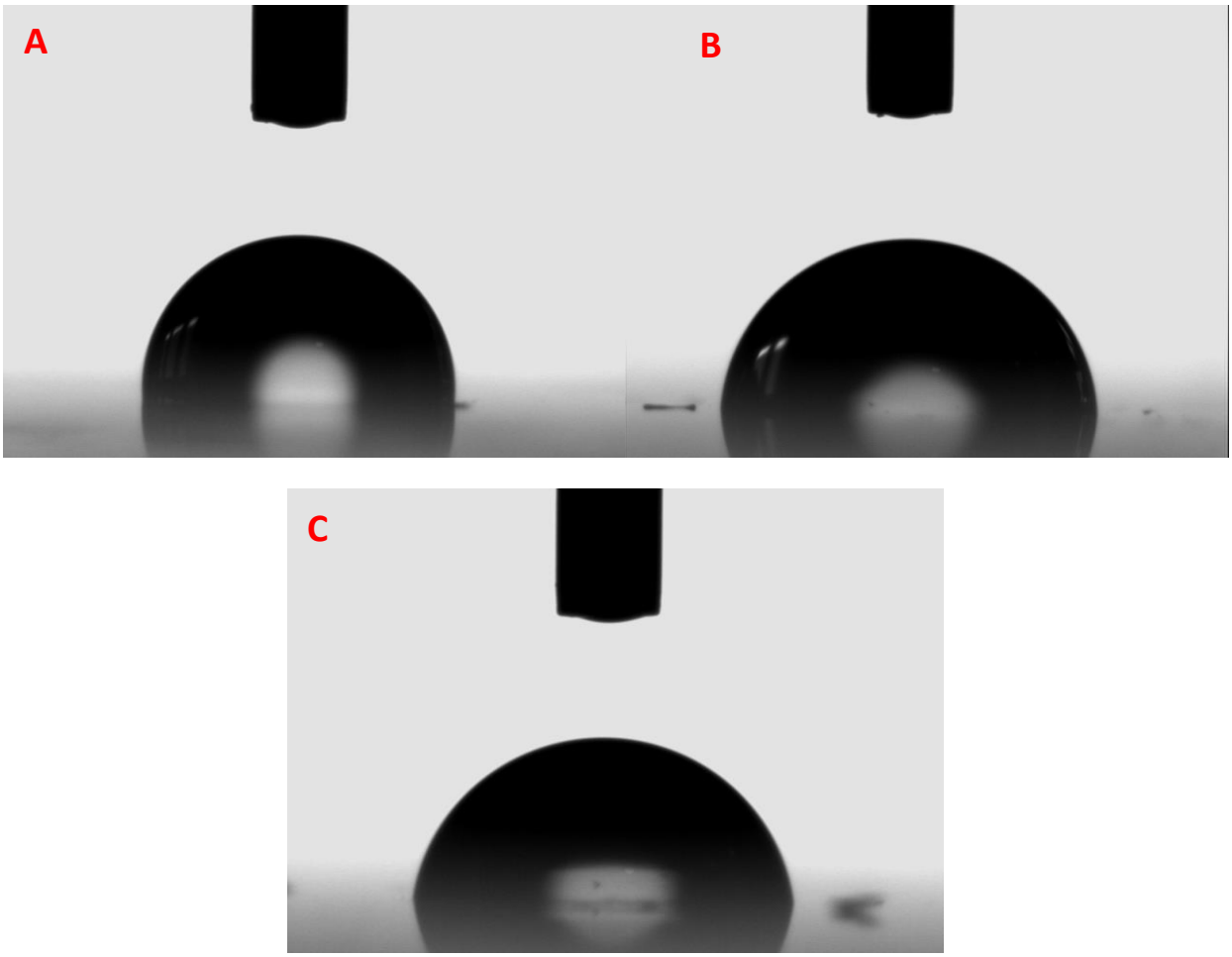

Figure 72 drops spread on SAL-CYM (A), SAL Self (B), and SLF-CYM(C) samples during a contact angle measurement

SAMPLE NAME	θ_{H_2O} [°]	θ_{DIM} [°]	$\gamma_{tot}\left[\frac{mN}{m}\right]$	$\gamma^p\left[\frac{mN}{m}\right]$	$\gamma^d\left[\frac{mN}{m}\right]$
SAL-CYM 93-7	98,8±1,1	53,0±5.3	32,6	0,7	31,8
SAL-CYM 95-5	100,3±0,9	56,6±3,0	30,5	0,7	29,8
SAL-CYM 97-3	94,3±1,9	50,1±3,5	34,3	1,4	32,9
SAL Self	89,9±2,7	47,7±2,3	35,9	2,3	33,6
SLF-CYM 93-7	86,5±2,9	46,3±2,1	37,0	3,3	33,7
SLF-CYM 95-5	85,7±0,9	47,9±1,9	36,4	3,7	32,6
SLF-CYM 97-3	86,2±1,4	48,3±2,6	36,1	3,6	32,5

Table 15 Results of the OCA measurements

The values of contact angles were obtained by using Water and Diiodomethane as probe liquids. The surface energy and its components were computed by means of Owen, Wendt, Rabel And Kaelble (OWRK) method. Dispersive interactions are caused by temporary fluctuations of the charge distribution in the atoms/molecules (van der Waals interaction); polar interactions instead include Coulomb interactions between permanent dipoles and between permanent and induced dipoles (e.g. hydrogen bonds).

Eq. 31
$$\gamma_{sl} = \gamma_{sv} + \gamma_{lv} - 2\sqrt{\gamma_{sv}^d \gamma_{lv}^d} - 2\sqrt{\gamma_{sv}^p \gamma_{lv}^p}$$

In all the samples, the dispersive component of the surface tension did not show great variations; it in fact maintained at values of about 32-36 mN/m; this confirmed that, as expected from the theory, the weak interactions due to the London Forces were not subjected to a significant change. The polar component instead grew slightly passing from the SAL-CYM samples towards the SLF –CYM samples. The reason of the increase could be due to the reaction between the succinic anhydride and the SLF, to form SAL: the esterification reaction made the -OH- groups of the SAL more available to react with CYMEL, so less of them will remain unreacted after the crosslinking reaction to obtain SAL-CYMEL. This could lead to a decrease in the polarity of the system, and then to the reduction of the polar component of the surface energy of the samples. Taking a look at the FTIR spectra of the SAL Self, SAL-CYM and SLF-CYM samples in **Figure 73**, this hypothesis was confirmed: the intensity of peaks relative to the stretching of the OH groups at 3390 cm^{-1} and 2860 cm^{-1} was found to be lower in both the SAL Self and SAL-CYM samples with respect to the SLF-CYM one.

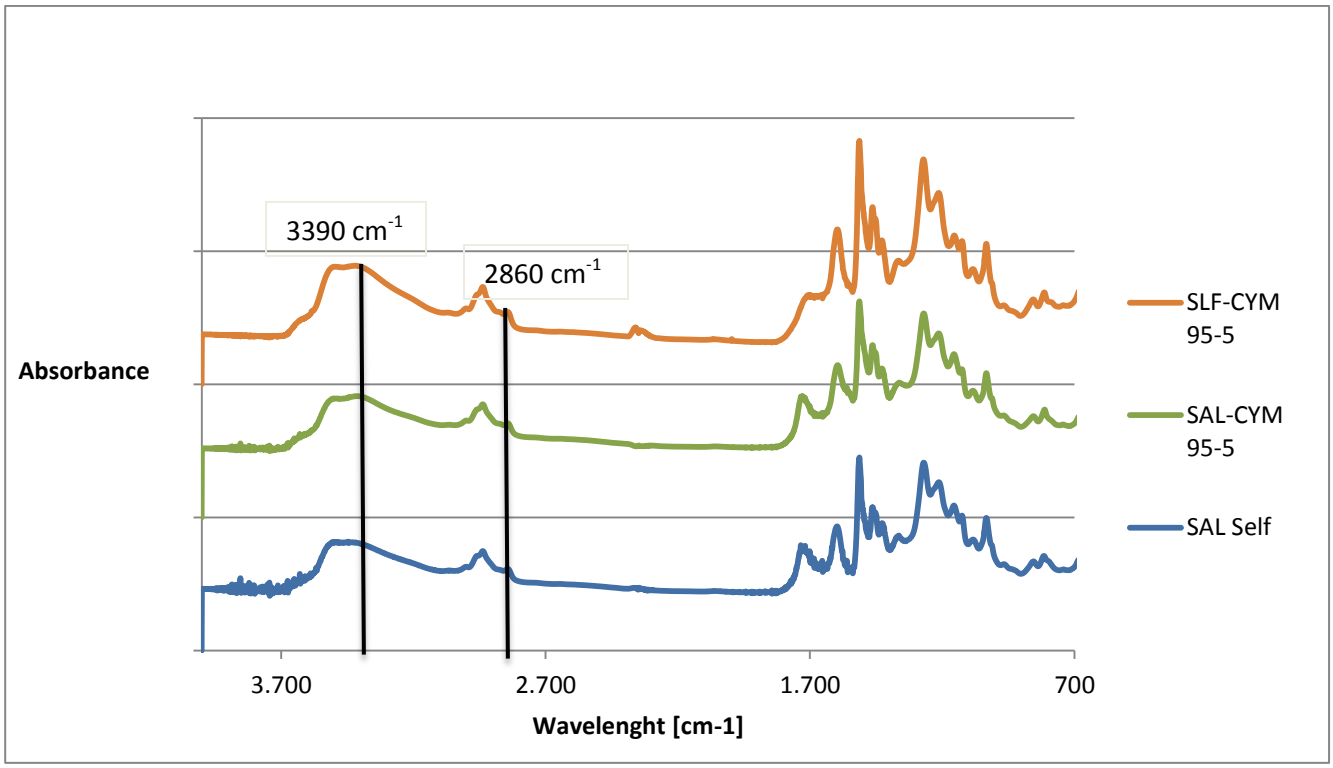

Figure 73 FTIR spectra of the three different samples compared

3.1.6.2 Pull-off Test

To complete the characterization of these samples, adhesion measurements were executed on the systems visible in **Figure 74.** Different substrates were used, in particular glass, aluminum and wood. As reported in **Table 16**, the highest adhesion strength was found with samples coated on wood (> 9MPa); this high adhesion made the wood substrate detach from the whole piece, giving a clear evidence of the strong bond with the coatings. Thinking about the nature of lignin, and about its origin and structure, this result could be totally justified and expected. Very good results were also obtained with the coatings spread on the glass substrates; the values of adhesion force measured were between 4 MPa and 7 MPa. This behavior could be justified by the presence of polar groups in the crosslinked formulations that are responsible for the hydrogen bonding with the glass and wood substrates. The lowest adhesion forces were obtained on aluminum substrate, with values around 1-2 MPa; this results anyway are of particular interest, since they are comparable with values of adhesion of the industrial coatings (primers).

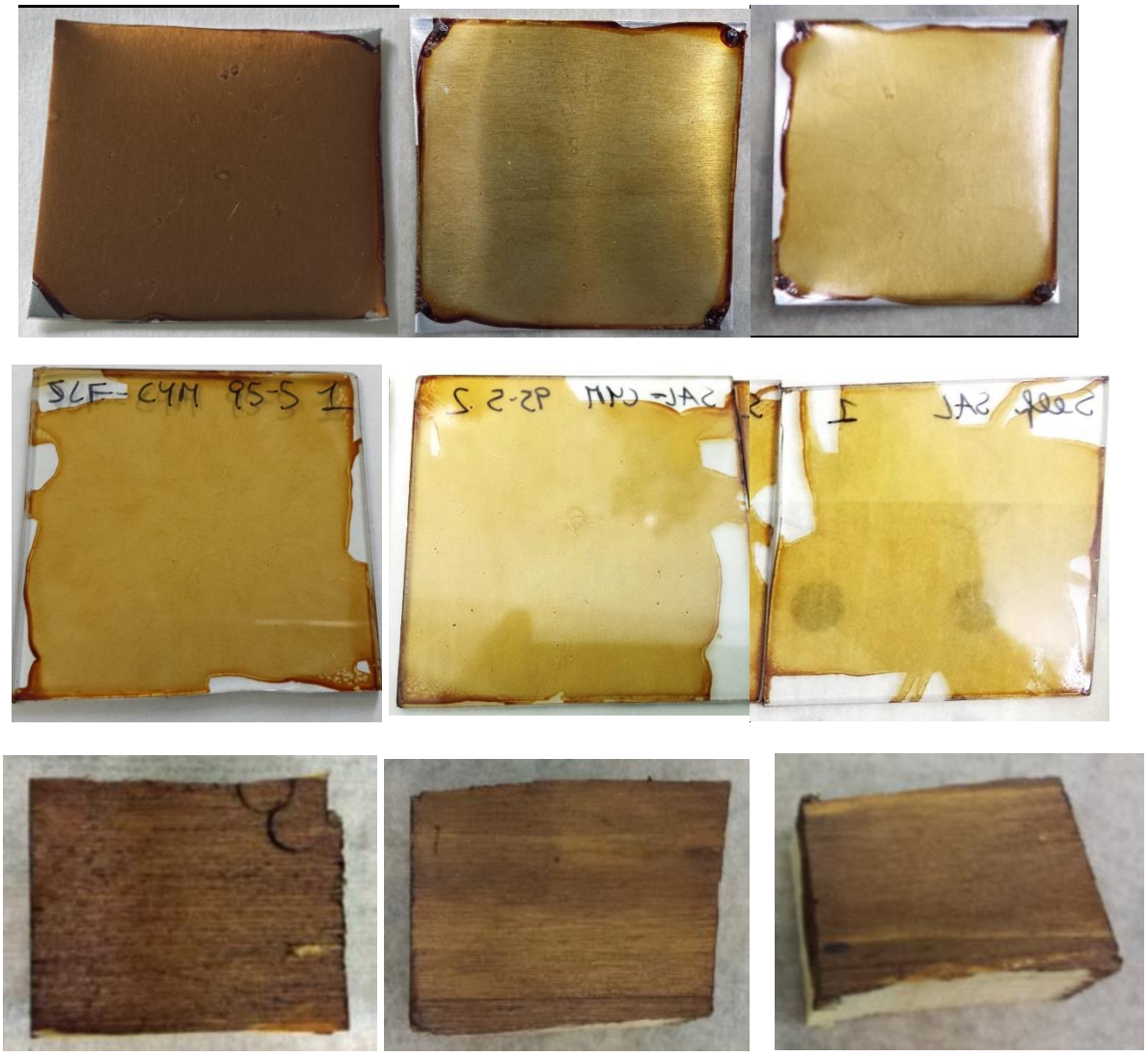

Figure 74 Samples of SLF-CYM, SAL-CYM and SAL Self coatings spread on aluminum, glass and wood

Sample		Adhesion Force (MPa)	
	wood	glass	aluminum
SAL self	> 9	6.5 ± 0.4	1.0 ± 0.1
SAL-CYM 93-7	> 9	7.5 ± 0.1	1.7 ± 0,1
SAL-CYM 95-5	> 9	5.7 ± 1.0	1.6 ± 0.1
SAL-CYM 97-3	> 9	5.7 ± 0.1	1.4± 0.1
SLF-CYM 93-7	> 9	7.1 ± 0.2	1.5 ± 0.2
SLF-CYM 95-5	> 9	4.2 ± 0.9	0.7 ± 0.1
SLF-CYM 97-3	> 9	6.0 ± 0.4	1.2 ± 0.1

Table 16 Pull off results for SAL-CYM, SLF-CYM and SAL Self samples

3.2 Silanized Lignin-based coatings

As explained in details in Chapter 2, four different types of silanized lignin-based coatings were realized and compared:

- LKSi: realized with the Silanized Lignin dissolved in THF solvent at two different concentrations, 20% and 0,5%, with the addition of Acetic Acid (99% pure) in order to obtain a solution with a pH around 3-4.
- LKSi- TEOS: made with TEOS (Tetraethyl orthosilicate, MW=208.33 g/mol; density= 0.933 g/mL) in a ratio of 5% with respect to the LKSi, at two different concentrations with respect to the THF solvent (20%, 0,5%). 3% of distilled water with respect to the solvent was also added, together with Acetic Acid in order to obtain a solution with a pH around 3-4.
- [LKSi]+ GLYCEROL: realized with the Silanized Lignin dissolved in THF solvent at two different concentrations, 20% and 0,5%, with the addition of Glycerol (1.25 g/mL, supplied by Sigma-Aldrich) in a ratio of 10% with respect to the LKSi and of Acetic Acid in order to obtain a solution with a pH around 3-4.
- [LKSi-TEOS]+ GLYCEROL: made with TEOS in a ratio of 5% with respect to the LKSi, at two different concentrations with respect to the THF solvent (20%, 0,5%). 3% of distilled water with respect to the solvent was also added, together with Glycerol in a ratio of 10% with respect to the LKSi and Acetic Acid in order to obtain a solution with a pH around 3-4.

Deposition occurred by means of a spin coater, at 1000 rpm for 80 seconds. The solutions deposited on different substrates were subjected to a thermal treatment of 200°C for 15 minutes. The addition of glycerol as plasticizer in the formulations was done to obtain less rigid coatings with improved film forming properties and able not to fail by cracking during mechanical processes of metal substrates like coil coating. Several characterization measurements were carried out on these samples, in order to evaluate their different properties.

3.2.1 FTIR Analysis

In **Figure 75** below it is possible to observe the different spectra of the LKSi and of the Soluble Lignin Fraction (SLF); two of the main differences in the comparison were found in the intensity of absorption of the OH stretching peaks at 3390 cm^{-1} and 2860 cm^{-1}, which is higher for SLF. This

decreasing in LKSi intensity peaks could be ascribable to the silanization reaction that involved the reactive OH of the SLF, decreasing in the end the number of the unreacted one.

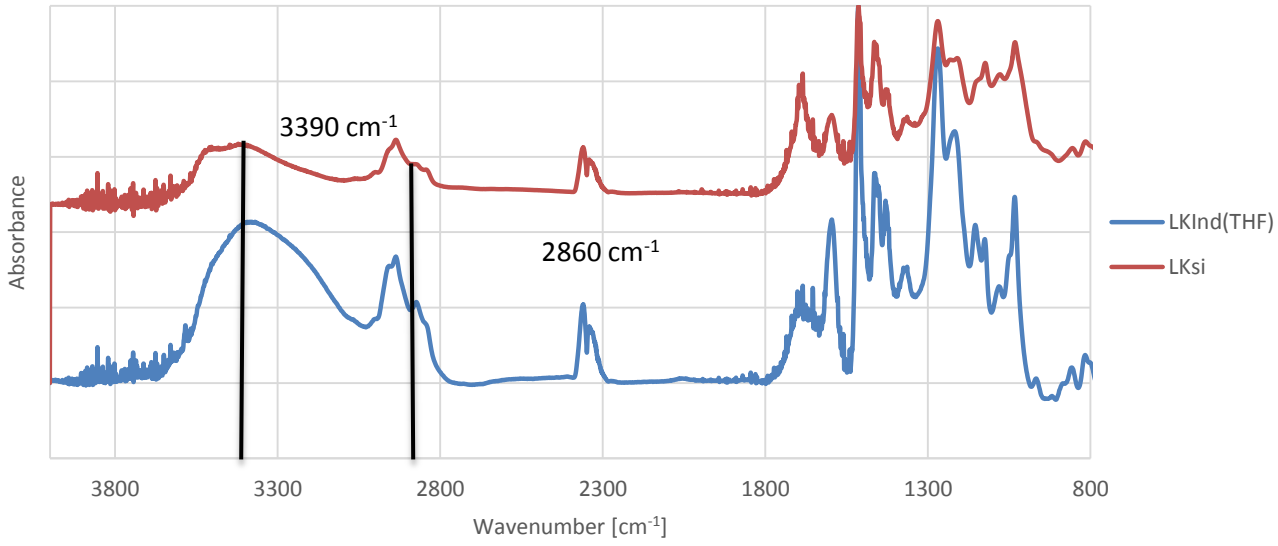

Figure 75 FTIR spectra of SLF and LKSi

Considering a magnification of the spectrum visible in **figure 76**, it was possible to notice other main differences between the two samples: the C=O stretching peak at 1690 cm^{-1} increased its intensity in LKSi spectrum, due to the formation of the urethane bond through the silanization reaction; also the 1360 cm^{-1} peak increased, which is ascribable to increasing of the –Me groups; at 856 cm^{-1} and 800 cm^{-1} differences were observed due to the –Si-O-C- and –Si-O-Si- bonds respectively , while at 1000 cm^{-1} an increase of the peak of stretching -Si-O- was observed.

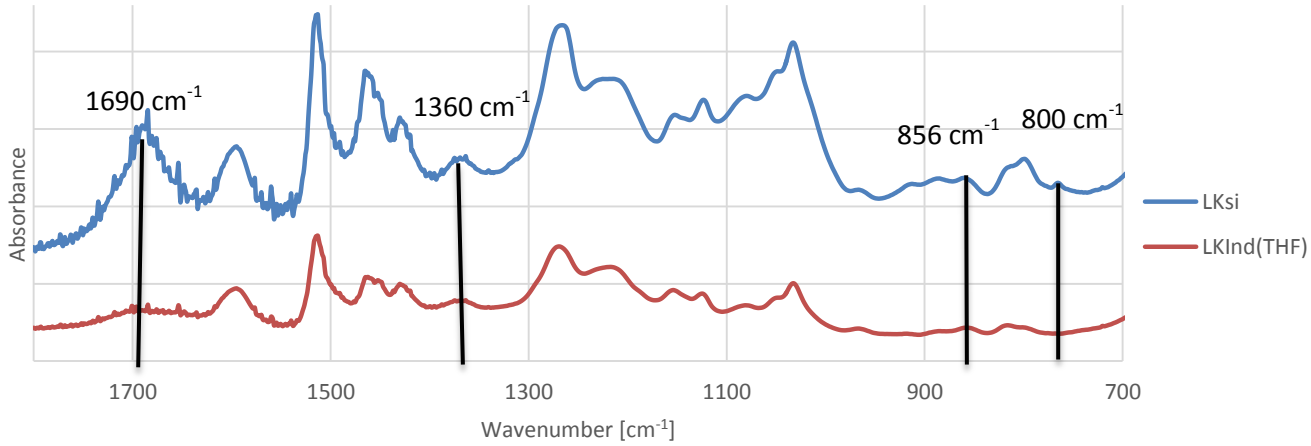

Figure 76 FTIR spectrum magnification of LKSi and SLF

FTIR spectrum of LKSI-TEOS system was also analyzed in **Figure 77** and compared to the LKSI. Differences in intensity absorption of the peaks ranged between 2800 and 3050 cm^{-1} were observed, due to the stretching of the OH; variations between 1170 and 1000 cm^{-1} were also noticed, ascribable to the increasing of the number of Si-C e Si-O bonds, due to the introduction of the TEOS.

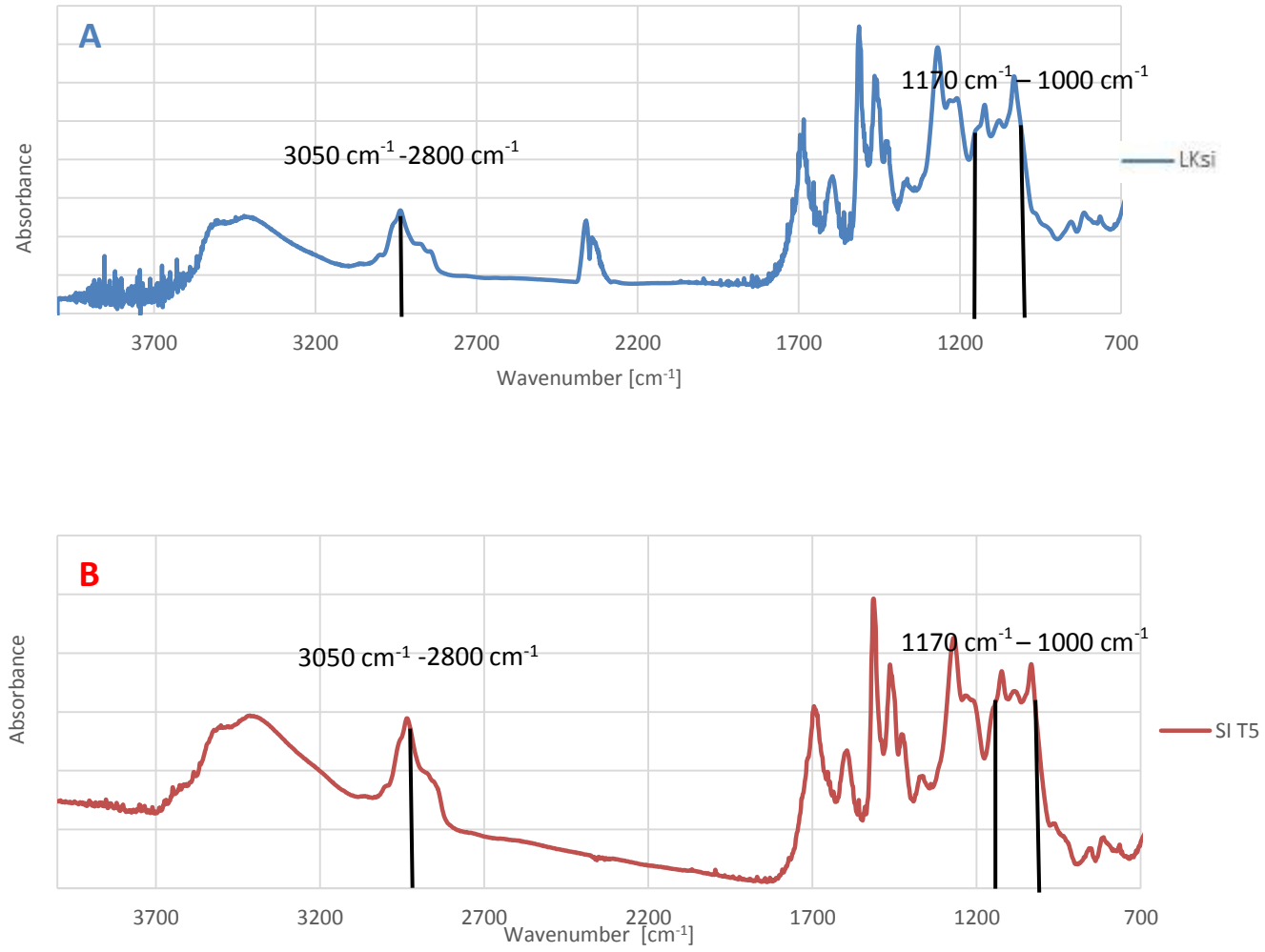

Figure 77 FTIR spectra of LKSi (A) and LKSi-TEOS (B)

3.2.2 Thermal Analysis

DSC measurements were performed on the four different samples, in order to determine their values of transition temperature.

Below in the **Table 17** the values of transition temperatures were reported. The introduction of Glycerol in different ratios to the lignin was responsible for the progressive decreasing of the Tg values of the samples: LKSi Tg decreased from 115°C in the formulation without Glycerol, down to 63°C for the formulation with 10% of plasticizer; LKSi-TEOS Tg instead, decreased from 110°C in the formulation without Glycerol, down to 48°C for the formulation with 10% of plasticizer. Due to the low ratio of TEOS to lignin, no significant increase in Tg could be observed; in other works (76), it was observed that starting from ratios of lignin/TEOS superior to 90/10, the Tg of the samples was higher than the simple LKSi.

SAMPLE NAME	T_g [°C]
[LKSi]	115
[LKSi]-GLY 5%	80
[LKSi]-GLY 10%	63
[LKSi-TEOS]	110
[LKSi-TEOS]-GLY 5%	79
[LKSi-TEOS]-GLY 10%	48

Table 17 DSC results for LKSi, LKSi-TEOS, and the corresponding systems with different glycerol content

DSC curves have been reported in **Figure 78** below, grouped according to the two different starting systems, LKSi and LKSi-TEOS.

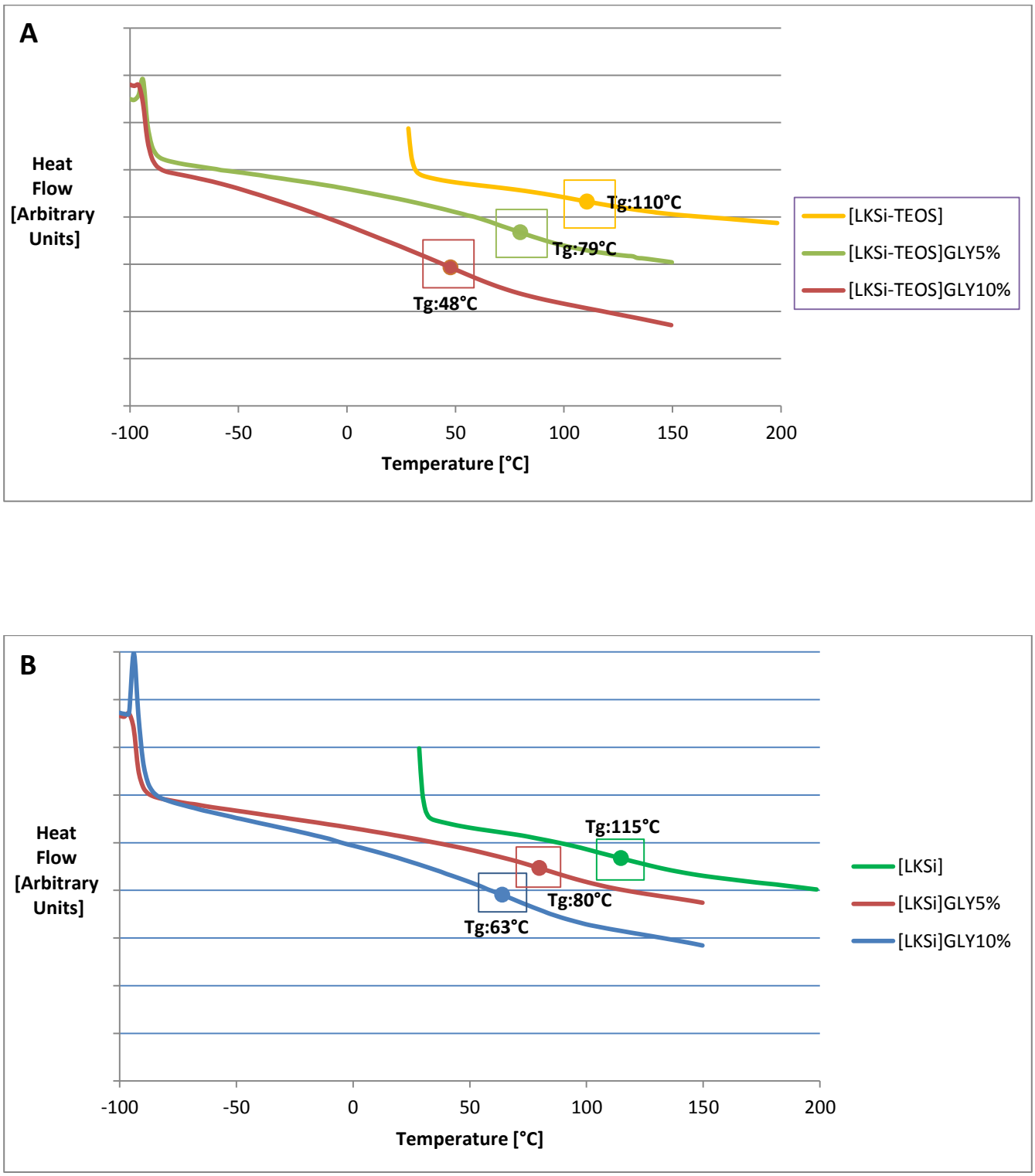

Figure 78 DSC curves of LKSi-TEOS(A) formulations with progressive increase of glycerol and LKSi (B) formulations with progressive increase of glycerol

3.2.3 Adhesion measurements

Adhesion measurements were executed on the four samples previously introduced. The solutions were spread by means of a spin coater on two different substrates, Q-Panels of Aluminum and Steel, at 1000 rpm for 80 seconds; average thickness obtained through this setup of deposition ranged from approximately 5 to 10 µm. In their formulations, Acetic Acid and water were included in order to increase the quantity of protons H^+ able to promote the reactions between the lignin's active sites and the metal oxides. Thermal treatment was performed in oven at 200°C for 15 minutes. For each sample, two different concentrations were tested: 0,5% and 20% of lignin with respect to the solvent (THF). A representative selection of these samples is visible in **Figure 79** below. Different colors correspond to different substrate-sample matchings: the dark brown samples correspond to solutions with the 20% of lignin concentration spread on steel substrates; the light brown are those with the 20% of lignin spread on aluminum substrates; the transparent ones are instead the solutions with the 0,5% of lignin spread on both steel and aluminum substrates.

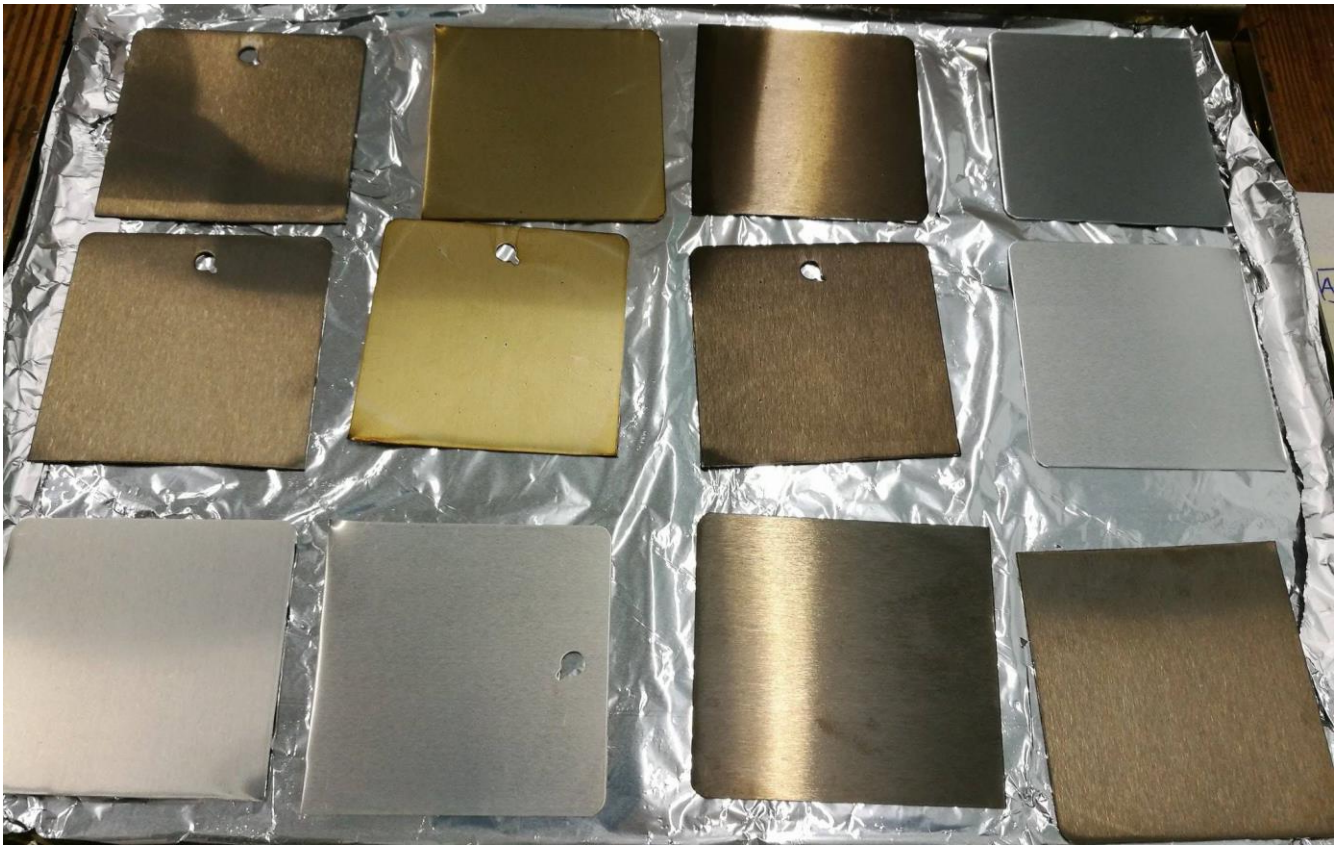

Figure 79 the four different systems spread on aluminum and steel substrates in order to execute pull-off adhesion measurements

Adhesion measurements of the solutions on the substrates were performed by means of a PosiTest AT-M Manual adhesion pull-off tester (DeFelsko); the measurement consisted in evaluating the pulling force necessary to detach a 20 mm-diameter aluminum dolly adhered to the coatings by means of epoxy adhesive (Araldite 2011, curing cycle: 100 °C, 12 h). Below in **Table 18** the values of these measurements were reported, expressed in MPa and compared to the reference values of the substrates without the coatings, simply cleaned through an ultrasonic bath of two hours in Isopropyl alcohol solvent followed by plasma treatment and tested through the adhesion of the epoxy adhesive directly on their surfaces. Two different trends can be noticed in the behavior of the systems. While the solutions with higher lignin concentrations showed values of adhesion not particularly elevated, all around 1– 1.5 MPa, those with lower lignin concentrations instead exhibited values of adhesion of about 2-4 MPa, with both aluminum and steel substrates. This could be justified by the fact that in the higher concentrations of lignin, the H^+ tended to disperse inside the bulk of the solution, driving the lignin to polymerize with itself rather than interacting with the substrates; instead the lower amount of solution in the 0,5% lignin/solvent ratios allowed the active sites of the lignin to better interact with the substrates, promoting the formation of LKSi-surface aluminum bonds.

SAMPLE NAME	ADHESION ON ALUMINUM [MPa]	ADHESION ON STEEL [MPa]
Epoxy adhesive	3.7±0.8	4.97±0.6
[LKSi]20%	1.06±0.2	1.63±0.5
[LKSi]0,5%	3.27±0.1	2.61±0.3
[LKSi-TEOS]20%	1.25±0.3	1.11±0.2
[LKSi-TEOS]0,5%	2.74±0.3	3.72±0.7
[LKSi]20%+GLY10%	1.14±0.1	1.02±0.1
[LKSi]0,5%+GLY10%	2.70±0.5	3.55±0.1
[LKSi-TEOS]20%+GLY10%	1.11±0.1	1.75±0.1
[LKSi-TEOS]0,5%+GLY10%	3.46±0.3	3.32±0.5

Table 18 Pull-off values for the different coating-substrate matchings

3.2.4 Corrosion measurements

Corrosion test was performed by means of a potentiostat-galvanostat model 273A. The operative conditions applied during the test established a scan rate of 5 mV/s from 0,5V vs Open Circuit Potential to +0,5V. The formulations were spread on both aluminum and steel substrates by means of a spin coater at 1000 rpm for 80 seconds. Thermal treatment to reach the crosslinking reaction was executed in oven at 200°C for 15 minutes. The corrosion resistance was evaluated through the measurement of the limiting current density value $\boldsymbol{j_{corr}^{lim}}\ [\frac{\boldsymbol{A}}{\boldsymbol{cm^2}}]$, which corresponds to the intersection between the tangents of the anodic and the cathodic curves. The lower the value of $\boldsymbol{j_{corr}^{lim}}$ obtained, the higher is the potential value of the systems, which means that the samples show a better resistance to corrosion. For both the substrates, an aluminum and a steel sample with no deposited coatings were taken as reference systems. The treatment they underwent, which was the same also for the coated samples, consisted of a cleaning in an ultrasonic bath for two hours in Isopropyl alcohol solvent followed by air plasma treatment.

- COATINGS ON ALUMINUM SUBSTRATES

The results of the test for coatings on aluminum substrates are reported below; they have been divided in four major groups:

1. Formulations containing [LKSi] at two different concentrations in solution with THF, 20% and 0,5%. The results visible in **Figure 80** showed a $\boldsymbol{j_{corr}^{lim}}$ for the [LKSi]20% of 6,8E-9 A/cm^2; instead the [LKSi]0,5% exhibited a $\boldsymbol{j_{corr}^{lim}}$= 5,6E-8 A/cm^2; for this reason [LKSi]0,5% resulted less protective than the [LKSi]20%, but in any case its corrosion resistance appeared to be still better than the one of the aluminum substrate, which was equal to 8,2E-8 A/cm^2.

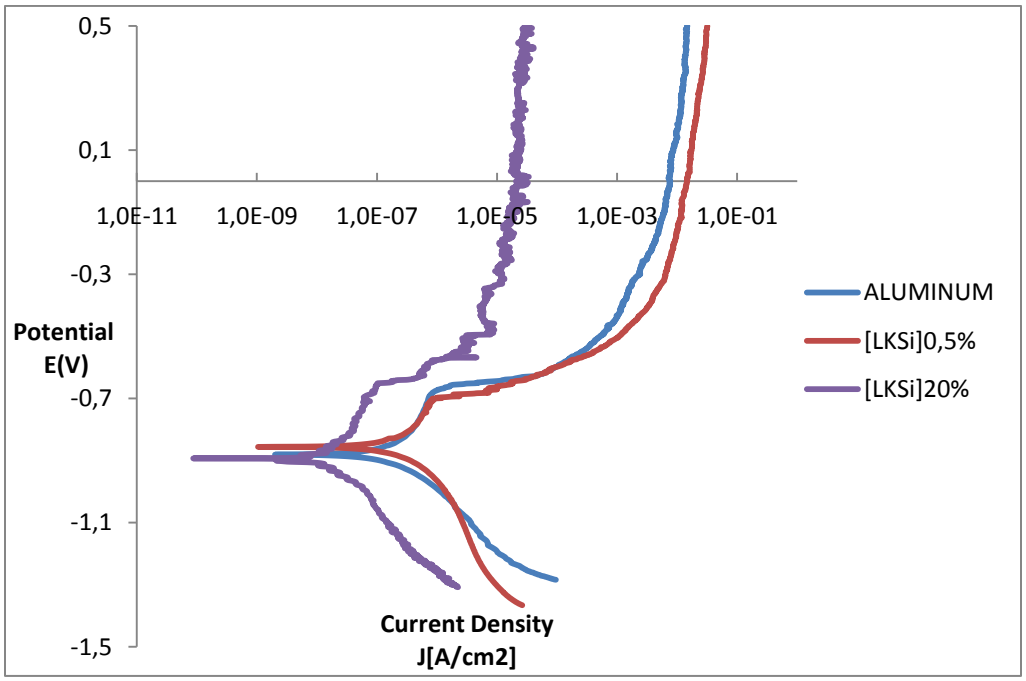

Figure 80 Potentiodynamic test results for LKSi formulations on aluminum substrate

In **Table 19** below are resumed the values obtained for the three samples above mentioned and visible in **Figure 80**.

SAMPLE	LIMITING CURRENT DENSITY J[A/cm^2]
ALUMINUM	8,20E-08
[LKSi]0,5%	5,60E-08
[LKSi]20%	6,80E-09

Table 19: summary of the values obtained for the LKSi values compared with the aluminum substrate

2. Formulations containing [LKSi-TEOS], at two different concentrations of LKSi in solution with THF, 20% and 0,5%. The results visible in **Figure 81** showed comparable values of j_{corr}^{lim} for [LKSi-TEOS]20% which was equal to 2,9E-09 A/cm^2 and for [LKSi-TEOS]0,5% that resulted equal to 9,6E-10 A/cm^2. Both of them showed lower values than the uncoated aluminum substrate.

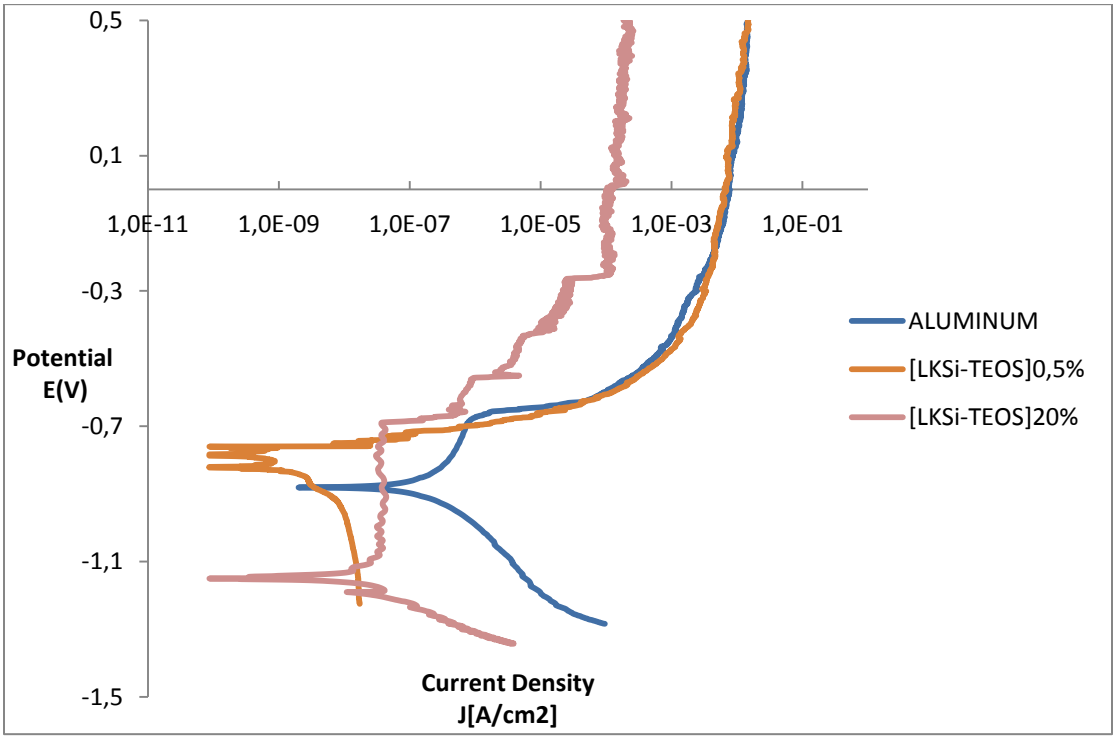

Figure 81 Potentiodynamic test results for LKSi-TEOS formulations on aluminum substrate

In **Table 20** below are resumed the values obtained for the three samples above mentioned and visible in **Figure 81.**

SAMPLE	LIMITING CURRENT DENSITY J[A/cm2]
ALUMINUM	8,20E-08
[LKSi-TEOS]0,5%	9,60E-10
[LKSi-TEOS]20%	2,90E-09

Table 20 summary of the values obtained for the LKSi-TEOS values compared with the aluminum substrate

3. Formulations containing [LKSi]+GLYCEROL at two different concentrations of LKSi in solution with THF, 20% and 0,5%. The results visible in **Figure 82** showed a j_{corr}^{lim} for the [LKSi]20%+GLY of 1,40E-08 A/cm^2,slightly lower than the value found for the uncoated aluminum substrate; instead the [LKSi]0,5%+GLY exhibited a j_{corr}^{lim}= 6,50E-08 A/cm^2; for this reason [LKSi]0,5%+GLY resulted not as resistant to corrosion as the other formulations.

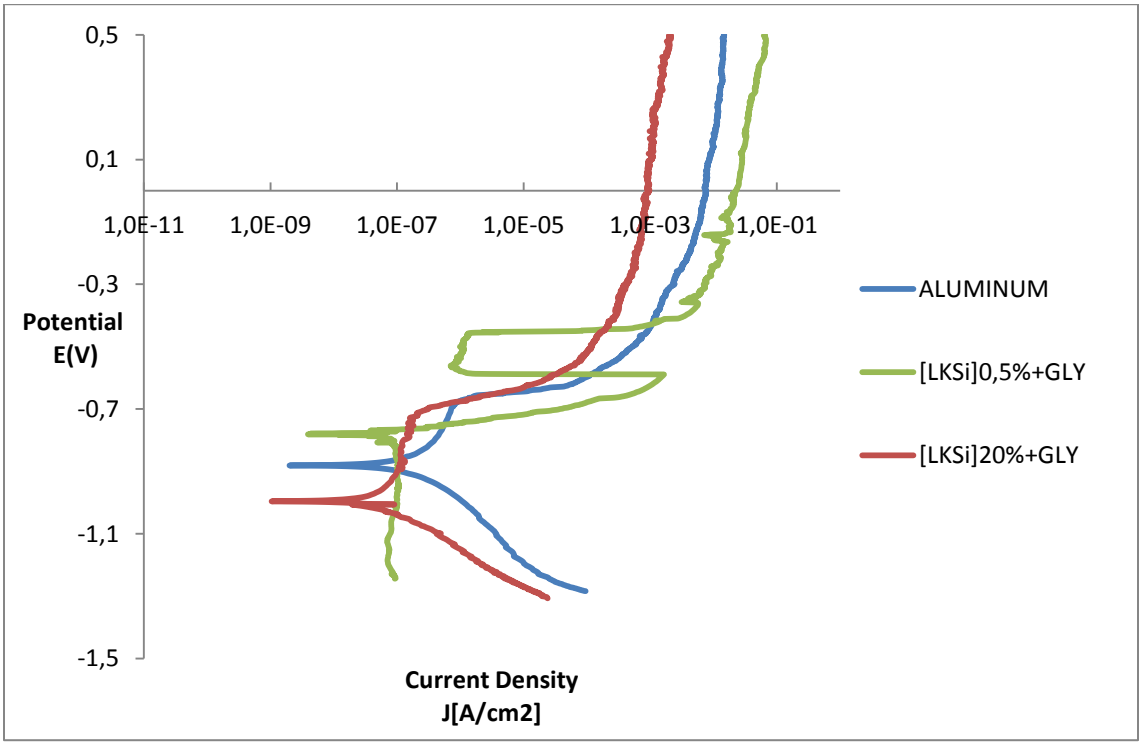

Figure 82 Potentiodynamic test results for [LKSi]+GLY formulations with glycerol on aluminum substrate

In **Table 21** below are resumed the values obtained for the three samples above mentioned and visible in **Figure 82.**

SAMPLE	LIMITING CURRENT DENSITY J[A/cm2]
ALUMINUM	8,20E-08
[LKSi]0,5%+GLY	6,50E-08
[LKSi]20%+GLY	1,40E-08

Table 21 summary of the values obtained for the [LKSi]+GLY values compared with the aluminum substrate

4. Formulations containing [LKSi-TEOS]+Glycerol at two different concentrations of LKSi in solution with THF, 20% and 0,5%. The results visible in **Figure 83** showed a j_{corr}^{lim} for the [LKSi-TEOS]20%+GLY of 1,70E-09 A/cm^2, and for the [LKSi-TEOS]0,5%+GLY of 3,40E-09 A/cm^2, both significantly lower than the value found for the uncoated aluminum substrate.

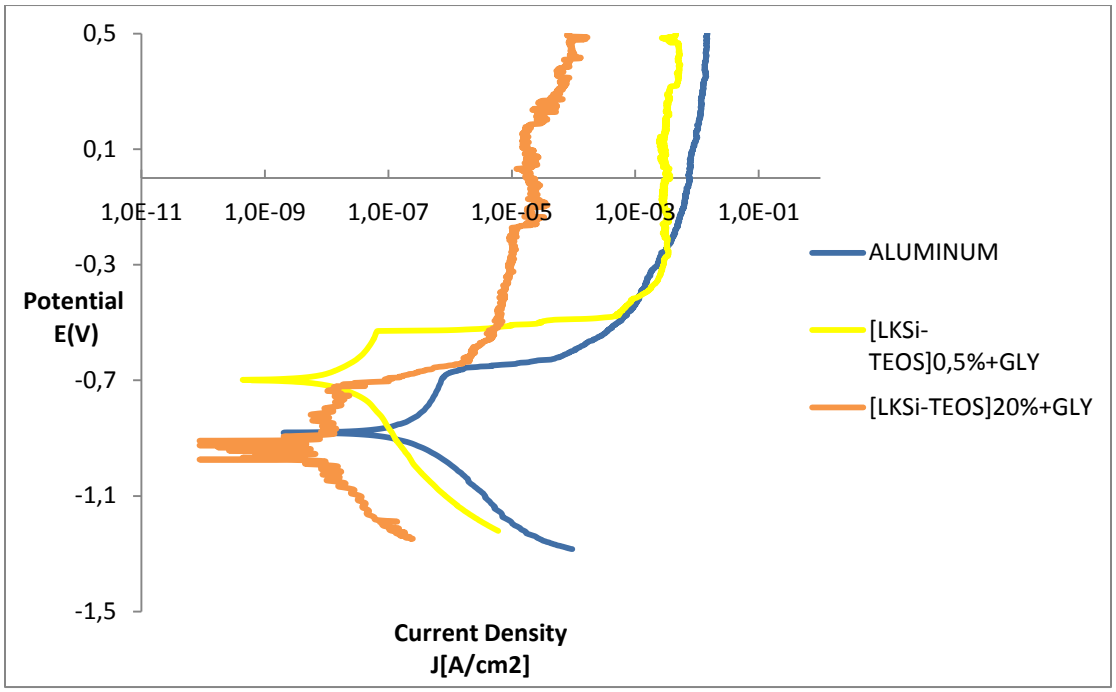

Figure 83 Potentiodynamic test results for [LKSi-TEOS]+GLY formulations with glycerol on aluminum substrate

In **Table 22** below are resumed the values obtained for the three samples above mentioned and visible in **Figure 83.**

SAMPLE	LIMITING CURRENT DENSITY J[A/cm2]
ALUMINUM	8,20E-08
[LKSi-TEOS]0,5%+GLY	3,40E-09
[LKSi-TEOS]20%+GLY	1,70E-09

Table 22 summary of the values obtained for the [LKSi-TEOS]+GLY values compared with the aluminum substrate

Making a comparison between all the formulations, it was possible to notice that the samples containing the higher concentrations of LKSi gave the lowest values of limiting current density, as a further proof of the antioxidant properties possessed by lignin; in particular, the formulations containing TEOS reached the lowest j_{corr}^{lim} among all, suggesting their possible application as anticorrosive coatings for aluminum substrates. A complete summary of the values obtained for the formulations spread on aluminum substrates is visible in **Table 23** below.

SAMPLE	LIMITING CURRENT DENSITY J[A/cm2]
ALUMINUM	8,20E-08
[LKSi]0,5%	5,60E-08
[LKSi]20%	6,80E-09
[LKSi-TEOS]0,5%	9,60E-10
[LKSi-TEOS]20%	2,90E-09
[LKSi]0,5%+GLY	6,50E-08
[LKSi]20%+GLY	1,40E-08
[LKSi-TEOS]0,5%+GLY	3,40E-09
[LKSi-TEOS]20%+GLY	1,70E-09

Table 23 summary of the values obtained for all the formulations spread on aluminum substrates

- COATINGS ON STEEL SUBSTRATES

The results of the test for coatings on steel substrates are reported below; they have been divided in four major groups:

1. Formulations containing [LKSi] at two different concentrations in solution with THF, 20% and 0,5%. The results visible in **Figure 84** showed a j_{corr}^{lim} for the [LKSi]20% of 3,7E-9 A/cm^2; instead the [LKSi]0,5% exhibited a j_{corr}^{lim}= 3,0E-7 A/cm^2; for this reason [LKSi]0,5% resulted less protective than the [LKSi]20%, but in any case its corrosion resistance appeared to be comparable to the one of the steel substrate, which was equal to 2,8E-7 A/cm^2.

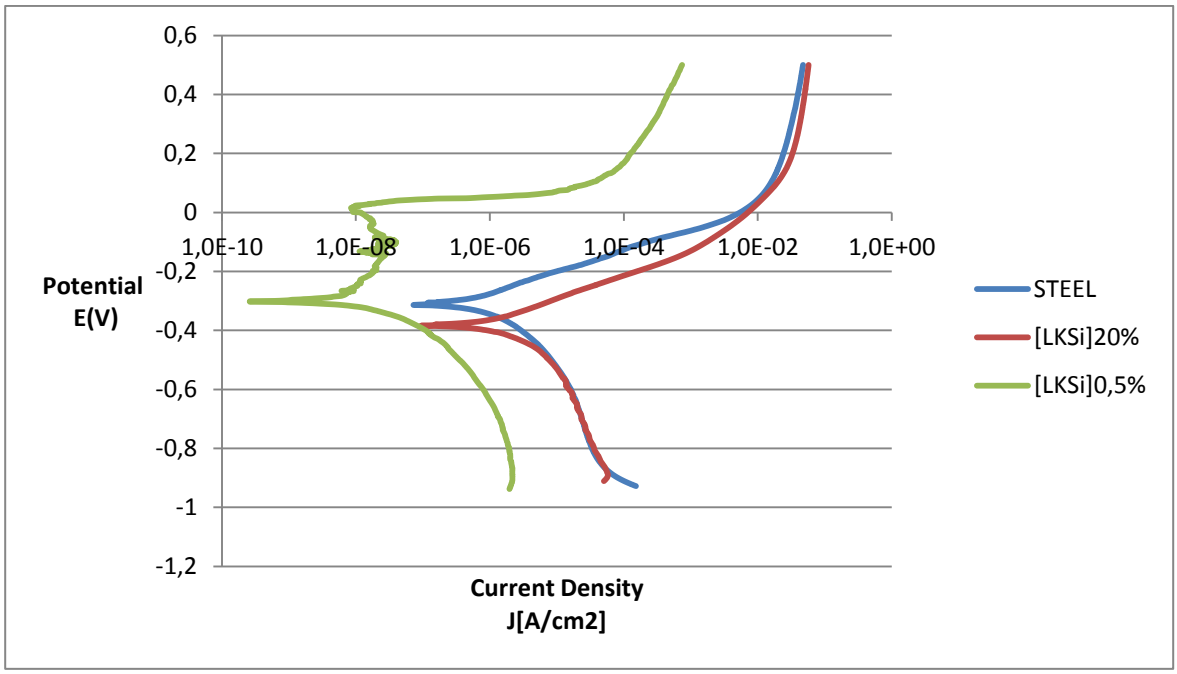

Figure 84 Potentiodynamic test results for LKSi formulations on steel substrate

In **Table 24** below are resumed the values obtained for the three samples above mentioned and visible in **Figure 84.**

SAMPLE	LIMITING CURRENT DENSITY J[A/cm2]
STEEL	2,80E-07
[LKSi]20%	3,70E-09
[LKSi]0,5%	3,00E-07

Table 24 summary of the values obtained for the [LKSi] values compared with the steel substrate

2. Formulations containing [LKSi-TEOS], at two different concentrations of LKSi in solution with THF, 20% and 0,5%. The results visible in **Figure 85** showed comparable values of j_{corr}^{lim} for [LKSi-TEOS]20% which was equal to 3,1E-7 A/cm^2 and for [LKSi-TEOS]0,5% that resulted equal to 2,9E-7 A/cm^2. Both of them showed almost the same corrosion resistance of the uncoated steel substrate.

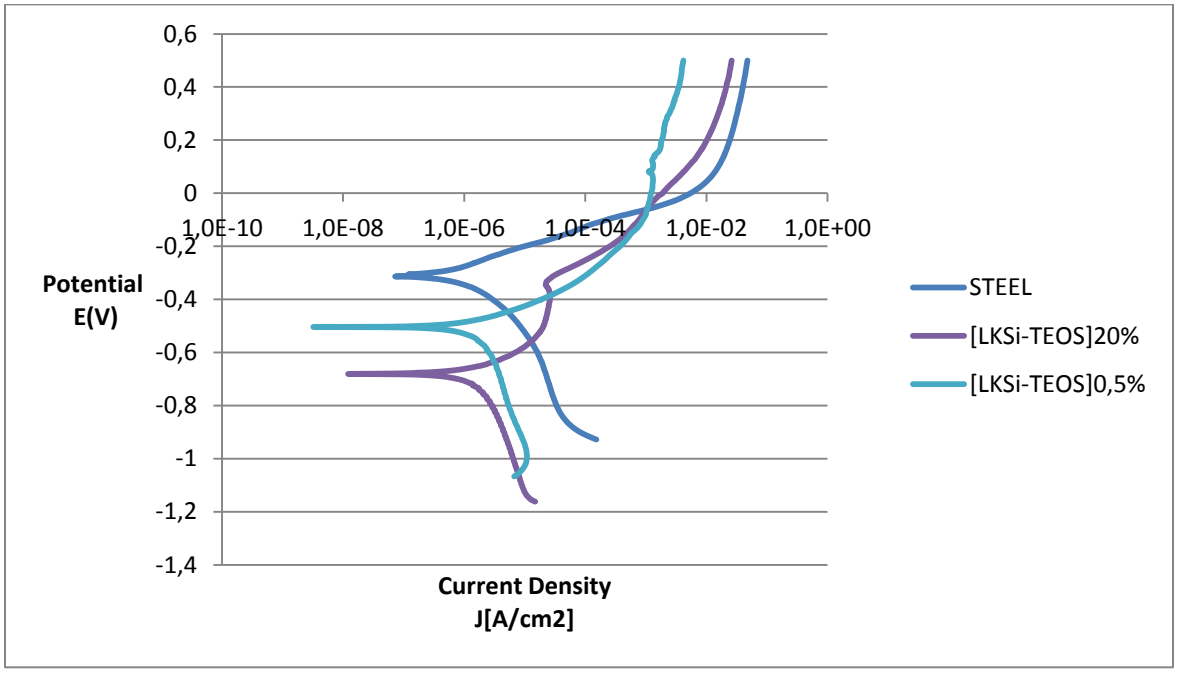

Figure 85 Potentiodynamic test results for LKSi-TEOS formulations on steel substrate

In **Table 25** below are resumed the values obtained for the three samples above mentioned and visible in **Figure 85.**

SAMPLE	LIMITING CURRENT DENSITY J[A/cm2]
STEEL	2,80E-07
[LKSi-TEOS]0,5%	2,90E-07
[LKSi-TEOS]20%	3,10E-07

Table 25 summary of the values obtained for the [LKSi-TEOS] values compared with the steel substrate

3. Formulations containing [LKSi]+GLYCEROL at two different concentrations of LKSi in solution with THF, 20% and 0,5%. The results visible in **Figure 86** showed a j_{corr}^{lim} for the [LKSi]20%+GLY of 1,70E-07 A/cm^2, lower than the value found for the uncoated steel substrate; instead the [LKSi]0,5%+GLY exhibited a j_{corr}^{lim}= 7,50E-07 A/cm^2; for this reason [LKSi]0,5%+GLY resulted not as resistant to corrosion as the other formulations.

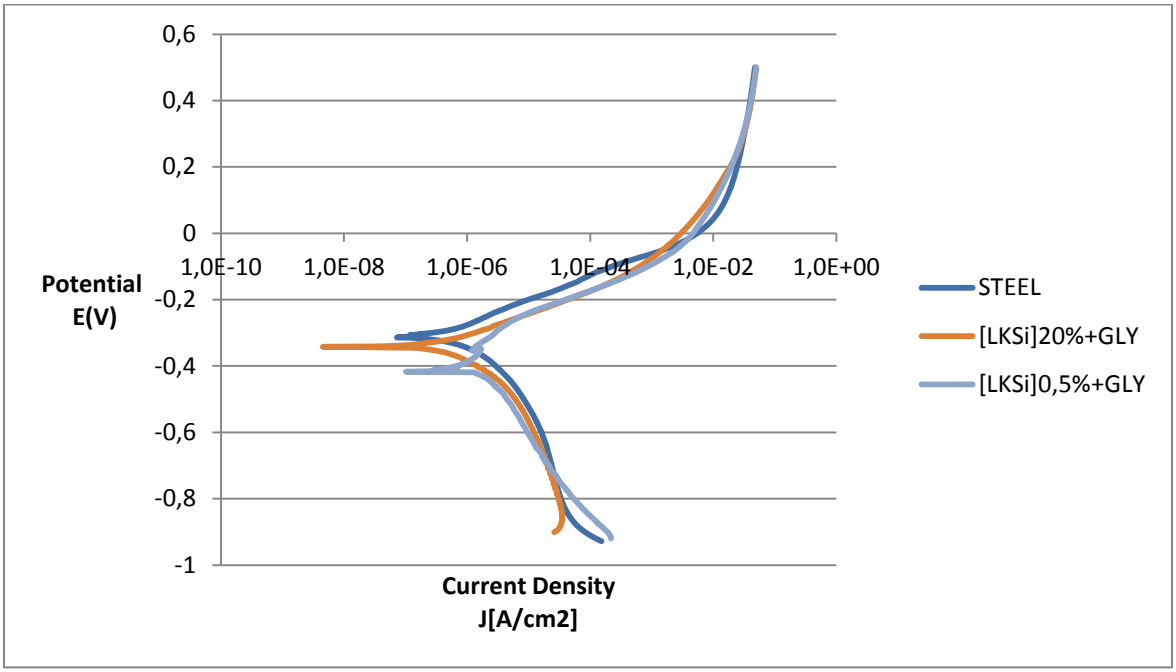

Figure 86 Potentiodynamic test results for [LKSi]+GLY formulations on steel substrate

In **Table 26** below are resumed the values obtained for the three samples above mentioned and visible in **Figure 86.**

SAMPLE	LIMITING CURRENT DENSITY J[A/cm2]
STEEL	2,80E-07
[LKSi]0,5%+GLY	7,50E-07
[LKSi]20%+GLY	1,70E-07

Table 26 summary of the values obtained for the [LKSi]+GLY values compared with the steel substrate

4. Formulations containing [LKSi-TEOS]+Glycerol at two different concentrations of LKSi in solution with THF, 20% and 0,5%. The results visible in **Figure 87** showed a j_{corr}^{lim} for the [LKSi-TEOS]20%+GLY of 3,30E-08 A/cm^2, significantly lower than the value found for the uncoated aluminum substrate, and for the [LKSi-TEOS]0,5%+GLY a value of 1,70E-06 A/cm^2, which resulted not as resistant to corrosion as the other formulations.

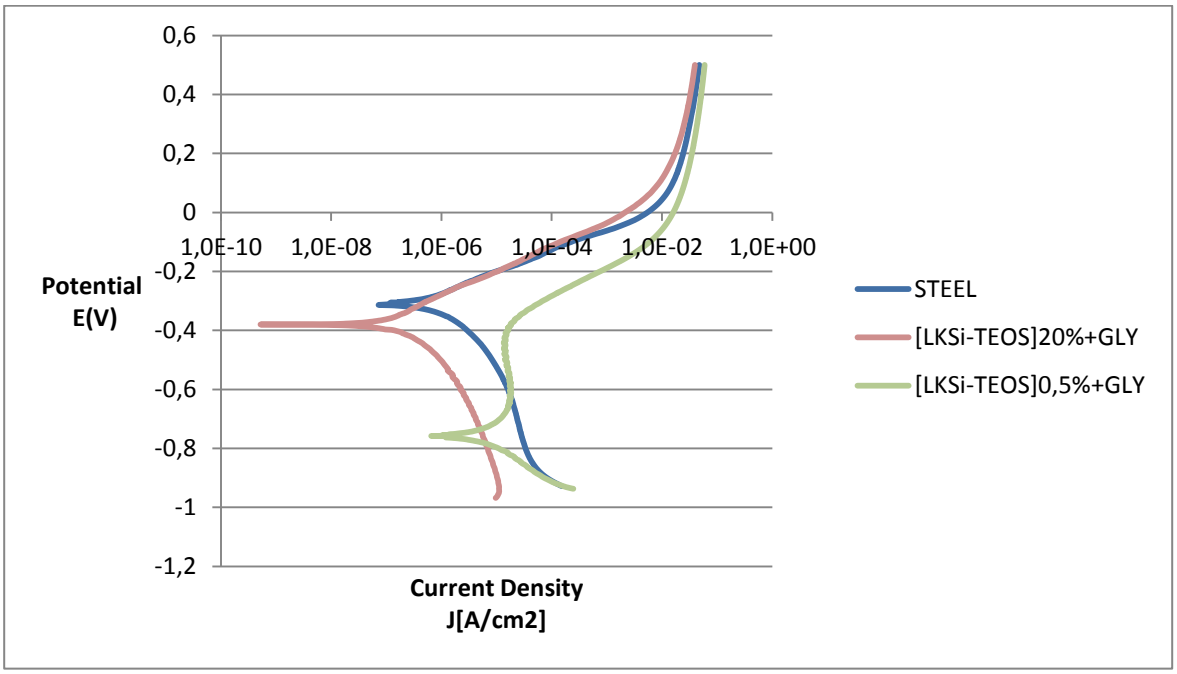

Figure 87 Potentiodynamic test results for [LKSi-TEOS]+GLY formulations on steel substrate

In **Table 27** below are resumed the values obtained for the three samples above mentioned and visible in **Figure 87.**

SAMPLE	LIMITING CURRENT DENSITY J[A/cm2]
STEEL	2,80E-07
[LKSi-TEOS]0,5%+GLY	1,70E-06
[LKSi-TEOS]20%+GLY	3,30E-08

Table 27 summary of the values obtained for the [LKSi-TEOS]+GLY values compared with the steel substrate

Making a comparison between all the formulations, it was possible to notice that three samples gave the significant low values of limiting current density, while the others were comparable to the behavior of the uncoated steel substrate, showing a similar corrosion resistance. A complete summary of the values obtained for the formulations spread on steel substrates is visible in **Table 28** below.

SAMPLE	LIMITING CURRENT DENSITY J[A/cm2]
STEEL	2,80E-07
[LKSi]0,5%	3,70E-09
[LKSi]20%	3,00E-07
[LKSi-TEOS]0,5%	2,90E-07
[LKSi-TEOS]20%	3,10E-07
[LKSi]0,5%+GLY	7,50E-07
[LKSi]20%+GLY	1,70E-07
[LKSi-TEOS]0,5%+GLY	1,70E-06
[LKSi-TEOS]20%+GLY	3,30E-08

Table 28 summary of the values obtained for all the formulations spread on steel substrates

3.2.5 Bending test

To evaluate the effect of the introduction of Glycerol in the formulations with LKSi and LKSi-TEOS, bending test was made on the four systems at different concentrations. Being glycerol a plasticizer and also according to the results obtained from Differential Scanning Calorimetry measurements, its introduction in the formulations reduced the transition temperatures of the samples; this helped them to improve their plastic behavior and turned this films into suitable coatings to be applied on metallic substrates subjected to coil coating processes. According to the EN ISO 17132:2007 International Standard, multiples of 180° bends of the coated metal are made, and the amount of cracking produced at each bend is visually determined. The results are classified as 0T, 1T, 2T etc. The 0T bend consists of making a 180° bend with the paint kept on the outside of the bend and pressing the bend flat so that there is no space between the metal surfaces. This operation is repeated successively to produce a 1T, 2T,3T, etc. These successive bends result in two, three, etc. thickness of the metal around the first bend. It results evident that the greater the number of thickness around which the coated metal is bent, the less severe the test. An example of the test procedure is visible below in **Figure 88.**

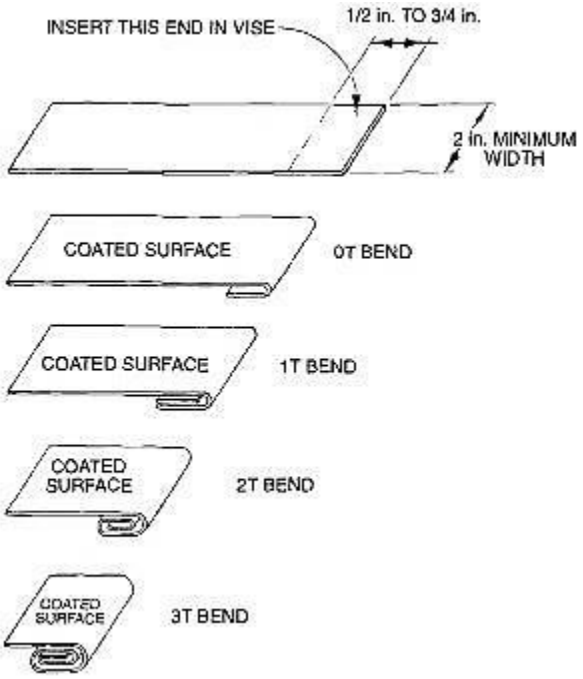

Figure 88 T-bend test in which the coated specimen is bent around itself (77)

The test was carried out folding triangular samples of coatings realized on aluminum substrates, at progressively decreasing angles, by mean of a manual bender. The chosen coatings were the ones with a concentration of lignin of 20%, in order to be able to see easily the modification of the film on the bended substrate, that is:

- [LKSi] 20%
- [LKSi-TEOS]20%
- [LKSi]20%+GLYCEROL 10%
- [LKSi-TEOS]20%+GLYCEROL 10%

The bending procedures of some of the samples are visible in **Figure 89**.

Figure 89 images of bending test procedures; fixing the sample(A), folding the sample(B), adjusting the bended piece (C).

At each folding, the 180° angle obtained as the first one and named T0 became smaller at each turn, and the following foldings were named with increasing numbers in the wording “XT”. The results obtained from the test, visible in **Figure 90,** have been presented taking into account the half angles of each folding instead of the units, since those angles allowed to better see the behavior of the coated samples. It was possible to identify two different behaviors of the samples: while the films not containing glycerol showed the breaking of the coating at high folding angles like 0T and 0,5T up to 2,5T, and maintained their integrity only at lower bending angles like 3,5T, instead both the coatings containing glycerol were able to resist at the mechanical processing starting from angle corresponding to 2,5T. Although the testing procedures and the available equipment weren’t quite accurate and suitable for an appropriate evaluation of the coating resistance to the mechanical processing of the substrates, it was anyway possible to found out a trend in the behavior of the samples that justified the plasticizing effect given by the introduction of glycerol in the coatings: thanks to the decrease of the glass transition temperature of the coatings with glycerol, their response to the deformation became less fragile and made them suitable for application on substrates subjected to coil coating processes.

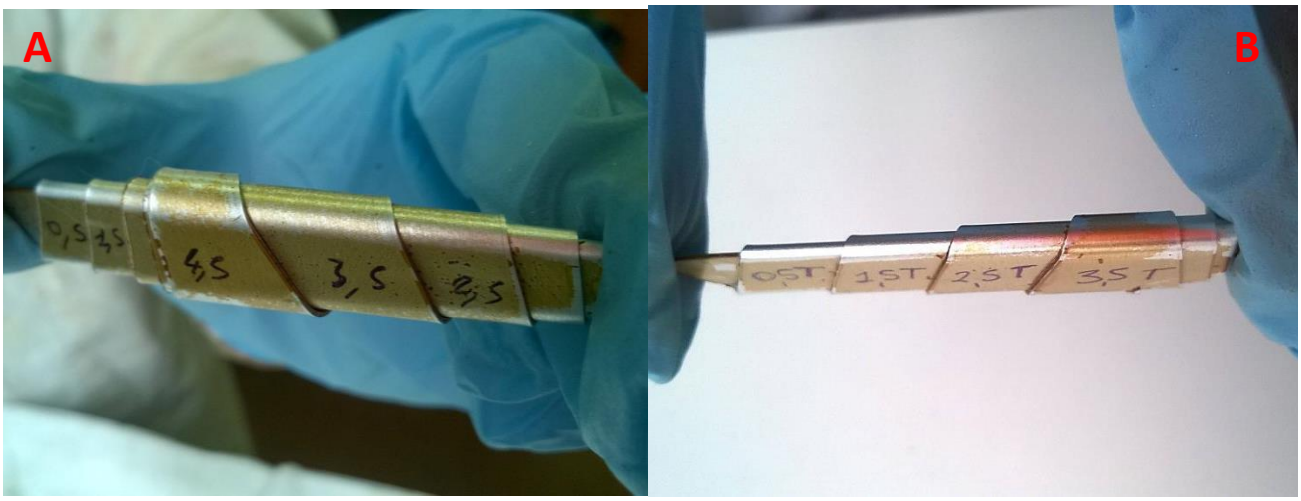

Figure 90 images of coatings with glycerol (A) and without glycerol (B)

3.3 Lignin-based crosslinked matrices for composite materials

From the results obtained in previous paragraphs, it was proved that lignin could be transformed, through specific functionalizations, into a crosslinked material for several applications. In the last part of the chapter, then, a brief introduction to another different application of this polymer will be discussed, which falls within bio-based polymer matrix composites. From literature it is known that bio-based components have already been utilized in composites for several applications like roofing and structural (78) or impact stressed components (79), and have mainly been employed as lignocellulosic fibers; this suggests that a proper functionalization of lignin could lead to its utilization in the field of composite materials. The experimental research discussed in this part of the work has been focused on the realization of lignin-based matrices for composite materials, in an effort to obtain crosslinked systems to characterize and compare with the well-known crosslinked matrices available to industry.

Two composite systems were realized and compared:

- A standard one, based on a matrix made of Saduren/Acronal [30%/70%] solution in different concentrations in the solvent, which consisted of distilled water.

- An experimental one, based on a matrix made of Indulin dissolved in distilled water with the addition of the Primid crosslinker in a ratio of 10% to the lignin, and of the PTSA catalyst 1% with respect to the dry content. Being lignin insoluble in neutral water (pH7), it was necessary to increase the pH of the solution by means of Ammonium Hydroxide. Also This system was realized at different concentrations of solute in water solvent, in order to increase progressively the add-on of dry content of matrix in the composite material.

Both these systems were obtained by fibers impregnation inside bechers containing the two solutions. After the immersion, the impregnated carbon fibers were pressed inside rollers for the same number of times. The non woven carbon fibers had an areal weight of 20 g/m^2 and were cut in rectangles of 3x4 cm^2 and impregnated of the solutions previously described. Both the samples were thermally treated in oven at 210°C for about 10 minutes, in order to achieve the crosslinking reaction of the matrix. Below in **Figure 91** some examples of the composite systems are shown. On the left, the composite with a browner color contains the lignin-based matrix; the darker composite on the right instead contains a matrix made of Saduren/Acronal mixture. The systems were characterized through

Scanning Electron Microscopy and Dynamic Modulus Analysis to obtain information about the sample surface topography, the wettability of the fibers and the elastic modulus.

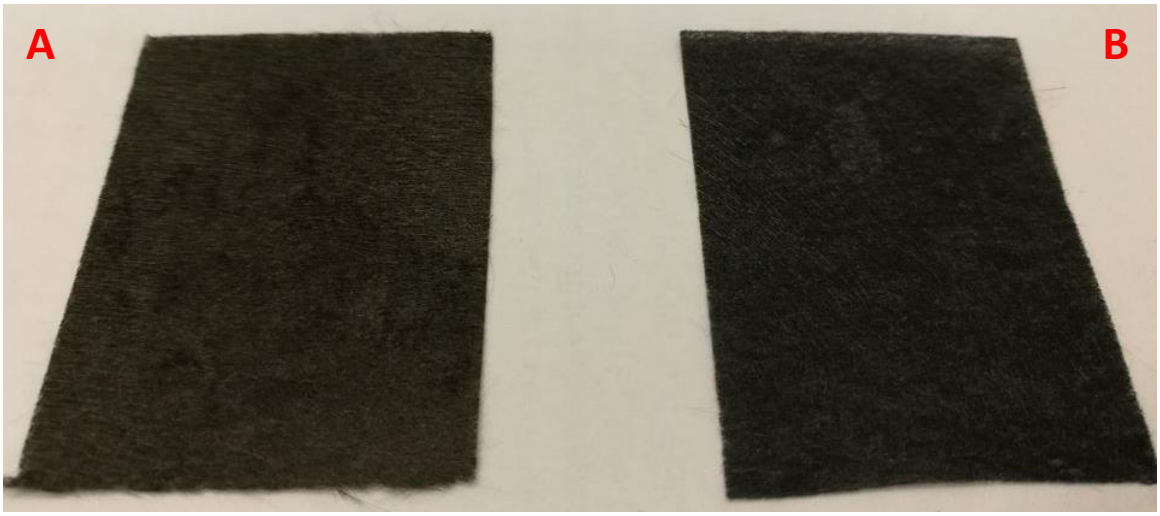

Figure 91 image of IND-PR (A) and SAD-ACR (B)

3.3.1 Dynamic Mechanical Analysis

It was carried out by means of a Mettler DMA/SDTA 861E equipment, in tension mode at a temperature of 25°C and a frequency of 1 Hz and deformation range between 0,1 and 100µm. Below in **Table 29** the values of Modulus as a function of displacement for all the different samples were reported. It was possible to notice that increasing the matrix content in the composite led both the systems to increase the value of the measured Modulus: ranging from 10% to 60%, the stiffness of the composite materials sharply increased. In **Table 29** it is possible also to notice that the systems named IND-PRI, i.e containing lignin, were less in number with respect to the SAD-ACR: this choice derived from the necessity to compare only systems with the same percentage of dry content included in the matrix, and was also limited by the equipment in possess, that allowed to obtain several different percentages of SAD-ACR matrices since they required less precise impregnation techniques, unlike the IND-PR.

SAMPLE NAME	CARBON FIBERS AREA [cm^2]	EFFECTIVE ADD-ON	MODULUS [MPa]
Sad-Acr [10%]	12	20%	1420
Sad-Acr [20%]	12	30%	2115
Sad-Acr [30%]	12	50%	2129
Sad-Acr [40%]	12	70%	2200
Sad-Acr [60%]	12	100%	2437
Ind-Pr [10%]	12	20%	1450
Ind-Pr [20%]	12	50%	1499
Ind-Pr [40%]	12	100%	2501

Table 29 DMA curves of the two composite systems at different dry content of matrix

The trend found in the measurements confirmed that lignin possesses properties able to compete with typical industrial matrices like the SAD-ACR system, reaching with the sample containing 40% of add on the modulus value of 2,5 GPa. Considering the thickness of the samples, the utilization of non woven fibers with random orientation distribution, and also the limitations implied by the inadequate support for fiber impregnation, the obtained results could be considered highly satisfactory, also comparing them to values of non woven crosslinked matrix composites present in literature (80), (81).

3.3.2 Scanning Electron Microscopy analysis

By mean of a focused beam of electrons, SEM images of the two systems were produced and compared. Only the lower and the higher percentages of the two systems were analyzed and compared, i.e. the SAD-ACR 10%,the SAD-ACR 60%, the IND-PR 10% and the IND-PR 40%. This analysis was performed in order to investigate the morphology of the samples and the wettability of the carbon fibers, and the instrument used was a Carl Zeiss EVO 50 Extended Pressure, set at an accelerating voltage of 5 keV. In **Figure 92** below images of SAD-ACR 10% and IND-PR 10% at two different magnification levels (300X and 600X) are shown.

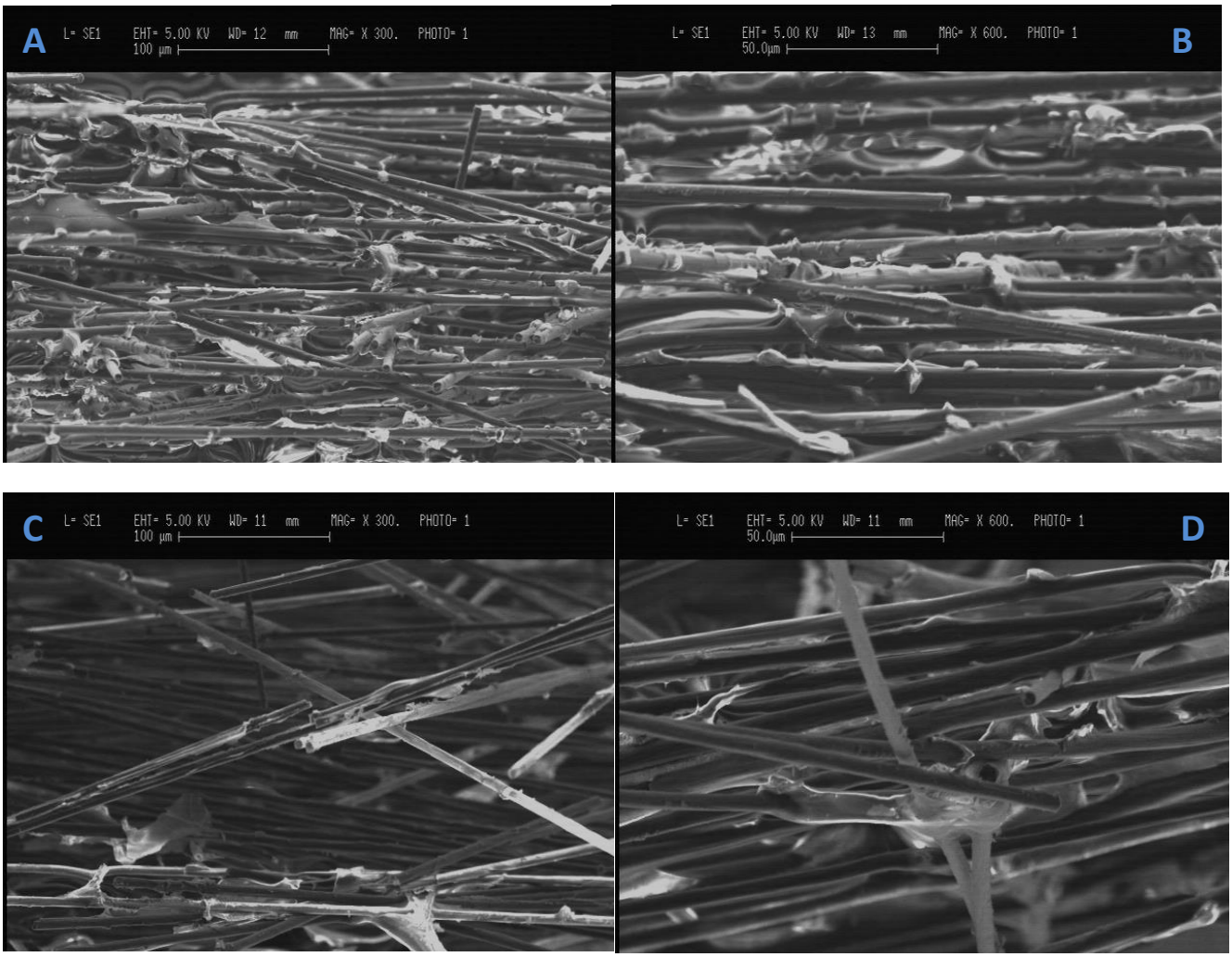

Figure 92 SEM images of: IND-PR 10% at 300X (A), and 600X(B); SAD-ACR 10% at 300X(C) and 600X(D)

Figure 92 showed that although both systems weren't able to perfectly wet the carbon fibers and neither to distribute themselves homogeneously in the sample, anyway the IND-PR samples seemed much more present in the composite network. Also taking a look at **Figure 93** below, it was possible to notice that lignin was able to create a more compact network with respect to the commercial matrix, so that just with a 40% of concentration of lignin in solution it was possible to obtain a pick-up of 60% of matrix content in the composite.

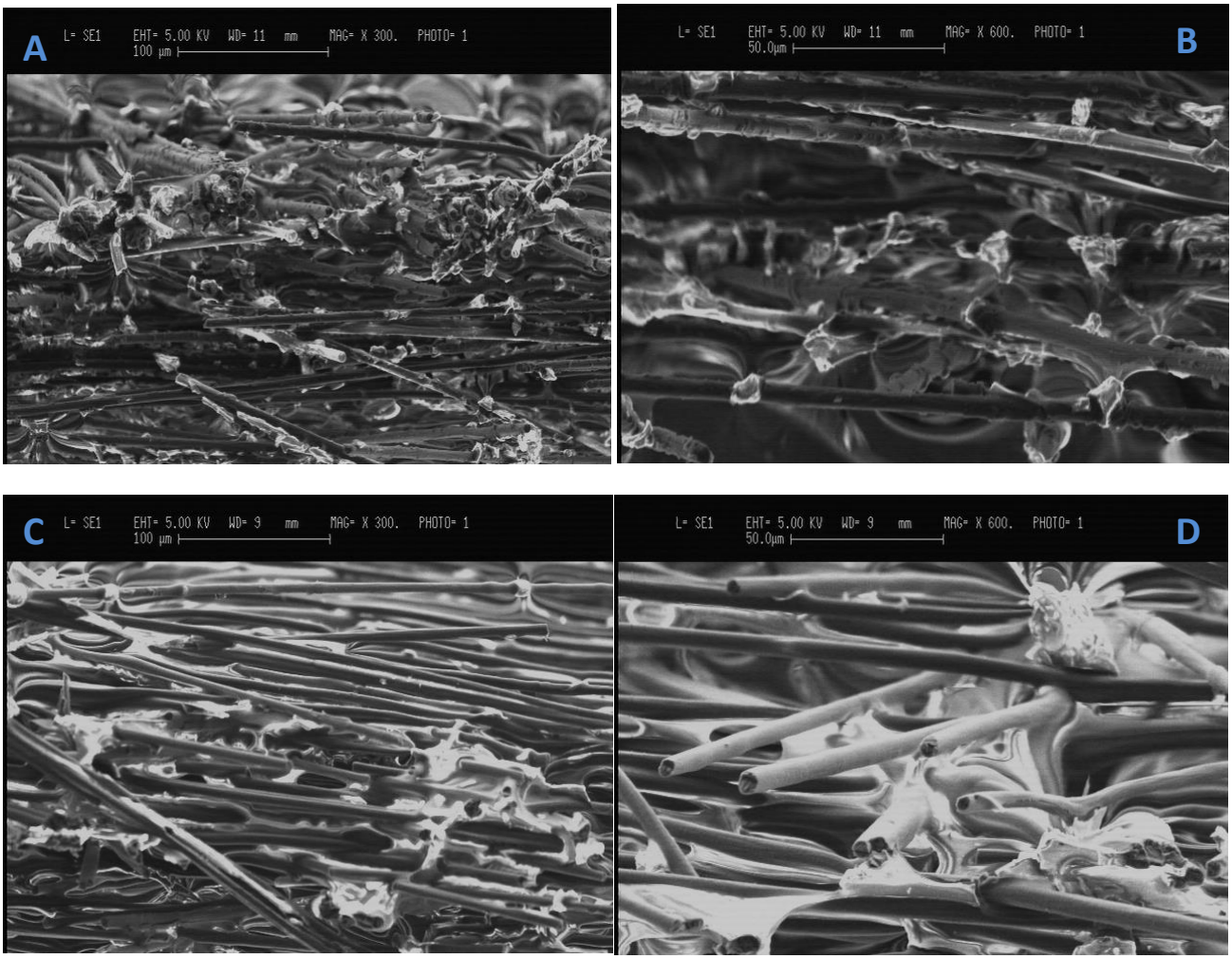

Figure 93 SEM images of: IND-PR 40% at 300X (A), and 600X(B); SAD-ACR 60% at 300X(C) and 600X(D)

References

71. **C. Scarica, G. Griffini, M. Levi and S.Turri,** *Synthesis and characterization of lignin polyesters.* Act of Conference, Roma, 2015.

72. **Fischer.** Path-breaking technology in the measuring microhardness and evaluating material properties. *Acutech.* [Online] [Cited: 11 26, 2016.] http://www.acutech.gr.

73. **Robinson, W. J. CousinsR. W. ArmstrongW. H.** Young's modulus of lignin from a continuous indentation test. *Journal of Materials Science.* 1975, Vol. 10, 1655–1658.

74. **Chew, K.C.** Analysing Organic Coatings. *Materials Mind.* 2015, Vol. 27, 1-2.

75. **T.H. Fanga, W.J.Chang, S.L. Tsai.** Nanomechanical characterization of polymer using atomic force microscopy and nanoindentation. *Microelectronics Journal .* Vol. 36, 55–59.

76. **Barlassina, A.** Studio della lignina nel campo dei trattamenti superficiali di substrati metallici. Milano : s.n., 2016.

77. **(Edt), J. Koleske.** *Paint and Coating Testing Manual.* Philadelphia : s.n. 28-017095-14.

78. **M.A. Dweiba, B. Hub, H.W. Shenton, R.P. Wool.** Bio-based composite roof structure: Manufacturing and processing issues. *Composite Structures.* Vol. 74, 379–388.

79. **N. Graupnera, A. S. Herrmanna , J. Müssigb.** Natural and man-made cellulose fibre-reinforced poly(lactic acid) (PLA) composites: An overview about mechanical characteristics and application areas. *Composites Part A: Applied Science and Manufacturing.* 2009, Vol. 40, 810–821.

80. **By H.P.S. Abdul Khalil, M. Jawaid, A. Hassan, M.T. Paridah and A. Zaidon.** Oil Palm Biomass Fibres and Recent Advancement in Oil Palm Biomass Fibres Based Hybrid Biocomposites. [book auth.] N. Hu. *Composites and Their Applications.* s.l. : InTech, 2012.

81. **J. M. Ferreiraa, C. Capelaa, J. Manaiab , J. D. Costa.** Mechanical Properties of Woven Mat Jute/Epoxy Composites. *Materials Research.* 2016, Vol. 19, 1-6.

4 CONCLUSIONS

The aim of this research work was to contribute to the valorization of the industrial wastes and also to offer innovative solutions to overcome the environmental issues that, year after year, have become always more worrisome. In the context of biorenewable sources, lignin appears to be a promising material still not enough explored. Its versatility of application in plants, from the structural support of the cell walls to the transport of water, strongly suggests that could be transformed into value-added products to apply in a wide range of fields. Among them, it was chosen to perform three functionalizations on a kraft softwood lignin called Indulin, that gave:

1) a lignin-based polyester (SAL), obtained through an esterification reaction between the soluble fraction of Indulin lignin (SLF) and succinic anhydride (SA);
2) a silanized lignin-based anticorrosive coating (LKSi), obtained through a silanization reaction between the soluble fraction of Indulin lignin (SLF) and 3-Isocyanatopropyltrimethoxysilane (IPTMS);
3) A lignin-based crosslinked matrix for composite materials (IND-PR), obtained through the realization of an aqueous solution of Indulin and a crosslinker, Primid, in which carbon fibers were immerged.

These starting materials have been compared to other formulations:

1) The crosslinked polyester SAL Self was compared to a formulation containing a crosslinker (SAL-CYM) in different ratios and a formulation containing the soluble fraction of Indulin (SLF) with the addition of a crosslinker (SLF-CYM) in different ratios.
2) LKSi was compared to a formulation containing a crosslinker (LKSi-TEOS), and to two systems equal to the previous ones containing also a plasticizer, Glycerol ([LKSi]+GLY and [LKSI-TEOS]+GLY).
3) IND-PR was realized in different solution concentrations and compared to an industrial acrylic resin- based matrix for composite materials (SAD-ACR), also at different solution concentrations.

Characterization of these formulations through several types of analysis techniques has been done to investigate their thermal properties, mechanical properties, adhesion strength, corrosion resistance, morphology and surface properties:

1) TGA analysis indicated that the percentage weight losses of the samples occurred at much higher temperatures than the one registered for the uncured precursor (SLF).Thermal analysis performed by means of DSC showed that lignin-based polyesters possess elevated Tg, whose

values increased with the increase of the crosslinker content as a further confirmation of the occurrence of the crosslinking reaction; this results suggest a possible application in materials that need to possess high resistance and rigidity. Microindentation and AFM test further proved the enhanced hardness and modulus value of these formulations with respect to their uncured precursor (SLF); pull-off test showed an high adhesion strength of the formulations to substrates like wood, glass and aluminum, suggesting a possible application as adhesive primers on different materials.

2) Thermal analysis performed by means of DSC showed that silanized lignin-based coatings LKSi and LKSi-TEOS possess elevated Tg; the addition of the plasticizer progressively reduced the glass transition temperature values. Pull-off test showed an high adhesion strength of the formulations to metal substrates like aluminum and steel, suggesting their possible applications as adhesive primers for metal substrates. The introduction of the plasticizer improved the plastic deformation of the coatings, making their application on substrates subjected to mechanical processes like coil coating achievable. Corrosion measurements showed that the formulations were able to protect both aluminum and steel substrates from corrosion attack, and could be utilized as corrosion inhibitor coatings.
3) Dynamic Mechanical Analysis performed on the formulations showed high values of Modulus for the lignin-based samples, comparable and in most of the cases better than the ACR-SAD ones. A study of the morphology by means of SEM technique revealed a dis-homogeneous distribution of the matrix inside the composite fiber network for both the formulations, although lignin-based one resulted much more present in the fibers lattice. From these preliminary analyses seems worthwhile to deepen this field of research, in order to better understand the properties of lignin-based matrixes for composites and to further develop materials to be utilized in composites industry.

Despite being still considered as a waste of the paper production process and utilized as a fuel, lignin has proved to possess a great potential, due to the high glass transition temperature that gives it a elevated rigidity, the high adhesion strength to different substrates like metals, glass and wood, the antioxidant properties that make it a suitable protective coating toward corrosion. The obtained results confirm the initial considerations from which this research work started, turning the hypotheses made on the future development of this material into concrete outcomes.

RINGRAZIAMENTI

Giunta alla conclusione di questo lavoro di ricerca e dunque dei miei studi universitari, sorge spontaneo in me il desiderio di porgere dei particolari ringraziamenti a coloro i quali sono stati parte integrante di questo tanto faticoso quanto soddisfacente percorso universitario e di crescita.

Ringrazio pertanto il Professor Turri, per avermi dato l'opportunità (inaspettata) di potere approfondire un argomento estremamente interessante e per avermi seguito con professionalità e disponibilità nella realizzazione di questo lavoro. Ringrazio il Dott. (Prof.) Gianmarco Griffini, che con i suoi preziosi consigli e la sua inesauribile pazienza è stato costante motivo di sprono e di miglioramento, insegnandomi a padroneggiare concretamente le conoscenze acquisite con lo studio. Ringrazio Gilly, che con immancabile premura e attenzione si è presa cura dei miei lavori.

I miei più profondi ringraziamenti vanno: alla mia famiglia, per aver sempre creduto nelle mie possibilità, per avermi insegnato che l'onestà e la tenacia danno sempre i loro frutti, per aver colmato col loro infinito amore la distanza che ci ha divisi; a Verdiana, per avermi fatto dono, ogni giorno, della sua incredibile forza e della sua inesauribile dolcezza; a Sara ed Erika, per avermi insegnato che la distanza non è mai un limite; a Francesca C, per avermi insegnato che bisogna sempre perseguire i propri sogni; a Gabriele, per aver riempito le mie giornate universitarie (e non) della sua allegra compagnia; a Giuseppe C, per avere ascoltato i miei pensieri senza alle volte doverli neppure esprimere, a Luca M, per il suo costante e immancabile supporto in ogni circostanza.

Ringrazio Caterina, Giovanni P, Nelly, Valeria, Carmen e Riccardo per avermi insegnato che essere tesisti, in fondo, non è poi così male se questo tempo lo si trascorre al fianco di persone così belle.

Ringrazio infine il Collegio San Paolo, per avermi insegnato il significato delle relazioni.